Reconfigurable Metasurfaces in Nanoelectromechanical and Silicon-Organic Systems

Thesis by
Tianzhe Zheng (郑天哲)

In Partial Fulfillment of the Requirements for the
Degree of
Doctor of Philosophy in Applied Physics

Caltech

CALIFORNIA INSTITUTE OF TECHNOLOGY
Pasadena, California

2024
Defended January 23, 2024

To my parents, 郑向阳 *and* 齐文娟*.*

ACKNOWLEDGEMENTS

When I took a flight to Pasadena in the summer of 2018, I never imagined what an incredible Ph.D. journey it would be. Looking back, choosing Caltech was the best decision I have ever made. From the beginning of my Ph.D., my goal was to delve deeply into a field and develop my own understandings. Now, looking back, I am proud to say that I have fully achieved this. Caltech is one of the best places for a Ph.D. student: the world-class facilities, warm and beautiful campus, and most importantly, the people who I could always learn from. Here are the people that I would like to express my gratitude during this journey:

First and foremost, I would like to extend my heartfelt thanks to my Ph.D. advisor Professor Andrei Faraon not just for welcoming me into Faraon lab, but for cultivating the chill and loose environment where academic research was a joyful and exciting adventure. Thank you for letting me choose the project I wanted to pursue and support me whenever I met difficulties.

Next I would like to thank Professor Kerry Vahala, Professor Alireza Marandi and Professor Axel Scherer, who serve as my doctoral defense committee. Also I would like to thank Professor Azita Emami for being my candidacy committee. I'm grateful for Dr. Andrey Matsko and Dr. Alireza Ghaffari. The TA experience taught me more fundamental concepts and improved my English communications.

I am immensely grateful to my flat-optics colleagues. When I first joined the group, Sarah, Ehsan, Mahsa and Sadegh provided a lot of initial guidance and ongoing support. Hyounghan was my mentor for the first several years of my graduate studies. He showed me how to initiate and organize a project. During the COVID-19 period, we have to alternatively conduct experiments in the lab. This was an unforgettable experience. Even today, his big-picture perspective on scientific research and his approach to problem-solving continue to influence me. Beyond the scope of this thesis, I learnt a lot about the inverse design technique computational imaging from Conner and Greg. They are always fun to work with. As native speakers, they also provide valuable advice for my academic writing. Thanks to Suki, Bilgehan, and Phillippe for collaborating on different projects. Suki is very hard-working, and actively participated in a lot of fabrication work. Bilgehan is always focused and meticulous, taking every project with great care. Phillippe is smart and insightful, and his creative ideas are always extremely progressive for the projects. I am also

grateful for Ian, Neuton for the meaningful discussions. A special thanks to Ding; as a independent postdoc researcher, he was extremely helpful to the flat-optics team with his expertise on the optical alignment and 2D materials.

I would like to say thank you to all the members in Faraon Group. Tian is the same-year cohort in the same group, and we always share our common difficulties in work and life. Thanks to Mi for the joyful conversations at the office and lessons on the quantum concepts. Thanks to Andrei for many late night discussions and hiking/skiing guidance. Thanks to Chun-Ju for your pineapple cake. Thanks to all the Faraon group members, including John, Jon, Chuting, Ioana, Jake, Daniel, Riku, Sophie, Jiahui, Emmanuel, McCoy, Erin, Will, and Faraz. Thanks to Cecilia for helping with the administration work.

My Ph.D. research wouldn't have been possible without the help with Kavli Nanoscience Institute (KNI). Thanks to all the staff who helped me with the fabrication tools and techniques, including Guy, Bert, Alex, Nathan, Matt, Lena, Kelly, Tiffany and Jennifer. I also thank the people I met there, especially Alessandro. During lonely nights in the clean room, I could always ask you for help.

I also need to thank all the collaborators for different projects. Professor Julia Greer, Matias and Andrew are great researchers who maximize the power of our metasurfaces in lithography. Jeff and Mahmood helped me understand the metausrface in astronomy applications. All the employees in NLM Photonics provided the OEO material and processing guidance. Thanks for your pioneering product that enabled the OEO project.

I would like to thank all my mentors in the industry internship at Apple, including Fang, Nate, Xiaobin, and Amin. The fast-paced workstyle and new type of industrial problems reshape my perspective of the photonics problems.

Outside of work, I also met many new friends in Caltech. It is very lucky that my roommates became my great friends. Leo, Yifan and Ruizhi, thanks for the lunches and dinners we had at home. Sharing life trivias with each other is relaxing after work. Thanks to many friends who helped me along the journey, including Yang, Zhiquan, Yuchun, Xiaoqiao, Yongzhao, Cheng, Duxing, Mingchen, Yiran, Jialong, Yangcheng and many more. I had a colorful life during these years. Wen-loong, Xiang, Roger, and Honglie, thanks for sharing your experiences and advice during the first several years of my Ph.D. I am also grateful to have many undergraduate friends that communicate regularly. Fenghao, Yuhao, Yukai, Jiayu, Yuhao, thanks

for all the stories and news we shared and the encouragement we received.

Thanks to Yijun, your support is the best comfort any time. Meeting you here is one of the luckiest things in my life.

Last but not least, no matter how far we are, my parents are always my best support. Thank you to my father and mother; although thousands of miles apart, our weekly phone calls always let me feel you will be my side. Your unconditional love makes me not afraid of any failures.

ABSTRACT

Over the past decade, metasurfaces, a technology referring to 2D or 3D engineered nanostructures, has demonstrated itself as a groundbreaking solution for creating compact and multifunctional optical devices. Moreover, the integration of metasurfaces with various modulation techniques enables compact yet high-performance active optical systems. In this thesis I explore various optical modes in engineered nanostructures and apply different design techniques to improve the amplitude and phase response of free-space modulators.

In Chapter 1 and 2, we first briefly introduce the concept of reconfigurable metasurfaces and its state of art. Then we introduce several nanophotonic concepts that will be used frequently in later projects and discuss the potential directions to improve modulator's performance.

In Chapter 3, we find that the dual-mode resonant metasurfaces could improve the phase response in the nanoelectromechanical system(NEMS). The interaction between the quasi-bond state in the continuum and guided mode resonance boosts the phase response up to $144°$.

In Chapter 4, the design target is to utilize the high-Q mode to decrease the driving voltage of the NEMS system to CMOS level. Motivated by the low-index confinement property of the slot mode, the device achieves over 10% reflection amplitude modulation with only 1.5V in the experiment. In addition, by adding a bottom gold mirror, 1.8π phase response is numerically observed. Based on the success of this device, we propose a design that could achieve subwavelength wavefront control. As a example, we show a 3-pixel optical beam deflector with 75% diffraction efficiency.

In Chapter 5, we extend the use of the slot mode into silicon-organic hybrid devices. The utilization of the slot mode achieves efficient electro-optic tuning under 17V in free space with a MHz modulation speed. We also explored various methods to enhance its phase response and discuss its feasibility. The spatial phase modulation design is also proposed with a 12-period supercell pixel. The beam deflector achieves 70% diffraction efficiency numerically.

In Chapter 6, we bring this dissertation to a close and outline potential directions for future research.

This thesis provides a foundation for the development of high-resolution and power-efficient one-dimensional spatial light modulators and showcases the potential of

reconfigurable metasurfaces.

PUBLISHED CONTENT AND CONTRIBUTIONS

[1]T. Zheng, Y. Gu, H. Kwon, G. Roberts, and A. Faraon, "Dynamic light manipulation via silicon-organic slot metasurfaces", Nature Communications 2024 15:1 **15**, 1–10 (2024),
T.Z. participated in the conception of the project, design of the devices, sample fabrication, sample measurement, data analysis and writing of the manuscript.

[2]T. Zheng, H. Kwon, and A. Faraon, "Nanoelectromechanical tuning of high-q slot metasurfaces", Nano Letters **23**, 5588–5594 (2023),
T.Z. participated in the conception of the project, design of the devices, sample fabrication, sample measurement, data analysis and writing of the manuscript.

[3]H. Kwon, T. Zheng*, and A. Faraon, "Nano-electromechanical tuning of dual-mode resonant dielectric metasurfaces for dynamic amplitude and phase modulation", Nano Letters **21**, 2817–2823 (2021),
T.Z. participated in the sample fabrication, sample measurement, data analysis and writing of the manuscript.

TABLE OF CONTENTS

LIST OF ILLUSTRATIONS

LIST OF TABLES

C h a p t e r   1

INTRODUCTION: RECONFIGURABLE META-OPTICS

In the past decade, the emergence of meta-optics has garnered widespread attention. This chapter is dedicated to providing a background about the area of reconfigurable metasurfaces, discussing its current advantages and challenges. We will first provide a concise overview of meta-optics' origins, followed by a summary of the current state of metasurfaces. The chapter culminates with a discussion of the recent advancements in reconfigurable meta-optics.

1.1   Meta-optics: flat optical components

Meta-optics refers to the research area that investigates subwavelength artificial patterns that are designed to modify different characteristics of light such as wavefronts, polarization distributions, intensity distributions, or spectra[1–7]. While encompassing a broad spectrum, the genesis of meta-optics can be traced back to the simple idea of controlling light's phase. Long before Maxwell's realization that light is an electromagnetic wave, it was known that a sphere could focus light, a phenomenon explained by Fermat's principle. When a human has the capability of fabricating subwavelength structures, the question naturally arose: could subwavelength features alone induce a phase shift? This query first surfaced within the microwave community, exemplified by microwave reflectarrays [8, 9], where it was discovered that varying the size and shape of microstrips alters the phase change. A significant leap in the field occurred in 2011, when researchers found that changing the shape and size of subwavelength components can locally alter the phase response of the emitted microwave [10]. This breakthrough propelled the field forward, opening avenues for non-periodic two-dimensional nanostructure design and subsequently adapting these concepts to optical wavelengths, thanks to advancements in fabrication techniques. After a decade development, metasurfaces have expanded their application across numerous photonics fields, positioning themselves as competitive candidate to many traditional optical components.

Metasurfaces offer several advantages over conventional optical components:

Compact and flat optical solutions

Metasurfaces utilize nanostructures to manipulate optical properties, resulting in a micrometer-scale thickness and a flat overall structure. This offers a compact and efficient alternative to bulk optical components and systematic optical solutions. Metasurfaces have provided alternatives for various optical components such as lenses[11], polarizers[12], and absorbers[13]. Furthermore, they offer novel optical solutions for existing applications, such as on-chip spectrometers[14] and quantitative phase imagers[15]. The primary goal in utilizing metasurfaces is to reduce the size and cost of optical solutions, thereby broadening their application scenarios.

Multifunctionality

The multifunctionality of metasurfaces, enabled by the flexible design of their nanostructures, dramatically expands their capabilities beyond mere phase control. These advanced surfaces can adeptly manage multiple optical properties simultaneously, such as harmonizing phase with polarization or amplitude [1, 16], or intertwining phase control with angular manipulation [17]. This multifunctional nature is not confined to generic optical controls; it also extends to highly specialized applications. Innovations such as color routers [18] and optical differentiators [19, 20] are prime examples of how metasurfaces can be tailored for complex but distinct, application-specific functions. This exceptional versatility highlights the potential of metasurfaces to revolutionize various technological domains through their multifaceted functionalities.

Large-scale fabrication and monolithic integration

Compared to the traditional grinding and polishing process for lenses and mirrors, CMOS-compatible fabrication techniques offer significant advantages in producing metasurfaces. These methods can create thousands or even millions of devices on a single wafer, drastically reducing the cost of optical components [21]. Furthermore, while single-layer metasurfaces have shown promise in various applications, their ultra-thin nanostructures inherently impose certain limitations [22, 23]. CMOS-compatible fabrication not only overcomes these limitations but also enables monolithic integration, substantially enhancing the utility and performance of metasurfaces. Notable examples of such advancements include multiwavelength metalenses [24, 25], demonstrating the significant potential of this approach.

1.2 Reconfigurable meta-optics

In the previous section, we demonstrated the significant achievements of metasurfaces in various photonics areas, highlighting their integral role in developing static optical solutions. This progress leads us to an intriguing question: Can the principles of metasurfaces be applied to active optical components? The answer is yes! The insights gained from arranging nanoscale patterns in static applications can be undoubtly applied to the design of active optical elements. Consequently, reconfigurable metasurfaces have become a popular scientific research area in recent years. Numerous studies are dedicated to exploring the integration of diverse modulation techniques with metasurfaces. In this section, we aim to present the key metrics of reconfigurable metasurfaces and discuss the latest progress in this rapidly evolving field.

Reconfigurable metasurfaces have a wide range of applications. Within the scope of this thesis, our primary focus is on devices that modulate reflective amplitude and phase. Consequently, we will specifically examine reflective modulators as our primary example. To illustrate this, we identify three key objectives that we aim to achieve with these modulators, as depicted in Fig. 1.1:

- Figure of merit

- Modulation speed

- Spatial resolution

Fig. 1.1 further outlines the relevant parameters for each metric associated with reconfigurable metasurfaces. First, the direct measure of the device performance is the figure of merit (FoM), which we aim to optimize. For example, in reflective amplitude modulation, the extinction ratio ($\Delta R/R_{\text{off}}$) is one of the key metrics we would like to enhance. In reflective phase modulation, the ideal device would enable full 2π phase modulation with uniform amplitude. Second, modulation speed is crucial in high-speed applications. It is related to the minimum switching time (T), and is largely constrained by the tuning mechanism. Finally, higher spatial resolution (higher p_x, p_y) is desireable, as it allows more pixels in the same area.

It is clear that no solution could realize high performance in all four factors simultaneously. Over the past several years, there has been extensive exploration into the combination of various modulation techniques, material platforms and nanophotonic structure designs aiming to balance these factors. In this section, we will
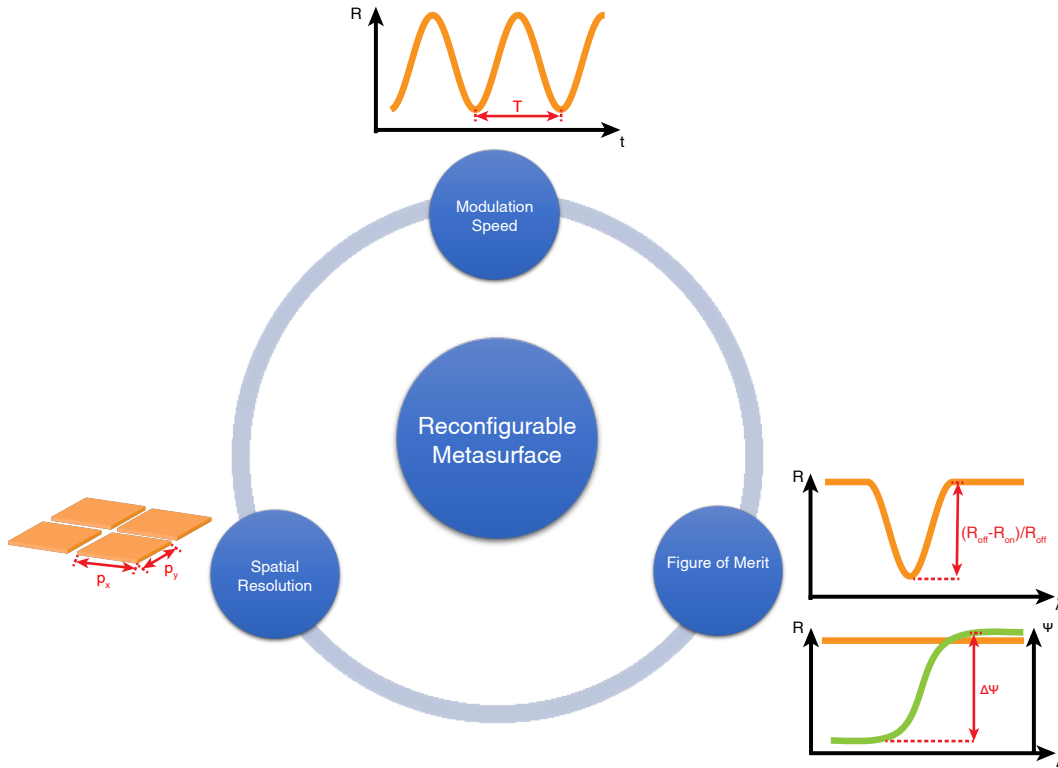
Figure 1.1: **Key metrics for reflective reconfigurable metasurfaces**. Top: modulation speed. R: the reflection amplitude response. T: the modulation time period. Bottom left: spatial resolution. p_x and p_y: the device pixel size in x and y. Bottom right: Figure of merit. λ: incident light wavelength. R_{off}: the reflection amplitude without external stimuli. R_{on}: the reflection amplitude without external stimuli. Φ: the reflection phase response.

provide an overview of major tunable mechanisms, along with a discussion about their advantages/disadvantages.

Electrical modulation

Electrical modulation is the most prevalent modulation technique, primarily because the electrical system is one of the most convenient driving methods and many material platforms have giant refractive index changes under voltage or electrical pulses. For instance, transparent conducting oxides have been proven to show high-speed, high-resolution spatial phase modulation both in one dimension or two dimensions[26–29]. The key idea involves utilizing the epsilon-near-zero (ENZ)[1] property to achieve substantial refractive index tuning. However, this ENZ region also introduces significant absorption, which in turn limits reflection effi-

---

[1]epsilon-near-zero means the real value of the permittivity is close to zero.

ciency. 2D materials exhibit remarkable refractive index tuning under cryogenic temperature[30] and even in room temperature[31]. However, its small mode of volume requires the use of high-Q cavity[32] or results in relatively small change of FoM[33, 34]. Phase-change materials can undergo substantial discrete refractive index changes with short electrical pulses [35, 36], but their limited lifecycle or endurance poses a challenge for practical applications. On a different note, liquid crystals[37, 38] offer significant refractive index modulation and low driving voltage, and has been commercialized in devices such as spatial light modulators. However, their operation speed is typically limited in kHz range. In Chapter 5, we will explore the silicon-organic platform which utilizes electro-optic effect and design a high-Q cavity to enhance its sensitivity.

Mechanical modulation

Mechanical modulation methods also often employ electrical voltage to generate mechanical forces. However, since the core principle is to use the mechanical movement to induce changes of the optical response, we should distinguish them into a single category. One simple way to induce mechanical movements is to use flexible substrates such as polydimethylsiloxane(PDMS) and stretch them. Metasurface based on flexible substrates could modify the optical properties[39], but it is challenging to achieve systematic and programmable tuning. One of the most important active metasurface is the integration with nanoelectromechanical/microelectromechanical (NEMS/MEMS) techniques[40, 41], since the MEMS/NEMS technology maturity provides a convenient path towards commercialization. Despite its great success, this approach typically requires high voltage for operation [41]. In chapters 3-4, we will delve into our research on NEMS metasurfaces.

Thermal modulation

Thermal modulation of the metasurface leverages the principle that temperature increase of the material will also induce large and continuous refractive index shift. Therefore, there are several works utilizing thermal-optics to make varifocal lens[42] or even wavefront engineering[43]. However, the practical application of thermal modulation faces challenges, particularly in achieving localized tuning and overcoming the inherent speed limitation of thermal response. These limitations highlight the need for further advancements before thermal modulation can achieve commercial success.

Optical modulation

Photoexcited free carriers[44] could induce small refractive index perturbations. The electrooptic effect is small but fast; therefore a high-Q cavity is necessary to enhance the optical response. Recently a photonic crystal cavity spatial light modulator has been demonstrated[45]. It achieved a high-speed 2D spatial light modulator with wafer scale fabrication. Therefore, it is a great candidate for high-speed optical addressing and control applications.

1.3   Thesis outline

In Chapter 2, we will discuss basic concepts that are relevant to the nanophotonic design technique. In Chapter 3, we will design a dual-mode resonant nanoelectromechanical metasurface that could provide enhanced phase response. In Chapter 4, we will further reduce the required voltage of NEMS metasurface by utilizing slot mode. In Chapter 5, we will combine the slot mode with organic electro-optic material to design a free-space electro-optical modulator. Finally, we will provide some conclusions and thoughts on possible future work in Chapter 6.

Chapter 2

BASIC CONCEPTS IN NANOPHOTONICS

This chapter will discuss some basic concepts that will be used in the following chapters. The contents of this chapter borrow heavily from the book[46].

2.1   Eigenmodes in Maxwell equations

Mathematically speaking, the nanophotonic problem could be transformed into partial differential equations (PDEs). Given the refractive index profile $\epsilon(\mathbf{r})$ and the source $\mathbf{J}(\mathbf{r})$, what is the result of the electrical field $\mathbf{E}(\mathbf{r})$ and magnetic field $\mathbf{H}(\mathbf{r})$. The governed PDEs are Maxwell equations:

$$\nabla \cdot \mathbf{B}(\mathbf{r}, t) = 0 \tag{2.1}$$

$$\nabla \times \mathbf{E}(\mathbf{r}, t) + \frac{\partial \mathbf{B}(\mathbf{r}, t)}{\partial t} = 0 \tag{2.2}$$

$$\nabla \cdot \mathbf{D}(\mathbf{r}, t) = \rho(\mathbf{r}, t) \tag{2.3}$$

$$\nabla \times \mathbf{H}(\mathbf{r}, t) - \frac{\partial \mathbf{D}(\mathbf{r}, t)}{\partial t} = \mathbf{J}(\mathbf{r}, t) \tag{2.4}$$

In general, the relation between $\mathbf{D}$ and $\mathbf{E}$ and $\mathbf{B}$ and $\mathbf{H}$ could be expressed via a power series:

$$\frac{D_i}{\epsilon_0} = \sum_j \epsilon_{ij} E_j + \sum_{j,k} \chi_{i,j,k} E_j E_k + O(E^3) \tag{2.5}$$

$$\frac{B_i}{\epsilon_0} = \sum_j \mu_{ij} H_j + O(H^2) \tag{2.6}$$

where ϵ_0 is the vacuum permittivity. The higher order term between $\mathbf{D}$ and $\mathbf{E}$ and $\mathbf{B}$ and $\mathbf{H}$ are all nonlinear effects. In this thesis, only second-order electro-optic effect will be considered in Chapter 6.

To simplify the discussion, we will make four approximations in this chapter:

- Ignore nonlinear effect

- no source term (ρ and $\mathbf{J}$)

- isotropic media ($\epsilon_{ij} = \epsilon_r$)

- The materials are not magnetic materials($\mu_{ij} = 1$)

Based on these approximations, the Maxwell equations become

$$\nabla \cdot \mathbf{H}(\mathbf{r}, t) = 0 \tag{2.7}$$

$$\nabla \times \mathbf{E}(\mathbf{r}, t) + \mu_0 \frac{\partial \mathbf{H}(\mathbf{r}, t)}{\partial t} = 0 \tag{2.8}$$

$$\nabla \cdot (\epsilon_r(\mathbf{r})\mathbf{E}(\mathbf{r}, t)) = 0 \tag{2.9}$$

$$\nabla \times \mathbf{H}(\mathbf{r}, t) - \epsilon_0 \epsilon_r \frac{\partial \mathbf{E}(\mathbf{r}, t)}{\partial t} = 0 \tag{2.10}$$

To further investigate the properties of the electric and magnetic fields under certain permittivity distributions, we could decompose the fields under various frequencies and expand the field into a set of harmonic eigenmodes. Specifically, we assume that the fields are complex and have the following format

$$\mathbf{H}(\mathbf{r}, t) = \mathbf{H}(\mathbf{r})e^{-i\omega t} \tag{2.11}$$

$$\mathbf{E}(\mathbf{r}, t) = \mathbf{E}(\mathbf{r})e^{-i\omega t} \tag{2.12}$$

The actual value of the fields at given time and spatial coordinate is the field in the real value of the complex number. Under this harmonic decomposition, the Maxwell equation in frequency domain could be written as

$$\nabla \cdot \mathbf{H}(\mathbf{r}) = 0 \tag{2.13}$$

$$\nabla \times \mathbf{E}(\mathbf{r}) - i\omega \mu_0 \mathbf{H}(\mathbf{r}) = 0 \tag{2.14}$$

$$\nabla \cdot (\epsilon_r(\mathbf{r})\mathbf{E}(\mathbf{r})) = 0 \tag{2.15}$$

$$\nabla \times \mathbf{H}(\mathbf{r}) + i\omega \epsilon_0 \epsilon_r \mathbf{E}(\mathbf{r}) = 0 \tag{2.16}$$

Combining 2.14 and 2.16, we have

$$\nabla \times \nabla \times \mathbf{E}(\mathbf{r}) = \frac{\omega^2}{c^2} \epsilon_r \mathbf{E}(\mathbf{r}) \tag{2.17}$$

The solution of electric field from 2.17 and its corresponding magnetic field by 2.14, are eigenmodes at given permittivity distribution and frequency. For general nanostructures, we need to use numerical solvers to get the fields. Instead of directly solving eigenmodes, our focus is to analyze the effects of the eigenmodes interacting with incident light and under small perturbations.

2.2 Small perturbation on the eigenmode

If we define the operator $\Phi = \nabla \times \nabla \times - \frac{\omega^2}{c^2}\epsilon_r$, then Φ is a linear operator. Perturbation theory could be applied[47]. The normalization condition in this euqation is

$$\iiint_{-\infty}^{\infty} \mathbf{E}_{\mathbf{m}}^{\dagger}\epsilon_r\mathbf{E}_{\mathbf{n}}\mathrm{d}x\mathrm{d}y\mathrm{d}z :=< \mathbf{E}_{\mathbf{m}}, \epsilon_r\mathbf{E}_{\mathbf{n}} >= \delta_{mn} \tag{2.18}$$

Assume we have small perturbation $\Delta\epsilon_r(\mathbf{r})$, the shift of the frequency could be expressed in 2.19.

$$\frac{\Delta\omega_i}{\omega_i} = -\frac{1}{2}\frac{< \mathbf{E_i}, \Delta\epsilon_r\mathbf{E_i} >}{< \mathbf{E_i}, \epsilon_r\mathbf{E_i} >} \tag{2.19}$$

For most of the reconfigurable metasurfaces, external stimuli will cause the change of the permittivity distribution. It is worth to point out that mechanical movement could be viewed as changing some parts of the material permittivity to air permittivity and vice versa.

2.3 Guided Mode(GM) and Guided Mode Resonance (GMR)

In general, the modes that nanostructures host can only be solved by numerical software and don't have general rules to describe them. Therefore, we are more interested in structures with more symmetry. If the structure has discrete translational symmetry or it is periodic, then one important type of eigenmodes in periodic structures are guided modes(GM).

Guided mode originates from the basic idea of the light confinement. To start with, first we could consider a high-index slab in low-index environment shown in the Fig. 2.1a-b. As long as the slab has enough thickness, the light could propagate inside the high refractive index slab without any loss. This could be understood by the dispersion relationship of the eigenmode inside the slab in Fig. 2.1b. There are many eigenmodes which are highly confined within the slab. We call this type of eigenmode 'guided mode' because the high refractive index slab 'guided' the light propagation. In Fig. 2.1b the blue curve represents the dispersion relationship of a guided mode. In addition, we also plot the air light line (the line splits the grey region and white region). All the points in the air light line follows the relationship $\omega = ck_x$, where ω is the frequency, c is the light speed in air, k_x is the wave vector in x direction. All the mode below the air light line couldn't couple to the free-space light because of the physical limitation $k_x \leq \frac{\omega}{c}$. Therefore, the guided mode is decoupled with the free-space light and doesn't have any energy loss when propogating.
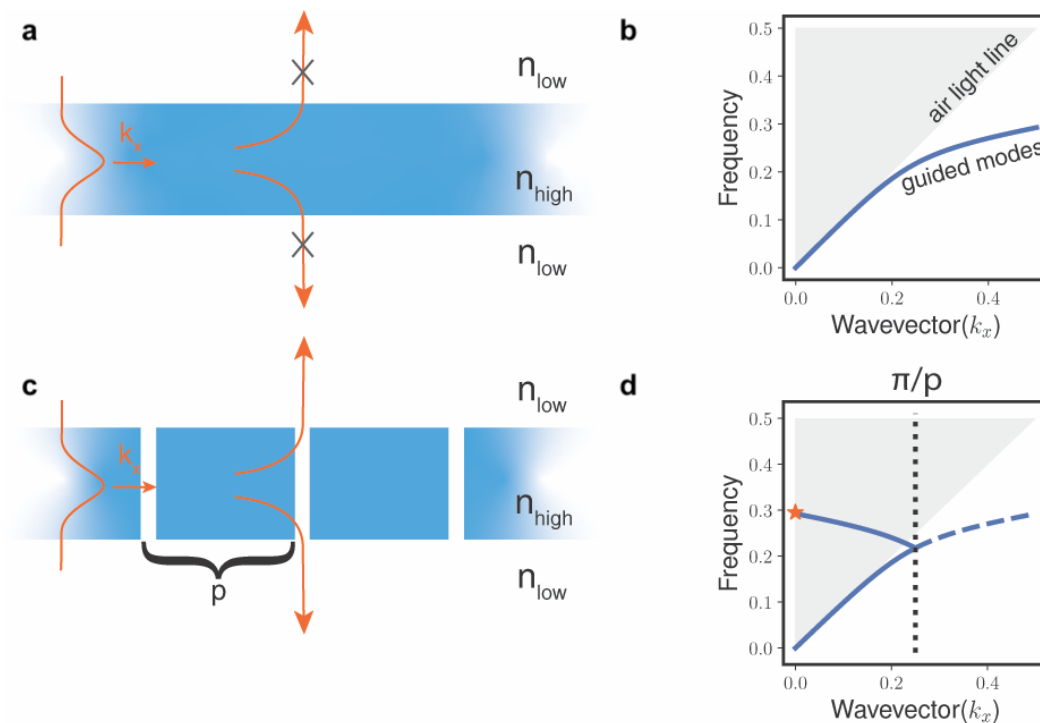
Figure 2.1: **Guided mode and guided mode resonance illustration**. **a:** the example of guided mode. The high refractive index slab hosts an optical mode inside the slab. The mode is bounded since the guided mode is below the light cone. **b:**the dispersion relationship of the guided mode in **a**. The grey region is above the air light line, indicating that the mode is accessible to the free-space. The guided mode falls below the air light line, therefore cannot couple with the free-space light. **c:** the example of guided mode resonance. The perturbation transforms the slab into a high-contrast grating with period p. **d:** the dispersion relationship of the guided mode in **c**. The periodic perturbation folds the dispersion of the guided mode into the grey region. Therefore the guided mode could couple with the free-space light. The orange star suggests the frequency where the normal incident light could couple with the mode.

In addition to a high refractive-index slab, we could add perturbations to modify the dispersion curve. For example, we could add periodic perturbations to create a grating with a periodicity p, shown in Fig. 2.1c. In this case, the light will not be perfectly confined inside the slab but will leak towards the upper and lower media at some frequencies[48]. In the dispersion relationship in Fig. 2.1d, the periodic perturbation adds a folding operation to the guided mode curve. As a result, the curve is within the grey region and could couple with the free space light. Therefore, we will see a sharp resonance in the free-space reflection or transmission spectra. This type of resonance originates from the interaction between the leaky waveguide and the incident light, therefore it is called 'guided mode resonance'(GMR).

GMR has been thoroughly investigated theoretically and numerically and has been widely used as a frequency filter[49]. Many type of metasurfaces also support GMR[50, 51]. As a old concept, the combination with the metasurfaces will provide a powerful tool for the desired optical responses.

2.4   Bound states in the continuum (BIC)

In addition to the guided mode resonance, there are other types that could be used. The BIC mode has received significant interests because these exotic resonant states could still be perfectly trapped in the extended structures despite its existence within the energy spectrum of the continuum [52, 53]. The difference between the GMR and BIC is where the mode exists without the perturbation. Previously, GMR showed that the periodic perturbation of the bound state could enable the free-space coupling of the optical mode. Since these bound states usually lie below the light cone, their existence is out of the energy spectrum of the continuum. The origin of the BIC comes from different sources, such as symmetry protection[54], interference effect and parameter tuning[55] or inverse construction[56]. The key property of the BIC is that it is perfectly protected from the continuum media. Therefore, when there is small perturbation, the condition of the bound states is broken, and the optical mode will start to radiate[57]. We call this perturbed state quasi bound state in the continuum (quasi-BIC). By controlling the parameters, we could control the strength and the direction of the leakage, resulting in the controllable quality factor and shape for the resonance. This concept provides the flexibility of designing sharp resonances in the optical response and has been applied in various applications such as lasers[58], nonlinear photonics[59], and modulators[60].

2.5 Temporal Couple Mode Theory (TCMT)

In this section, we start to consider the interaction of the input light with the eigenmodes. We will introduce the general framework of the temporal couple mode theory(TCMT). Especially, we will investigate the case where there are only two ports. The main framework is adapted from the work[61].

Any optical eigenmodes could be treated as a single-mode optical resonator. The outside interactions could be described as the coupling ports. Thus, we could describe the time dynamics of the resonator:

$$\frac{dA}{dt} = (i\omega_0 - \frac{1}{\tau})A + (\langle\kappa|^*)\,|s_+\rangle \tag{2.20}$$

$$|s_-\rangle = C\,|s_+\rangle + A\,|d\rangle \tag{2.21}$$

Here A is the amplitude of the mode, ω_0 is the center frequency of the mode, τ is the total lifetime of the mode. Assume we have m ports, the incident wave from the ports is expressed as $|s_+\rangle$, and the outgoing waves are expressed as $|s_-\rangle$. κ represents the coupling constants between the input wave and the resonators, and d represents the coupling constants between the output wave and the resonators:

$$|s_+\rangle = \begin{pmatrix} s_{1+} \\ s_{2+} \\ ... \\ s_{m+} \end{pmatrix}, |s_-\rangle = \begin{pmatrix} s_{1-} \\ s_{2-} \\ ... \\ s_{m-} \end{pmatrix}, \langle\kappa|^* = \begin{pmatrix} \kappa_1 \\ \kappa_2 \\ ... \\ \kappa_m \end{pmatrix}, |d\rangle = \begin{pmatrix} d_1 \\ d_2 \\ ... \\ d_m \end{pmatrix} \tag{2.22}$$

The coefficients listed in equations 2.20 and 2.21 are not independent. By energy conservation, we could first get

$$\langle d|d\rangle = \frac{2}{\tau} \tag{2.23}$$

If we further apply the time-reversal symmetry[61], several conclusions could be derived:

$$|\kappa\rangle = |d\rangle \tag{2.24}$$

$$C\,|d\rangle^* = -\,|d\rangle \tag{2.25}$$

Assuming that the incident wave frequency is ω, combine equation 2.20 and 2.21 and we have

$$A = \frac{\langle d|^*\,|s_+\rangle}{i(\omega - \omega_0) + \frac{1}{\tau}} \tag{2.26}$$

Based on equations 2.20-2.26, we have

$$|s_-\rangle = (C + \frac{|d\rangle \langle d|^*}{i(\omega - \omega_0) + \frac{1}{\tau}}) |s_+\rangle \qquad (2.27)$$

If we consider the reflection coefficients $|r\rangle = \frac{|s_+\rangle}{|s_-\rangle}$, we have

$$|r\rangle = |r_b\rangle + \frac{|r_m\rangle}{i(\omega - \omega_0) + \frac{1}{\tau}} \qquad (2.28)$$

Here $|r_b\rangle$ represents the background reflection coefficient for each port, and $|r_m\rangle$ represents the mode amplitude on resonance. The contribution of the mode interaction also depends on the total loss rate.

From these equations, we have a qualitative understanding of the reflection coefficient across a mode. When the input light frequency is far off resonance, the behavior is determined by the scattering matrix C or background reflection coefficient $|r_b\rangle$. The mode amplitude $|r_m\rangle$ and loss τ determine the Fano shape of the resonance[61].

Based on the origin of the loss, we could split the total loss into several categories:

$$\frac{1}{\tau} = \frac{1}{\tau_1} + ... + \frac{1}{\tau_m} + \frac{1}{\tau_a} + \frac{1}{\tau_s} \qquad (2.29)$$

Here $\tau_i, i = 1, ..., m$ represent the radiation through each port, and τ_a is the absorption loss due to the materials. τ_s is the scattering loss. Engineering the structure could significantly control different parts of the loss. Combined with equation 2.28, we could engineer the structure to achieve the desired amplitude and phase response.

TCMT with two ports

In practical devices discussed in this dissertation, we only have two ports or four ports. Here we first discuss a simplified situation; the incident light directly couples into one single mode and then couple out from two radiation ports. This corresponds to a device where we only have one radiation channel in each direction. In other words, consider a normal incident light into the device from the top, if the device has no diffraction, then the device could only radiate through the top channel (reflection) and the bottom channel (transmission). In this case, we could rewrite the equations 2.27 and 2.28:

$$\begin{bmatrix} s_{1-} \\ s_{2-} \end{bmatrix} = C \begin{bmatrix} s_{1+} \\ s_{2+} \end{bmatrix} + \frac{1}{i(\omega - \omega_0) + \frac{1}{\tau}} \begin{bmatrix} d_1^* \\ d_2^* \end{bmatrix} \begin{bmatrix} d_1 & d_2 \end{bmatrix} \begin{bmatrix} s_{1+} \\ s_{2+} \end{bmatrix} \qquad (2.30)$$

Since C is the direct-transport scattering matrix from two ports[62], we could assume that

$$C = e^{i\phi_d} \begin{bmatrix} r & it \\ it & r \end{bmatrix} \tag{2.31}$$

Also with equation 2.25, we have

$$r_1 = \frac{s_{1-}}{s_{1+}}\Big|_{s_{2+}=0} = r + \frac{d_1^2}{i(\omega - \omega_0) + \frac{1}{\tau}} \tag{2.32}$$

$$r_2 = \frac{s_{2-}}{s_{2+}}\Big|_{s_{1+}=0} = r + \frac{d_2^2}{i(\omega - \omega_0) + \frac{1}{\tau}} \tag{2.33}$$

Since there are only two radiation ports, the loss rate could be expressed as $\frac{1}{\tau} = \frac{1}{\tau_1} + \frac{1}{\tau_2} + \frac{1}{\tau_{nr}}$. τ_1 and τ_2 are radiation rate from the port 1 and port 2, respectively, and τ_{nr} is the non-radiation loss rate. From equation 2.23 we could assume that

$$d_1 = \sqrt{\frac{2}{\tau_1}} e^{i\theta_1}, d_2 = \sqrt{\frac{2}{\tau_2}} e^{i\theta_2} \tag{2.34}$$

We could derive $\cos(2\theta_1)$ and $\cos(2\theta_2)$:

$$\cos(2\theta_1) = \frac{\tau_1}{2r}\left(-\frac{r^2}{2\tau} - \frac{1}{\sigma}\right) \tag{2.35}$$

$$\cos(2\theta_2) = \frac{\tau_2}{2r}\left(-\frac{r^2}{2\tau} + \frac{1}{\sigma}\right) \tag{2.36}$$

where $\frac{1}{\sigma} = \frac{1}{\tau_1} - \frac{1}{\tau_2}$. We could also solve $\sin(2\theta_1)$ and $\sin(2\theta_2)$:

$$\sin(2\theta_1) = \pm\frac{\tau_1}{2r}\sqrt{\frac{4r^2}{\tau_1^2} - \frac{r^4}{\tau^2} - \frac{1}{\sigma^2} - \frac{2r^2}{\tau\sigma}}, \tag{2.37}$$

$$\sin(2\theta_2) = \pm\frac{\tau_2}{2r}\sqrt{\frac{4r^2}{\tau_2^2} - \frac{r^4}{\tau^2} - \frac{1}{\sigma^2} + \frac{2r^2}{\tau\sigma}}. \tag{2.38}$$

As r_1 and r_2 in Eqs. 2.32 and 2.33 can be described by $\cos(2\theta_1)$, $\cos(2\theta_2)$, $\sin(2\theta_1)$, and $\sin(2\theta_2)$, we can derive the expression for r_1 and r_2 again:

$$r_1 = r + \frac{\frac{2}{\tau_1}\Big(\cos(2\theta_1) + i\sin(2\theta_1)\Big)}{i(\omega - \omega_0) + \frac{1}{\tau}} = \frac{i\left[r(\omega - \omega_0)\pm\sqrt{\frac{2}{\tau_1^2} + \frac{2}{\tau_2^2} - \frac{r^2}{\tau^2} - \frac{1}{r^2\sigma^2}}\right] - \frac{1}{r\sigma}}{i(\omega - \omega_0) + \frac{1}{\tau}}, \tag{2.39}$$

$$r_2 = r + \frac{\frac{2}{\tau_2}\left(\cos(2\theta_2) + i\sin(2\theta_2)\right)}{i(\omega - \omega_0) + \frac{1}{\tau}} = \frac{i\left[r(\omega - \omega_0)\pm\sqrt{\frac{2}{\tau_1^2} + \frac{2}{\tau_2^2} - \frac{r^2}{\tau^2} - \frac{1}{r^2\sigma^2}}\right] + \frac{1}{r\sigma}}{i(\omega - \omega_0) + \frac{1}{\tau}}.$$

$$(2.40)$$

Up to now, we discussed the general case of single mode resonance with two ports. A special case is when two ports are symmetric and we ignore any energy loss, $\tau_1 = \tau_2 = \frac{\tau}{2} = \tau_0$ and $\frac{1}{\tau_{nr}} = 0$, equations 2.39 and 2.40 simplify to the same result:

$$r_s = \frac{i\left[r(\omega - \omega_0)\pm\frac{2}{\tau_0}\sqrt{1 - r^2}\right]}{i(\omega - \omega_0) + \frac{2}{\tau_0}}.$$

$$(2.41)$$

When the incident light frequency is far off this mode, the reflection coefficient converges to the background reflection coefficient r. When the incident light frequency is on resonance, the reflection coefficient is $\frac{2i}{\tau_0}\sqrt{1 - r^2}$, determined by r and radiation rate τ_0 simultaneously. In addition, when $\tau_0 \neq 0$, the mode is always critically coupled to the incident light. To see this, consider the case when $\text{Im}(r_s) = 0$, we have $(r(\omega - \omega_0) \pm \frac{2}{\tau_0}\sqrt{1 - r^2})\frac{2}{\tau_0} = 0$, therefore $\text{Re}(r_s) \propto r(\omega - \omega_0) \pm \frac{2}{\tau_0}\sqrt{1 - r^2} = 0$.

Physics picture of mode coupling on reflection response

Although we already derive the expression of r_1 and r_2, To form a clearer picture of how the coupling of the mode affects the phase response of a device, we get back to use the equation 2.32 and the expression of d_1 in equation 2.34:

$$r_1 = r + \frac{\frac{2}{\tau_1}e^{2i\theta_1}}{i(\omega - \omega_0) + \frac{1}{\tau}} := r + r_m$$

$$(2.42)$$

We can clearly see that the reflection coefficient has been decomposed into two term. The first term r is the background term, labeled the 'background' reflection where the incident frequency is off resonance. The second term is the contribution from the optical mode r_m where we call 'mode term' here. Although as shown in equation 2.35 and 2.37, θ_1 has relationship with τ_1 and τ, the amplitude of the mode term is irrelevant to this phasor term. The amplitude of the mode term determines the coupling condition between the incident light and the optical mode, shown in Fig. 2.2. Fig. 2.2 describes the trajectory of the reflection coefficient r_1 on a complex plane when the incident light frequency ω sweeps across a resonance. Since the only variable is ω, the mode term will mostly be responsible for the movement

of the reflection coefficient of port 1 r_1[1]. The undercoupled (overcoupled) curve means that the trajectory excludes (includes) the origin point in the complex plane. The background reflection coefficient, amplitude and phase of the mode term jointly determine whether the trajectory will encompass the origin point. Assuming that the radiation rate τ_1 and τ is a constant within certain frequency sweeping range, the maximum amplitude of the mode term is at the resonance frequency $\omega = \omega_0$, where $r_1 = r + \frac{2\tau}{\tau_1} e^{2i\theta_1}$. We could easily know a sufficient condition of the undercoupled regime:

$$|r| > \frac{2\tau}{\tau_1} \tag{2.43}$$

Since if the vector length of r is larger than maximum vector length of r_m, the trajectory couldn't encompass the origin point. In other words, for the optical mode in interest, if the radiation loss from one specific port takes a smaller 'ratio' of total loss than the background reflective coefficient from this port, then the mode is undercoupled.

Due to the existence of the phase term $e^{2\theta_1}$, even with condition $|r| < \frac{2\tau}{\tau_1}$ cannot guarantee an overcoupled mode. However, if we have

$$|r| \ll \frac{2\tau}{\tau_1} \tag{2.44}$$

then the trajectory will be close to a circle whose center is at the origin point. As shown in the overcoupled curve in Fig. 2.2, in this highly overcoupled regime, the overall reflection coefficient r keeps the same amplitude but has a nearly 2π phase response[2]. The overcoupled mode greatly enhances the phase response, shrinks the need of external stimuli strength, but keeps the uniformity of the amplitude response, therefore it is ideal for a phase modulator[63].

2.6 Phase enhancement using nanophotonic modes in free-space modulation

The phase response of the optical device is one of the most important topics in free-space reconfigurable devices due to its widespread applications. However, covering 2π phase response is not an easy task. For integrated photonics, the light propagation is through waveguides, and the interaction length could be easily extended to hundreds of wavelengths. However, if we don't consider any resonance

---

[1] We use the word 'mostly' because the direct scattering process will slowly change the phase of r_1 as the frequency changes and slightly contributes to the movement of the reflection coefficient.

[2] If we extend the sweeping range, the starting point and ending point will finally draw a circle and covers 2π.
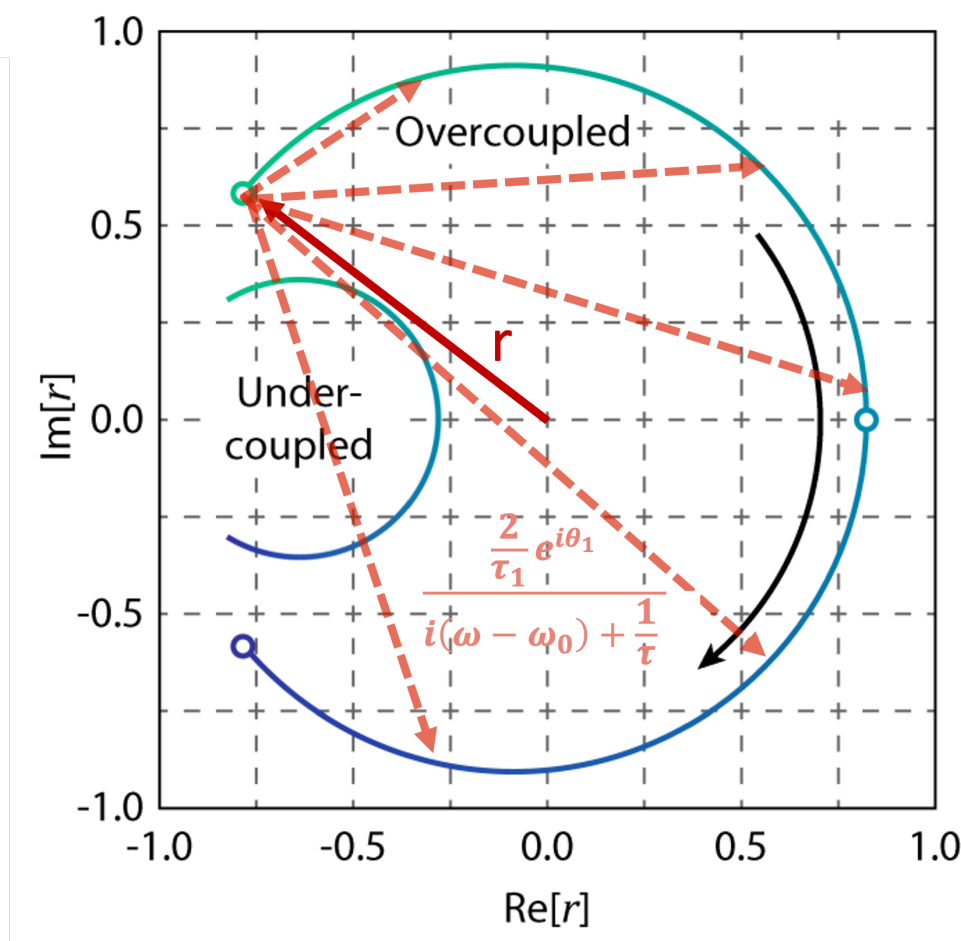
Figure 2.2: **Analysis of coupling regime using one port TCMT.** There are two curves in the figure. One represents the undercoupled mode, and the other represents the overcoupled mode. r: the red arrow, represents the background reflection term. $\frac{\frac{2}{\tau_1}e^{2i\theta_1}}{i(\omega-\omega_0)+\frac{1}{\tau}}$: the orange arrow, represents the mode term.

effect and special material-related phenomena, the interaction length of the free-space device could only be a multiple of wavelengths. Therefore, 2π phase coverage means that the external stimuli needs to generate large enough refractive index modulation (or mechanical movements), or have to couple into the eigenmodes to enhance the response. In Chapter 1, a plethora of modulation mechanisms are discussed. Many of them directly utilize the special material properties to generate large refractive index modulation, such as ENZ materials, 2D materials, liquid crystal etc. However, the consideration from nanophotonics is still required, as the use of nanophotonic modes will greatly reduce the required driving power. Therefore, knowing how to design the eigenmode and understand its effect on the input light

are essential. This section aims to provide some potential ways to improve phase response in the free-space modulation.

Mirrors

In previous section, we found out that an overcoupled mode is preferred to design a reflective phase modulator. To achieve an overcoupled mode, one of the popular methods is to use the mirror to reflect the power and block the radiation from other ports. The mirror is widely used in many works[27, 28, 64], but it greatly enhances the difficulty of fabrication. For all-dielectric metasurfaces, adding a layer of metal mirror or distributed bragg reflector (DBR) will add difficulty to the devices that require thermal processes such as annealing due to the thermal cofficient difference. Furthermore, the hybrid of metal and dielectric material will cause contamination for some fabrication equipments. Therefore, it remains a challenge to widely use mirrors in the reflective modulation devices.

Asymmetric metasurface

As we already demonstrated that a pure symmetric optical mode will be critically coupled, introducing some asymmetry is necessary to achieve an overcoupled mode. For free-space modulation, the difficulty is to break the symmetry of the two radiation ports towards top and bottom in Fig. 2.1. In a real device, the media on top of the device layer and the substrate are usually different in refractive index (unless the device is suspended), but the small asymmetry usually can't support a high overcoupled mode. Therefore, the symmetry of the device layer needs to be broken. In recent years, some works tried to develop new fabrication techniques and explore the asymmetry of the device to achieve unidirectional radiation[65] and enhanced phase response[66]. By carefully designing the shape of the device, the radiation to the unwanted port could be suppressed, then the ratio $\frac{2\tau}{\tau_1}$ could get enhanced to achieve an overcoupled mode. However, since the feature resolution is usually sub-100 nm (around 100 nm) for nanophotonic devices operating in visible(near infrared), to control the asymmetric shape of the device the fabrication resolution ends up being challenging. Overall, it is still a promising method to achieve high-performance reflective modulation device.

Low background reflection

Another way to achieve uniform phase response is to reduce the background reflection coefficient r. As shown in equation 2.42, reducing r could also help satisfy the

overcoupling condition. However, as the device material and shape is usually prede-termined, the off-resonant reflection coefficient is usually fixed. An exception case is when the device is dual-mode resonant. When one mode is leaky mode with low-Q but has strong coupling, at some wavelengths the low reflective coefficient could be treated as 'background' due to the low-Q property. If the two modes don't have intercoupling or the intercoupling effect could be ignored, then the 'background' reflection coefficient could be modulated. We will show a case in Chapter 5.

Multimodes interaction

When the metasurface is in dual-mode regime, the two modes will possibly have intercoupling that affects the total phase response. In this case, the previous discus-sion of TCMT in one mode doesn't apply, and the phase response could be greatly enhanced. For example, recent work shows that the two modes hybridation could induce 4π at a maximum[67]. One of the famous examples is the Huygen's meta-surface[68, 69]. In Chapter 3, our work also shows that the interaction between two modes will enhance the phase response.

NANOELECTROMECHANICAL TUNING OF DUAL-MODE RESONANT DIELECTRIC METASURFACES FOR DYNAMIC AMPLITUDE AND PHASE MODULATION

The material in this chapter was in part presented in [70] and covered in Dr. Hyounghan Kwon's thesis. T.Z. participated in the sample fabrication, sample measurement, data analysis and writing of the manuscript.

From the previous chapter, we know that planar all-dielectric photonic crystals and metasurfaces host various resonant eigenmodes including GMR and BIC. Engineering these resonant modes can provide new opportunities for diverse applications. Particularly, electrical control of the resonances will boost development of the applications that require tunability. Here, we experimentally demonstrate nanoelectromechanical tuning of both the GMR and the quasi-BIC modes in the telecom wavelength range. With electrostatic forces induced by a few voltages, the devices achieve spectral shifts over 5 nm, absolute intensity modulation over 40%, and modulation speed exceeding 10 kHz. We also show that the interference between two resonances enables the enhancement of the phase response when two modes are overlapped in spectrum. A phase shift of 144° is experimentally observed with a bias of 4V. Our work suggests a direct route towards optical modulators through the engineering of GMRs and quasi-BIC resonances.

3.1 Motivation

GMR has been widely used in the NEMS applications[71] since it has large coupling to free-space modes, but the quasi-BIC modes enable sophisticated control of the radiative lifetime through a symmetry-lowering perturbation[57], which provides a versatile platform for various applications such as lasers [58, 72], nonlinear light generation [59, 73], modulators [60, 74–76], and sensors [77]. As we mentioned in Chapter 1, reconfigurable metasurfaces can exploit new degrees of the freedom to manipulate light in time domain [78] and has potential to offer competitive advantages over conventional components. To achieve substantial tunability of the optical properties, the required optical response should generally be sensitive to small perturbations. Both the GMR and the quasi-BIC mode are not only highly resonant, but also efficiently coupled to free-space modes. Thus, the two resonant modes

can potentially play a pivotal role in the realization of active metasurfaces. Over the past decades, reconfigurable devices hosting the GMR have been demonstrated through various platforms, such as microelectromechanical tuning [79], thermal tuning [80], carrier injection [81], and electro-optic polymer [82]. However, to the best of our knowledge, none of the works have been related to the concept of the BIC mode. Thanks to the highly resonant characteristic of BIC mode, tuning with the quasi-BIC mode can be superior in the quality factor (Q-factor) compared to GMR in similar device size. In contrast to the devices hosting a single GMR mode, devices hosting both the GMR and the quasi-BIC modes can be beneficial in exhibiting a larger phase response. Previously, the experimental demonstration of the reconfigurable BIC mode was mostly limited to all-optical tuning [60, 74, 75] or global thermal tuning [76]. In contrast to the previous tuning methods, electromechanical tuning can be advantageous in terms of power efficiency, high modulation speed, and integration with electronic circuits [40, 41, 83]. Moreover, the previous experimental demonstrations of the reconfigurable BIC modes mostly focused on modulation of intensity rather than phase [60, 74–76]. In this work, we experimentally demonstrate nanoelectromechanical tuning of both the GMR and the quasi-BIC modes hosted by suspended silicon gratings. With a few volts, the devices achieve reconfigurable spectral shifts, large reflection modulation, and modulation speed over 10 kHz in air. It is also shown that the electrical tuning of the interference between the GMR and the quasi-BIC mode can offer continuous tuning with large phase response.

3.2 Device design

The schematic of nanoelectromechanically tunable gratings is illustrated in Fig. 3.1a. The gratings consist of two sets of pairs of doped silicon nanobars. Throughout this paper, all structures are based on arrays of 500 nm thick and 30 μm long silicon bars. We also ensure that the lattice constant of the pair of the nanobars is smaller than the wavelength of interests to avoid unwanted diffraction. Fig. 3.1b shows top and side views of illustrative schematics of the gratings. One end of the suspended nanobars is connected to the large silicon layer on which gold electrodes are deposited. To prevent bending or buckling of the suspended structures, the other end of the suspended nanobars is connected to the anchors marked in Fig. 3.1b. The gold electrodes are used to induce the Coulomb forces between the nanobars thus enabling the actuation. The silicon gratings and the electrodes are fabricated by sequential conventional nanofabrication procedures (see Method for details).
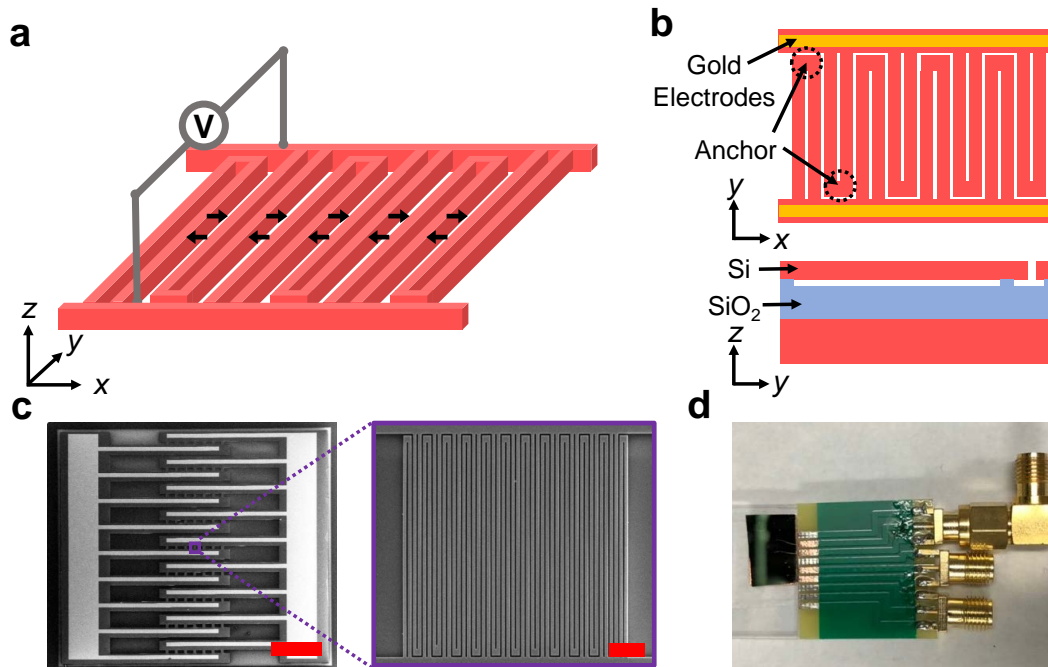
Figure 3.1: **Nanoelectromechanical tunable suspended gratings. a.** Schematic illustration of the nanoelectromechanically tunable gratings. The grating is composed of pairs of silicon nanobars. The nanobars are connected to electrodes for actuation through electrostatic force. Black arrows show the directions of the actuation. **b.** Schematic illustration of top (top) and side (bottom) views of the grating. Top: Two gold electrodes are deposited on top of the doped-silicon layers. Anchors and the gold electrodes are marked. Bottom: Buffered silicon oxide layer under the silicon nanobars is partially etched by 300 nm for the suspension while the anchors are supported by the oxide layer. **c.** Scanning electron microscope images of the fabricated devices. Left: An array of the gratings and two gold electrodes are shown. One of the gratings is marked by a purple box. Right: Zoom-in scanning electron microscope image of the grating marked with the purple box in the left image. The grating consists of 23 pairs of silicon nanobars. Scale bars in left and right denote 500 μm and 5 μm, respectively. **d.** Optical images of the fabricated device. The device is wire-bonded to a custom printed circuit board that is connected to an external source by a SMA cable.

Fig. 3.1c shows the scanning electron microscope images of the fabricated device, which consists of two electrodes and an array of the gratings. The device is wire-bonded to a custom-made printed circuit board so that it allows for connection to an external voltage source. The optical image of the fabricated device and the printed circuit board is shown in Fig. 3.1d.

3.3 Optical characterization of the gratings

First, the optical characterization of the gratings is performed. The finite-sized gratings are known to host both GMR and quasi-BIC modes that allow for coupling with free-space light [52, 84]. Fig. 3.2a shows calculated reflection spectra for 6° tilted TE-polarized input light (See section 3.7 for details). With a lattice constant of 700 nm, the widths of the nanobars vary from 420 nm to 480 nm. In other words, the coupling is achieved by breaking of the even symmetry of the incident beam. Moreover, it is worth noting here that breaking the odd symmetry of the mode can also result in efficient coupling at normal incidence [54]. Two distinct resonant modes can be found. One mode at the shorter wavelength is the leaky GMR mode and the other mode at the longer wavelength is the quasi-BIC mode. We fabricated and measured seven corresponding devices with nanobar widths varying from 420 nm to 480 nm by 10 nm. A custom-built microscope setup is utilized to measure the reflection spectra of the grating samples (See section 3.7 for details about the measurement). The spectrum is normalized by the reflection from the gold layer to estimate absolute reflection and remove fluctuations resulting from polarization variations of the input light. Thus, the actual reflection values should be a few percentages lower than the plotted reflection spectra presented in this paper considering the reflection loss of the 95 nm thick gold layer. The measured reflection spectra for the six degree tilted TE polarized light are plotted in Fig. 3.2b showing good agreement with the simulation results in Fig. 3.2a. The black and red circles show the positions of the GMR and quasi-BIC modes, respectively. Furthermore, three examples of the measured reflection spectra are shown in Fig. 3.2c. As shown in Fig. 3.2b, two distinct modes, GMR and quasi-BIC mode, are observed at the three spectra shown in Fig. 3.2c and also marked by black and red circles. While broad dips below 1510 nm show dips of the low-Q fano-shape GMRs, other narrow dips over 1520 nm represent high-Q quasi-BIC modes. If the incident angle decreases from 6° to 0°, the BIC will be protected by symmetry [52, 54]. As a result, the radiation channels of the quasi-BIC mode are gradually closed, which increases Q-factor and decreases the amplitude of the resonant signal (see Fig. 3.A.2 for two
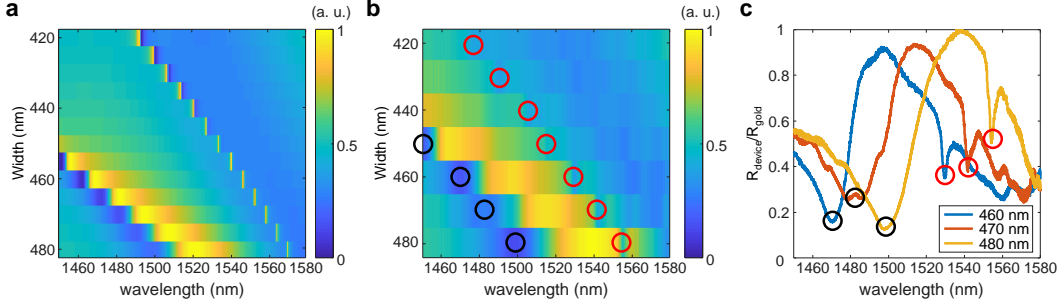
Figure 3.2: **Calculated and measured reflection spectra of the GMR and the quasi-BIC modes hosted by the gratings. a.** Calculated reflection spectra (TE-polarized light) for gratings where widths of the nanobars vary from 420 nm to 480 nm by 5 nm. Period of the grating and incidence angle of light are 700 nm and 6 degree, respectively. **b.** Measured reflection of TE-polarized light for the fabricated gratings with 6 degree tilted incident light. The reflection is normalized by the measured reflection from the gold electrode. The widths vary from 420 nm to 480 nm by 10 nm. **c.** Three example spectra of the measured reflection spectra shown in b. The widths of the nanobars are 460, 470 and 480 nm and noted in legend. In b and c, black and red circles denote resonances of the GMR and the quasi-BIC modes, respectively.

measured reflection spectra for normal and 6° tilted TE-polarized input light).

3.4 Device modulation characteristics

To demonstrate nanoelectromechanical tuning of the devices, static bias voltage is applied to the electrodes and the induced changes in the optical reflection are evaluated. The shape and position of both the GMR and the quasi-BIC mode highly depend on the gap size between the nanobars, which can be continuously controlled as a function of the external bias. Specifically, in the configuration shown in Fig. 3.3a every two nanobars are connected to one electrode and biased by an external source or ground, so bars connected to different electrodes will attract each other. In Fig.3.3a, g_1 (g_2) is the gap between the nanobars having different (same) voltages. As the external bias is applied, g_1 and g_2 will decrease and increase, respectively. Consequently, this nanomechanical actuation enables continuous shifts of the resonances. It is worth noting here that similar laterally movable actuators have been investigated with single-mode low-Q grating resonators [40, 85]. The measured reflection spectra under several bias voltages are shown in Figs. 3.3b and 3.3c. For the devices used in Figs. 3.3b and 3.3c, it should be mentioned that g_1 and g_2 are adjusted in the fabrication process to make g_1 smaller than g_2 such that the nanoelectromechanical tuning of the gaps efficiently results in a large shift

of the resonances (see Table 3.A.1 for the detailed information about the device). In Figs. 3.3b and 3.3c, the static bias causes the red shift of the GMR mode and blue shift of the quasi-BIC mode. The observed directions of the spectral shifts show good agreement with the simulated results (see Fig. 3.A.3 for the numerical investigation about spectral shifts of the resonances induced by the actuation). With the external bias of 7 V, the peak shifts of the GMR and the quasi-BIC mode shown in Fig. 3.3b are as large as 5 nm and -6 nm, respectively. The absolute spectral shifts over 5 nm indicate that the required Q-factor for the spectral shift corresponding to the bandwidth of the resonance is around 300, which is readily achievable with quasi-BIC mode resonance even in a small array [73]. In general, the large spectral shift is beneficial in terms of robustness, stability, and operating bandwidth. To illustrate the capability of reflection intensity modulation of the presented devices, the absolute changes in reflection over spectrum are plotted in Figs. 3.3d and 3.3e. In Fig. 3.3e, the maximum absolute change in the reflection is as high as 0.45. As we treat the reflection of the 95nm thick gold electrode as 1 and use it as the normalization constant, the reflection change induced by the nanomechanical tuning will be larger than 0.4 if a few percentage loss from the gold surface is considered. It is also worth noting that the modulation can be readily improved by increasing the coupling between the resonant mode and the free space light by using the structural symmetry-breaking perturbation. Moreover, the measured values are not the real limit but the lower bound of the performance as the spectral shifts and the intensity modulation are measured with the external bias below pull-in voltage. The temporal and frequency responses of the gratings are investigated in air. To explore temporal responses first, a periodic square-wave signal with a modulation frequency of 3 kHz, amplitude of 6V, and duty cycle of 0.5 is applied to the electrodes (see Supporting Information for details). The device used for Fig. 3.3b is measured with input light at 1562 nm. The measured output signals are plotted in Fig. 3.4a having the corresponding frequency of 3 kHz. Fig. 3.4b shows measured rise time (up to 90% power) and fall time (down to 10% power) of 41 and 66 μs, respectively. The rise and fall times indicate the speed limit of 15.2 kHz which is dominantly limited by air damping. The frequency response is measured and plotted in Fig. 3.4c showing the 3 dB frequency of 25 kHz. In addition, the mechanical resonant frequency in vacuum can be calculated by COMSOL$^{®}$ (see Method for details). The mechanical resonance frequency of the devices presented in this paper is estimated to be around 4.5MHz that could be observed with proper vacuum packaging [40, 86]. Thus, our device has the potential to operate in a few MHz regime with decreased driving
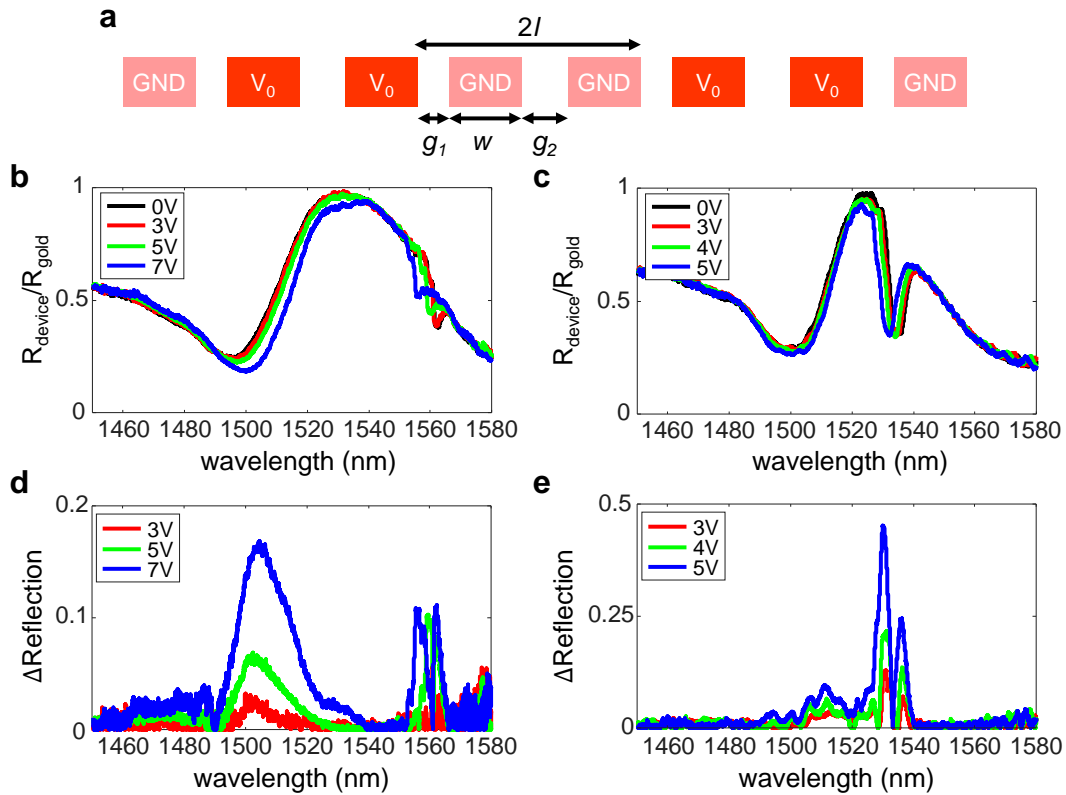
Figure 3.3: **Nanoelectromechanical tuning of the resonances for intensity modulation. a.** Schematic illustration of an array of pairs of the silicon nanobars. The grating consists of periodic pairs of the silicon bars. Pink and red colors represent ground, GND, and external bias, V_0, respectively. Parameter definitions are shown in the illustration where l, w, g_1, and g_2 are the lattice constant of the grating, the width of the nanobar, the gap between the nanobars having a different bias, and the gap between the nanobars having the same bias, respectively. **b** and **c.** Measured reflection spectra of TE-polarized lights for two different structures (see Table S1 for detailed design parameters). The spectra are measured under four different biases and plotted in different colors. The applied bias for each color is shown in legends. **d** and **e.** Spectra of absolute modulation in reflection calculated from b and c. The applied bias for each color is shown in legends.
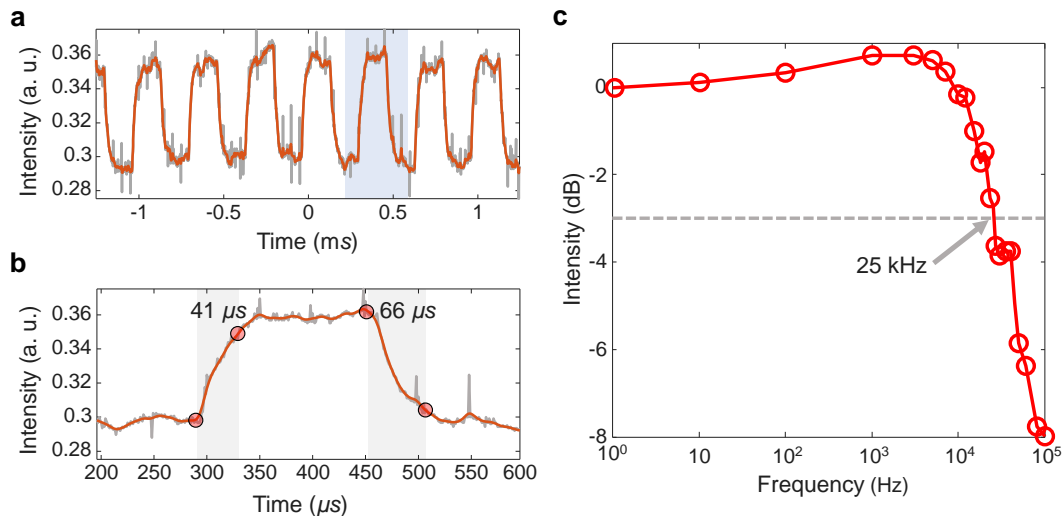
Figure 3.4: **Temporal and frequency response of the nanoelectromechanically tunable grating a.** Measured time response of the grating with a 3-kHz square wave signal of which duty cycle and amplitude are 0.5 and 6V, respectively. Raw and filtered reflection signals are plotted by grey and orange curves, respectively. **b.** Magnified temporal signal marked by sky-blue color in a. Measured rise and fall times are 41 and 66 μs, respectively. **c.** Measured frequency response of the grating. The 3 dB frequency is 25 kHz.

voltage.

3.5 Enhanced phase response by dual-mode interference

Finally, we investigate enhanced phase modulation based on the interference of the two resonant modes. Temporal coupled mode theory can generally describe the optical response of eigenmodes through ports [61], where we described the general framework in Chapter 2. With coupled mode equations describing a single mode and a single port, it is known that large phase shift close to 2π can only be achieved when the resonant mode is over-coupled to the input port [64, 87, 88]. Specifically, coupling coefficient between the mode and the input is larger than intrinsic loss of the mode in the over-coupled regime [64, 88]. As also mentioned in section 2.6, the over-coupling is often achieved by the presence of the bottom mirrors that ensure the radiation of the mode is matched with the direction of the input [64, 88]. The silicon nanobars shown here are surrounded by air, so the structure is nearly symmetric in z-axis[1]. This nearly symmetric environment results in similar radiation in +z and -z directions, which hinders the over-coupling of light through one direction. As a

---

[1]The existence of the substrate breaks the z-symmetry.

result, using a single GMR or quasi-BIC mode hosted by the presented devices, it is very challenging to achieve large phase modulation of reflected light if there is no bottom mirror (see Fig. 3.A.4 for numerical study about the phase response of the single BIC resonance). We also discussed the potential ways to solve this problem in section 2.6 without a bottom mirror. If there are multiple resonances in the frequency range of interest, the overall reflected phase response is affected by interference effects of the multiple resonant modes. Thus, the interference of dual modes can enable large phase shifts with non-zero reflection, indicating a overcoupling regime. Fig. 3.5a shows calculated reflection intensity and phase spectra of a device for which the design parameters are adjusted to place the narrow quasi-BIC mode resonance near the peak of the broad GMR (see Table 3.A.1 for detailed designs of the device). In Fig. 3.5a, the minimum reflection at the resonance is 0.237 and the reflected phase shows strong phase response close to 2π. To numerically show the phase modulation via nanomechanical tuning, expressed by $g_2 - g_1$, the spectra of the reflected phase are plotted in Fig. 3.5b as a function of $g_2 - g_1$. In Fig. 3.5b, the mechanical tuning results in continuous blue-shift of the resonance while the strong phase response remains at the resonance. The blue-shifts of the quasi-BIC mode shown in Fig. 3.5b agree with the experimental observations in Figs. 3.3b and 3.3c. For the experimental demonstration, a new device is fabricated with the corresponding design parameters and its reflection spectra are plotted in Fig. 3.5c. The reflection spectra in Fig. 3.5c show electrical tuning of the resonances and a good agreement with the spectra shown in Fig. 3.5a. The measured Q-factor of the device used in Fig. 3.5c is ~244, which is less than simulated Q factor of ~1836. The difference could be explained by the small size of the array and imperfect fabrications. To experimentally characterize the phase response of the device used in 3.5c , we used a Michelson-type interferometer setup (see Fig. 3.A.1). Due to the small size of the device, the incident laser beam illuminates the entire grating and the gold electrode at the same time and the interference patterns on both interfaces are simultaneously collected by a camera. At the resonant wavelength of 1556 nm, the fringes on the grating are shifted by external biases from 0 V to 4 V while the fringes on the electrode are unchanged (see Fig. 3.A.5 for the details). The induced phase modulation is estimated by the observed shifts of the fringes on the grating and plotted in Fig. 3.5d. The largest phase shift of 144° is achieved at the external bias of 4V, which is smaller than the simulation result shown in Figs. 3.5a and 3.5b. The deviation from the simulation is primarily due to limited free-space coupling to the quasi-BIC mode. For example, the absolute reflection
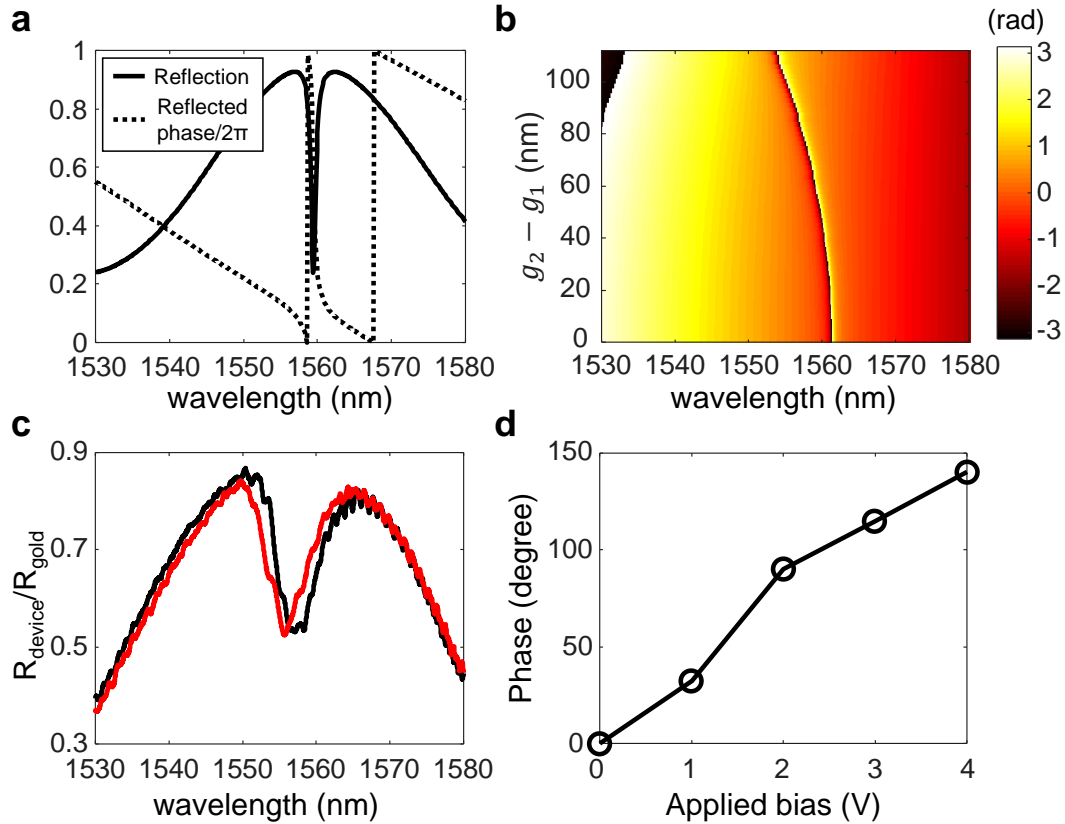
Figure 3.5: **Overlap of the GMR and quasi-BIC mode resonances for enhanced phase modulation. a.** Calculated reflection and reflected phase spectra. The quasi-BIC mode is placed near the peak of the GMR. **b.** Calculated spectra of reflection phase. The spectra are plotted as a function of the nanomechanical tuning, $g_2 - g_1$. **c.** Measured reflection spectra with applied biases of 0V (black) and 4V (red). **d.** Measured phase shift of the metasurface at the wavelength of 1556 nm as a function of the applied biases from 0V to 4V.

dip shown in Fig. 3.5a is much smaller than the measured dip in Fig. 3.5c indicating imperfect coupling to the quasi-BIC mode. We believe that this inefficient coupling dominantly results from the finite size effect. Although it might be expected that the introduction of a spatially varying perturbation for each pair of the nanobars could allow electrically controlled wavefront shaping, it is worth explicitly noting that the presented resonance mode doesn't support efficient wavefront shaping at subwavelength scale. The introduction of the spatially varying perturbations at subwavelength scale may severely break the periodic condition of the structures, which the two modes necessitate to resonate. Thus, the interference effect of the two resonant modes is more suitable for spatial light phase-modulators having a pixel pitch of tens of micrometers than the pixel pitch of subwavelength scale.

However, we expect that electrically controlled wavefront shaping in subwavelength or wavelength scale is possible with judicious engineering of various resonance modes hosted by an array of dielectric nanostructures [57, 76, 89, 90].

3.6 Conclusion

In this chapter, we demonstrate nanoelectromechanical tuning of the leaky GMR and the quasi-BIC modes hosted by suspended silicon grating structures. With an external bias below 7 V, the devices experimentally achieve a spectral shift of the resonance over 5 nm, intensity modulation exceeding 40%, and modulation speed over 10 kHz in air. The required electrostatic bias can be further decreased by choosing the resonant modes that host large electric fields in the gaps [91]. In addition, co-optimization of both mechanical and optical properties is expected to improve the operating speed in air. With proper vacuum packaging, the devices may operate at high mechanical resonant frequency around several MHz. Moreover, we experimentally show that the interference between the GMR and quasi-BIC mode can enhance the phase response. The phase shift of 144° is measured at the external bias of 4V. Engineering of the resonant modes via structural tuning will improve the phase responses and enable dynamic wavefront shaping at subwavelength scale. Thus, this work paves the way of nanoelectromechanical dynamic dielectric metasurfaces towards diverse applications such as spatial light modulators, lasers, nonlinear or structured light generation, pulse controller, polarization converters, and compact spectrometers for bio-sensing.

3.7 Appendix

Simulation and design

The reflected spectra of the gratings with 6° tilted incidence light were calculated using the rigorous coupled wave analysis technique[92]. Assuming the infinite length of silicon nanobars, 2D simulations were performed. The silicon, air, and silicon oxide layers on a silicon substrate were 500nm, 300 nm, and 2700 nm thick, respectively. Refractive indices of Si and SiO$_2$ for the telecom wavelength in the simulation were 3.4 and 1.45, respectively. The width and lattice constant were varied in the simulation to achieve the desired reflection spectra (see Table S1 for detailed information about the design parameters).

The mechanical resonance frequency is calculated by a commercial software based on the finite element method, COMSOL®. The eigenfrequency of the Si bar is extracted assuming that both ends of the suspended nanobars are fixed. In the

mechanical simulation, Young's modulus and density values for silicon were 170 GPa and 2329 kgm^{-3}, respectively.

Device fabrication

The devices are fabricated using a silicon-on-insulator wafer with a device layer of 500 nm and a buffered oxide layer of 3 μm on a 1 mm thick silicon substrate. The fabrication includes two sequential e-beam lithography steps, the first one for the grating structures and another for the electrodes. For both lithography steps, a ~300-nm-thick positive electron resist (ZEP-520A, Zeon) is spin-coated on the device. The patterns are generated by 100 kV electron beam exposure (EBPG5200, Raith GmbH), and the resist is developed in a developer solution (ZED-N50, Zeon). For the silicon grating structures, the ZEP resist is utilized as a soft mask to etch the silicon device layer and then removed by remover PG (Microchem). Next, the electrodes were patterned by electron beam lithography, the deposition of chrome and gold (5nm and 95nm) layers, and liftoff. Buffered hydrofluoric acid is exploited to etch the buffered oxide layer under the gratings. The time of the under-cut process is carefully controlled such that the anchors are supported by the SiO$_2$ while the gratings are fully suspended. The device is dried by a critical point dryer. Finally, the device is bonded to a custom printed circuit board using a wire bonder (WestBond 7476D).

Measurement procedure

All of the reflection spectra presented in this paper are characterized using the set-ups shown schematically in Fig. 3.A.1[64]. A tunable laser (Photonetics, TUNICS-Plus) is used as the light source and the wavelength of the light is tuned from 1450 nm to 1580 nm. We use a beam splitter in front of the fiber collimator (Thorlabs, F260FC-1550) to capture the power from the source and send the light to the sample. For reference, the power from the source is captured by a InGaAs detector (Thorlabs, PDA10CS). Due to variation in polarization states from the laser, a quarter waveplate in front of a polarization beamsplitter (PBS) is used to prevent low transmission through PBS at specific wavelengths, increasing signal-to-noise ratio over the entire spectrum. The PBS, a half waveplate (HWP), and a polarizer are inserted to set the polarized state of the incident light to TE polarization. The sample at the object plane is imaged by a 20× infinity-corrected objective lens (Mitutoyo, M Plan Apo NIR) and a tube lens with a focal length of 200 mm. As the tube lens and the objective lens are forming a 4-f system, the movement of the tube lens in x-axis

enables to adjust the angle of illuminated light. At the image plane, a pinhole with a diameter of 400 μm is inserted to select a region of interest with a diameter of 20 μm in the object plane. The spatially filtered light was either focused onto another InGaAs detector for the measurement of the spectra, or imaged on an InGaAs SWIR camera (Goodrich, SU320HX-1.7RT) using relay optics. All spectra in this paper were obtained by dividing the signal from the sample by the signal from the sources. Due to different input polarization states, the incidence power onto the sample varies in different wavelengths. Thus, the spectra are further normalized by the spectra from the gold electrode. For the measurement of dynamic responses shown in Figs. 3.3-3.5, bias voltages, both DC and AC, are applied with a function generator (FeelTech, FY6600-60M).

To measure the phase response shown in Fig. 3.5d, we use a Michelson-type interferometer setup. A part of the setup marked by a black dashed box in Fig. 3.A.1 is only utilized for the phase measurement. Specifically, the reference beam interferes with the reflected beam of the sample and forms fringe patterns at both image and camera planes, enabling the measurement of reflected phase as a function of applied biases from 0V to 4V.

Figure	$2l$ (nm)	w (nm)	g_1 (nm)	g_2 (nm)
Fig. 3.3b,d, and 3.4	1400	495	245	165
Fig. 3.3c,e	1320	495	185	145
Fig. 3.5	1332	494	144	200
Fig. 3.A.2a	1400	460	240	240
Fig. 3.A.2b	1400	480	220	220

Table 3.A.1: **Design parameters for all nanomechanical gratings in this work.** $2l$: Lattice constant for a pair of the silicon bars. w: Width of the silicon bar. g_1: Gap between the silicon bars having voltage difference. g_2: Gap between the silicon bars having the same voltage.

The angle sensitivity of the reflection spectra

In this chapter, the quasi-BIC mode we use is origin from the symmetry-lowering perturbation. More specifically, when the incident light angle is normal, the electric and magnetic incident field is odd under C_2, while the BIC mode is even under C_2. The preserved symmetry prohibits the coupling between the incident light and the mode[52], therefore there isn't any resonance in the reflection spectra, as shown in
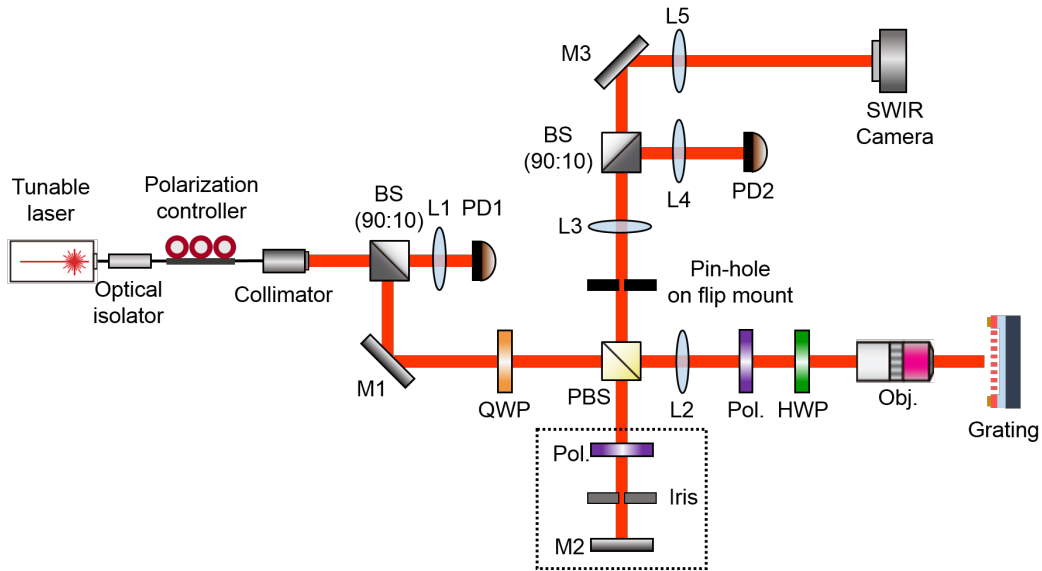
Figure 3.A.1: **Schematic illustration of the experimental setup.** Red lines represent the paths of the light. To achieve the reflection spectra of the TE-polarized input light, Pol. and HWP in front of the objective lens are aligned to 45 and 67.5 degree, respectively. A black dashed box represents optical elements exploited to generate reference beam for the phase measurement shown in Fig. 3.5d of the main text and Fig. 3.A.5. Pol.: linear polarizer. BS: beamsplitter. PBS: polarizing beamsplitter. L: lens. PD: photodetector. M: mirror. QWP: quarter waveplate. HWP: half waveplate. Obj.: microscope objective lens. SWIR camera: short-wave infrared camera.

the red line of the Fig. 3.A.2. The 6° tilt angle breaks this symmetry protection and activates the coupling between the incidence light and the mode. Therefore, the high-Q resonance shows up in the blue line of the Fig. 3.A.2. The quality factor could be controlled by the tilt angle, but decrease the coupling will also decrease the amplitude of the resonance. We choose 6° as a balance of the quality factor and the resonance amplitude.

Numerical investigation related to spectral shifts of the resonances induced by actuation

To confirm that the observed resonance in the experiment matches with the resonance in the numerical simulation, we also perform the numerical simulation with varied parameters. With increase of $g_2 - g_1$, the GMR and quasi-BIC mode show red and blue shifts in Fig. 3.A.3, respectively. The shift matches the observation in Fig. 3.2c. Therefore, the experimental and numerical results match each other.
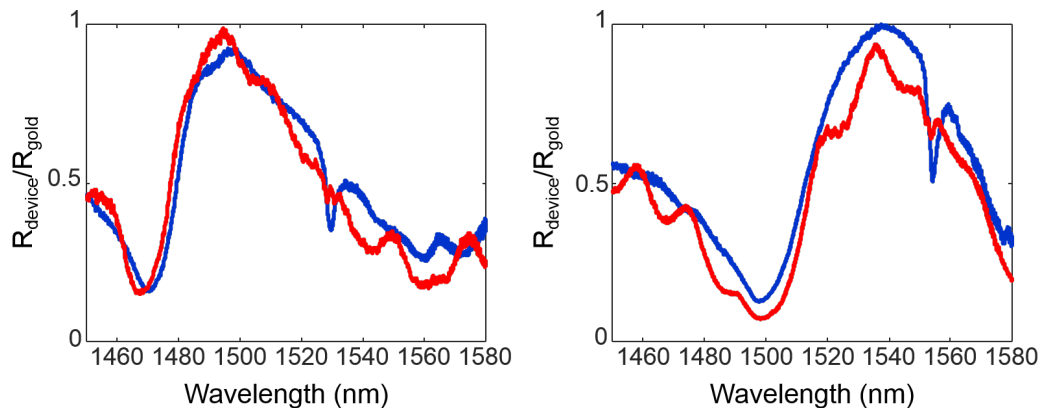
Figure 3.A.2: **Measurement of angle-sensitive reflection spectra. a** and **b.** Red and blue curves show the reflection spectra for normal and 6 degree tilted TE polarized incident light, respectively. With 500 nm thickness and 700 nm period of the lattice, the design parameters of a and b are shown in Table 3.A.1.
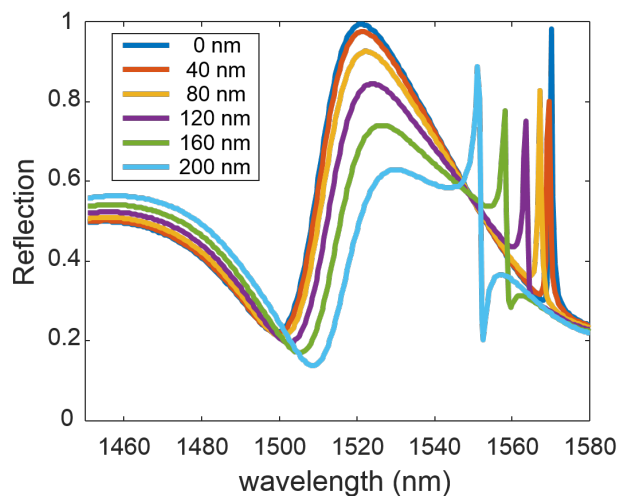
Figure 3.A.3: **Numerical investigation related to spectral shifts of the resonances induced by actuation.** The spectra are simulated under six different values of $g_2 - g_1$ and plotted in different colors. The value of $g_2 - g_1$ for each color is shown in legends. The width and lattice constant of the device are 480 nm and 700 nm, respectively.

Calculated reflection and reflected phase spectra for single BIC resonance

To directly prove that the two mode coupling increases the phase response, we also calculate the numerical phase response when the GMR and quasi-BIC modes are not resonant at the same frequency. The results is plot in Fig. 3.A.4. The phase response due to the single quasi-BIC resonance is only 55°. Therefore, the effect of dual-mode resonance increases the phase response by nearly three times.
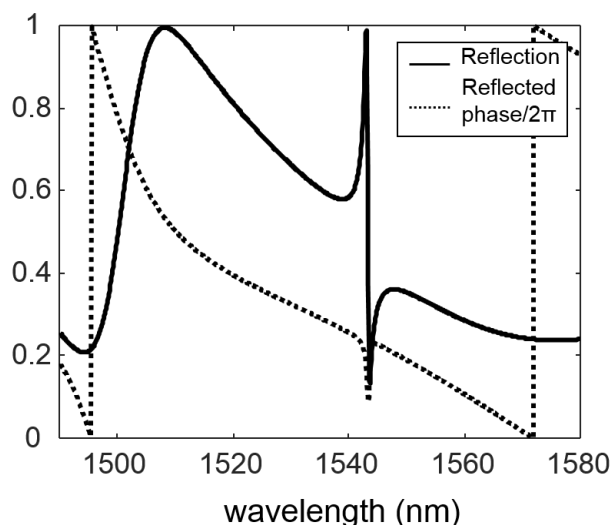
Figure 3.A.4: **Calculated reflection and reflected phase spectra for single BIC resonance.** The quasi-BIC mode is apart from the peak of the GMR. At the resonance wavelength of 1543 nm, the calculated phase response of the quasi-BIC mode is smaller than 55 deg. The width and the lattice of the structures are 475 nm and 666 nm, respectively.

Fringe analysis for phase response measurement

The phase response measurement is performed by the inteferometer setup. The interferometer part of the setup is shown in the dashed box of the Fig. 3.A.1 and described by the measurement procedure. The original light trace serves as one arm of the interferometer, and the dashed box serves as another arm. The two beams form fringes in the camera, and when the device under test has phase response, the fringe position will move accordingly. The shift of the fringe as a ratio of the fringe period is the phase change of the device under biased voltage. As shown in Figs. 3.A.5b and c, the fringes are not shifted on the electrode but on the gratings under different external biases. The phase responses under the external biases are calculated by using the corresponding shifts of the fringes on the grating shown in

Fig. 3.A.5c. We used the formula $2\pi\frac{\delta w}{w_0}$ to calculate the phase shifts, where δw is the averaged shift of the fringes in the unit of camera pixel number, and w_0 is the pixel number of a period of the fringe. The measured w_0 is 10 camera pixels. Finally, the phase shifts are averaged from all five pictures in Fig. 3.A.5c and plotted in Fig.3.5d.
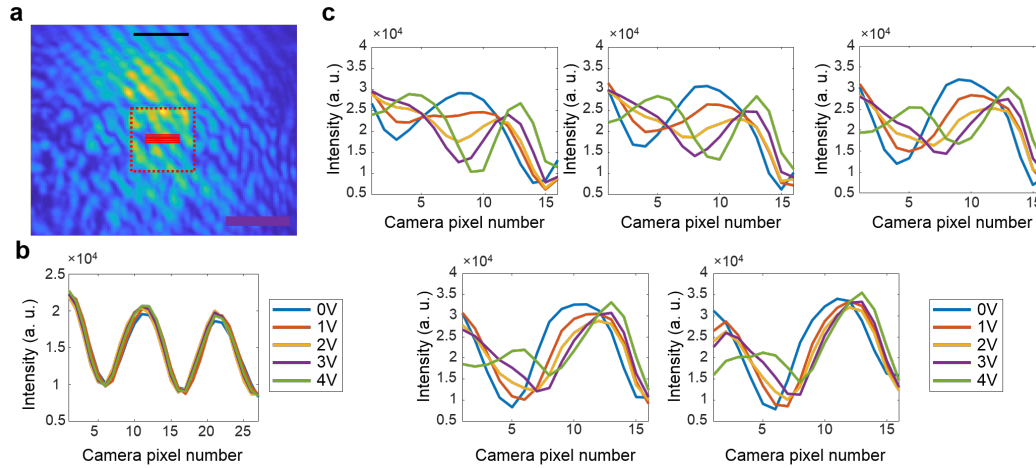
Figure 3.A.5: **Fringe analysis for phase response measurement. a.** A camera image of the fringes on the measured device. The red dashed square shows the position of the measured device. Five solid red lines inside the red square and a black solid line show the places that we use to analyze the phase responses on the grating and the electrode, respectively. Scale bar denotes 30 μm. **b.** The fringe patterns on the electrode under the external biases from 0V to 4V. The fringe patterns are captured along the black solid line in a. The fringes are nearly identical and not shifted for the different voltages. **c.** The five fringe patterns on the grating under the external biases from 0V to 4V. The fringe patterns are captured at the center of the grating along the five red solid line in a. The five plots show the clear shifts of the fringes. In b and c, *x*- and *y*- axes are pixel number and pixel value of the camera, respectively. The applied biases for all colors are denoted in outsets in b and c.

C h a p t e r   4

NANOELECTROMECHANICAL TUNING OF HIGH-Q SLOT METASURFACES

The material in this chapter was in part presented in [93].

Nanoelectromechanical devices have been used widely in many applications across photonics, electronics and acoustics. Their incorporation into metasurface systems could be beneficial in designing new types of active photonic devices. Here, we propose a design of active metasurfaces using a nanoelectromechanical system (NEMS) composed of silicon bars which operates under CMOS-level voltage and achieves phase modulation with wavelength-scale pixel pitch. By introducing a perturbation to the slot mode propagating between the silicon bars, the device operates in a high-Q regime, making the optical mode highly sensitive to mechanical movement. Over 12 dB reflection modulation is observed by full-wave simulation and over 10% is achieved in the proof-of-concept experiment both under CMOS-level voltage. We also simulate a device with 1.8π phase response using a bottom gold mirror. Based on this device, a 3-pixel optical beam deflector is shown to have 75% diffraction efficiency.

4.1   Motivation

In Chapter 3, we successfully achieved enhanced phase response by utilizing dual-mode metasurface. However, there are a few disadvantages of this approach. First, the driving voltage is around 5-7V in the experiments. If the NEMS system could reduce the voltage to CMOS-level[1], they could seamlessly integrate with many digital driving chips and have widespread applications. Second, the requirement of the dual-mode resonance strongly limits the possible geometry of the NEMS gratings. Since these two modes have to have similar eigenfrequencies, the shape of the metasurfaces could only have several distance choices and we couldn't arbitrarily choose the resonant wavelength. Third, although the phase response is enhanced up to 144°, the phase coverage is below π and therefore more sophisticated spatial phase modulation couldn't be achieved. Fourth, the GMR and quasi-BIC have a strong requirement of the periodic condition in both x and y directions and need

---

[1]In CMOS gates, the "high" voltage is between 3.5V and 5V, and "low" voltage is between 0V and 1.5V.

large device size to satisfy this periodic condition. Therefore, in the device of Chapter 3, the footprint is around $50 \times 30 \mu m^2$. The pixel size is large and is difficult to shrink due to the intrinsic operating principle. Because of all these reasons, the beam steering in wavelength-scale pixel size within CMOS-level voltage has not been realized yet.

In order to demonstrate active photonic devices operated at CMOS-level voltage, it is advantageous for the NEMS structure to operate using a high-Q optical resonance. As mentioned in Chapter 2, high-Q resonant metasurfaces have been demonstrated in various systems and in many different ways [54, 94, 95]. By breaking the symmetry of a bound state, the radiation channel of the mode can be controlled by the perturbation strength, and thus arbitrary Q could be achieved. This high-Q perturbation paves the way to further reduce the driving voltage of the nanoelectromechanical metasurfaces. Moreover, we found that perturbing the slot mode leads to a larger sensitivity of the optical modes with mechanical movements. Here, we theoretically and experimentally demonstrate a nanoelectromechanical metasurface using a perturbed slot waveguide, which leads to high tunability under CMOS voltages. Over 12 dB and over 10 % modulations are observed in simulation and experiment respectively. Thanks to the locally resonant nature of the slot mode, the devices can locally control the optical response at the level of one slot. To showcase this property, we demonstrate a beam deflector with 3 pixel periodicity that achieves 75% diffraction efficiency.

4.2 Principle of the slot modes

The slot mode represents the eigenmodes where the electric field is confined within the low refractive index media between the high refractive index media [96]. When the dimension of low refractive index media is small, the electric field will be greatly enhanced due to the discontinuity of the high-refractive-index-contrast interfaces. Over the last two decades, the slot modes have been widely explored [97, 98], which enabled applications in sensors [99] and modulators [100]. However, the slot modes have been rarely used in free-space optics since they cannot couple to the free-space wave due to momentum unmatching. A small perturbation could change the scenario and transform the slot mode into a free-space coupled resonance. When periodic perturbations are applied to the waveguide, the guided mode starts to radiate through the free-space channel [94, 95]. To illustrate the proposed concept, we first consider an infinite number of silicon bars in air, periodically placed in the *x*-direction and infinite long in the *y*-direction. The two bars within a period are close to each
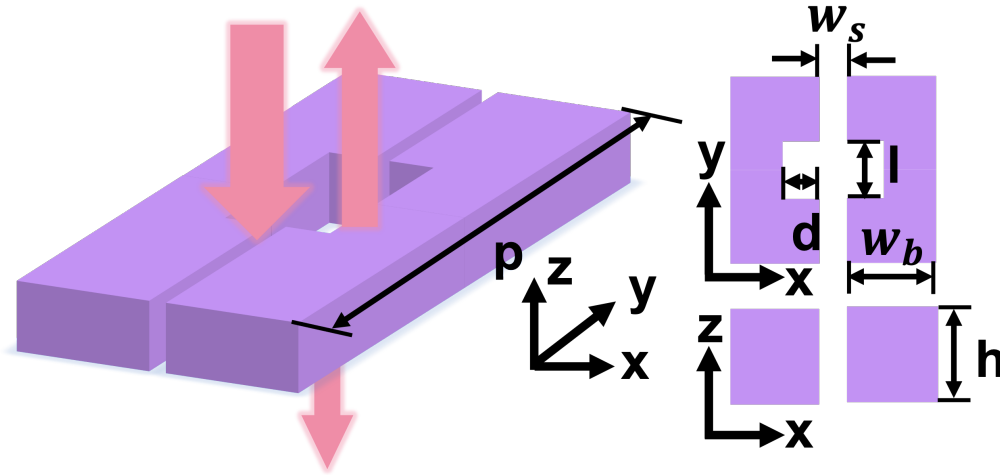
Figure 4.1: **Geometric diagram of a pair of infinite-long slots with periodic notches.** Left: perspective view. Top right: top view. Top bottom: front view. The definitions of design parameters are noted: p is the period of the notches. d and l are the width and length of the notches. h is the height of the silicon bar. w_s is the slot width between the bars with different voltages, and w_g is the gap between the bars with the same voltages.

other to form a slot. A period of the structure is drawn in Fig. 4.1, including the perspective view and relevant cross-sections. Before we introduce the perturbation, we first investigate the dispersion relationship of the slot mode shown in Fig. 4.2.

A typical dispersion relation is shown in Fig. 4.2a, where the periodicity is introduced fictitiously (i.e. there are no notches) in the periodic boundary conditions of the simulation. Fig. 4.2b-i presents the electrical field profiles of multiple points in Fig. 4.2a. At $k_\parallel = k_y = 0$, two degenerate slot eigenmodes are observed, as shown in Fig. 4.2(b) and (c), respectively. These profiles exhibit a $\pi/2$ phase offset along the y-axis, indicating standing wave modes. The formation of these standing waves arises from the degeneracy of the slot modes at $k_\parallel = 0$. Under this fictitious periodic condition, two bands converge at the same wavelength, $\lambda = 1.493\mu m$, and the structure supports two orthogonal slot eigenmodes represented by orthogonal standing wave modes.

When $0 < k_\parallel < 1$, the eigenmodes split into two branches at longer and shorter wavelengths, respectively. Fig. 4.2(d) and (e) illustrate the mode profiles for longer and shorter wavelengths, specifically when $k_\parallel = \pi/(2p)$ (where p denotes the period of the fictitious perturbation, as shown in Fig. 4.1b). The constant amplitude of E_x and the periodic variation of $\text{Re}(E_x)$ in both modes confirm their nature as

propagating modes along the slot. Within the simulation region ($-500nm < y < 500nm$), the mode at the longer wavelength (e) exhibits more periods compared to the mode at the shorter wavelength (d), while both modes satisfy the boundary Floquet condition along the y-axis.

Finally, when $k_\parallel = \pi/p$, the boundary condition is the same as $k_\parallel = 0$, except for a phase shift of π. In this case, two degenerate eigenmodes can be identified at different wavelengths. Fig. 4.2(f)-(g) and (h)-(i) display the two sets of degenerate modes, respectively. Similar to the $k_\parallel = 0$ case, these modes are standing waves and are formed by two propagating modes.

Notches are introduced in the design in order to create a periodicity in the y direction and wrap the dispersion relation of the slot modes. We focus on the case where $k_\parallel = k_y = 0$, and the mode profiles in Fig. 4.2b-c, indicating that two guided waves form a standing wave mode under this fictitious periodic condition, matching the $k_\parallel = k_y = 0$ momentum of the incident plane wave propagating along $-z$. Thus, when we create notches at this fictitious period p, the normally incident light will start to couple into the slot mode. As a result, the high-Q resonance will appear near the frequency of the degenerated slot mode. It is worth noting that similar designs were proposed before [101], but our main purpose here is to utilize these defect modes to achieve high-Q resonance in the NEMS system. When the notch depth increases, the perturbation strength increases thus decreasing the quality factor. Fig. 4.3a shows the reflection spectra of the slot resonances for several different notch sizes, and Fig. 4.3b summarizes their Q-factors. We could examine the field profiles of eigenmodes for different notch sizes in Fig. 4.3c. As the notch size increases, although the field is still enhanced for multiple times and mostly confined in the slot region, the field enhancement within the slot (at $z = 0$) decreases, explaining the observed decrease in the quality factor.

Overall, this fictitious periodic perturbation wraps the band and facilitates the matching of momentum between the incident light and the propagating slot mode. By selecting specific p and adding perturbation, such "guided wave" will emerge due to the "momentum matching" effect at $k_p = 0$. Therefore, a resonance could be created and Q factor could be controlled. This observation provide a systematic way to create the desired resonance at any wavelength with any Q factor requirement.
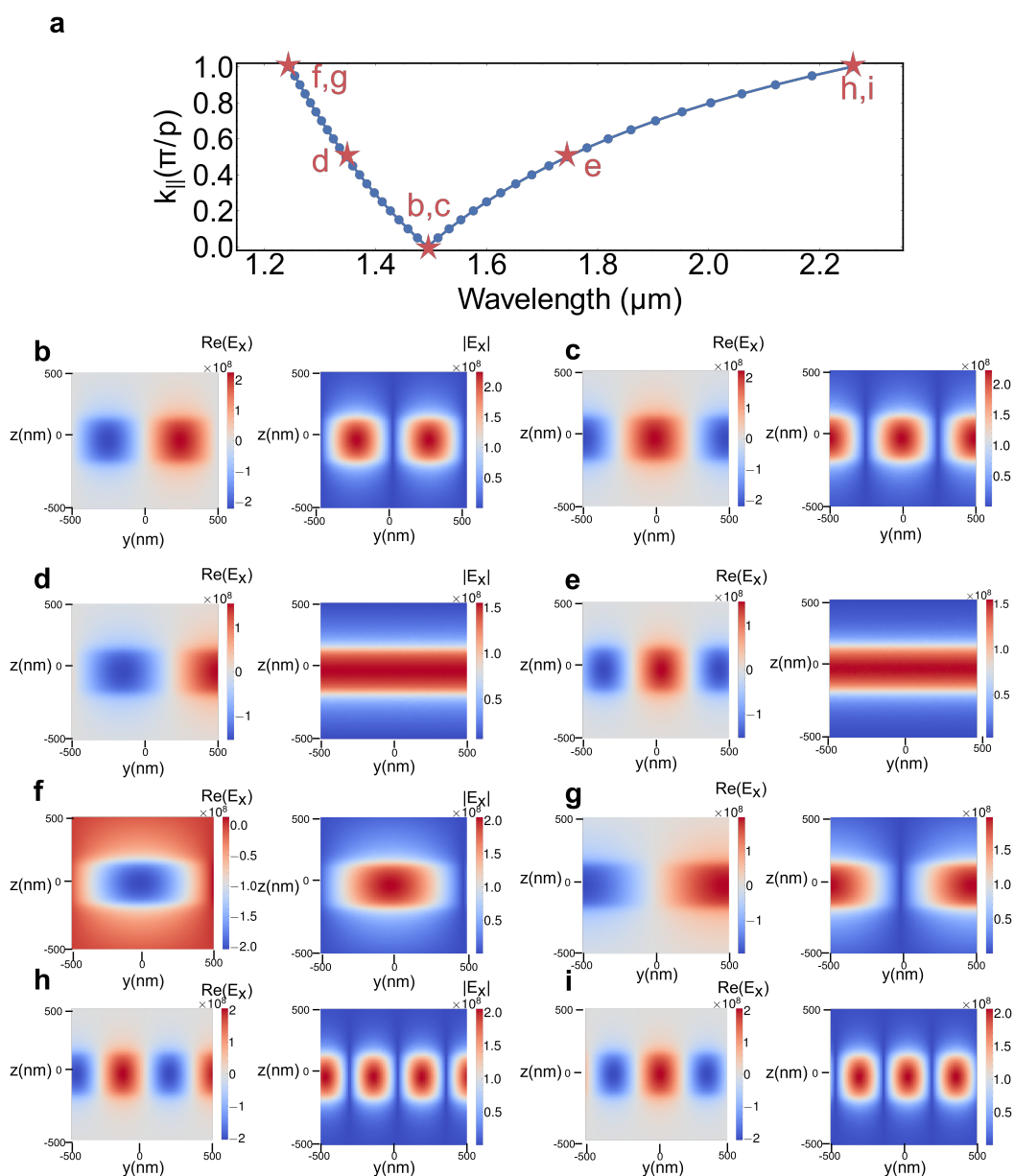
Figure 4.2: **Slot mode dispersion and corresponding electrical field profiles.**
a. The dispersion relationship of the mode when varying different k_y. The red
stars label the wavelengths and $k_\parallel$ numbers of the mode profile ($Re(E_x)$ and $|E_x|$)
in the following subfigures. p: the period of the floquet boundary condition in
numerical simulation(Same as Fig. 4.1). **b-c.** The mode profile when $k_\parallel = 0$. b
and c are two degenerate modes. **d-e.** The mode profile when $k_\parallel = \pi/(2p)$. The
longer and shorter wavelength mode are described in d and e, respectively. **f-i.** The
mode profile when $k_\parallel = \pi/p$. f,g and h,i are two degenerate modes in the longer
wavelength end and shorter wavelength end, respectively.
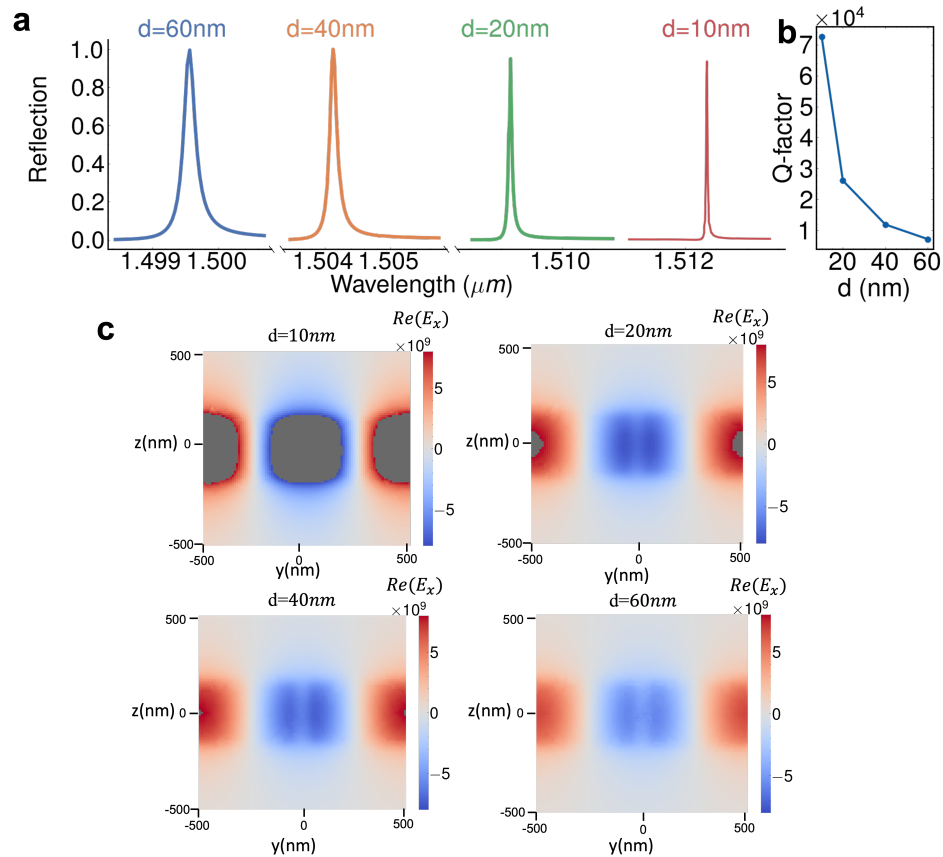
Figure 4.3: **The resonance characteristics of the slot mode under normal incidence for different notch sizes.** The profiles are plotted at the resonance wavelength. **a.** Numerically calculated reflection spectra of the slot resonances. The silicon is suspended in the air without any substrate. Four different spectra are plotted by changing d from 10 nm to 60 nm. **b.** Dependence of the Q factor on the perturbation parameter d for the spectra shown in a. **c.** The y-z cross-section electrical field profile ($\text{Re}E_x$) of the slot mode in different notch sizes. d: The width of the notch perturbation(Same as Fig. 4.1a). The grey pixels indicate that the field is over or below the limit of the colorbar.

4.3 Amplitude modulation design and experimental results

Since the electrical field of the slot mode is mostly confined in air, the mode is highly sensitive to the air gap width. As a result, the horizontal movements between nanobars induced by electrostatic force will lead to significant modulation of optical signals. Fig. 4.4a shows the conceptual schematics of the proposed NEMS-tunable devices. The system consists of two groups of suspended silicon bars in a comb-shaped arrangement. Every bar has periodical notches to create high-Q resonances, and every pair of nanobars is interdigitally connected to different islands for electrical biasing. To enhance the robustness, the two bars with the same voltages are linked together at the anchors [70]. The device could be directly fabricated using a commercial silicon-on-insulator (SOI) wafer. The voltage setting and the cross-section of the system are shown in Fig. 4.4b. One period unit with width w_p includes one pair of nanobars grounded and at a voltage separately. The voltages on the nanobars are doubly interdigitated such that when there is a voltage difference between the neighboring nanobars, the electrostatic force will cause smaller w_s. In the experiment, the length of the nanobars could be tens of μm and is much longer than the wavelength. Therefore, we assume that the nanobar is infinite in the y-direction in numerical simulation [70, 83]. The reflection spectra for different slot widths are plotted in Fig. 4.4c. As w_s gets smaller, the resonance shows a larger amount of the redshift. To illuminate the relationship between the bias voltage and the maximum displacement, we simulate the mechanical displacement under the different voltages, assuming that the length of the nanobars is 33 μm (using Comsol Multiphysics™, see supplementary material section 1). In Fig. 4.4d, we plot simulated results of the mechanical movement at the center of the nanobar and the absolute reflection at input wavelength $\lambda = 1.4573$ μm (where $R = 0.05$ when $w_s = 80$ nm) and $\lambda = 1.4544$ μm (where $R = 0.05$ when $w_s = 90$ nm) as a function of the applied voltage. It is worth noting that we assume the slot gaps shrink uniformly along y direction in reflection simulation and the displacement is the same as the center of the nanobar (see supplementary material section 1). Under the conditions above, the numerical pull-in voltage is only 1.65 V due to the small w_s of $90nm$. The maximum slot width change Δw_s of each nanobar has an approximately quadratic relationship with the bias voltage, and within $1.5V$, the maximum displacement for each bar is over 10 nm. Thanks to the high sensitivity of the slot resonance, the reflection amplitude will have 11.9 dB modulation from 0 V to 0.926 V, and 12.3 dB modulation from 1.117 V to 1.296 V. The results indicate that a high extinction ratio could be accomplished within CMOS-level voltage with
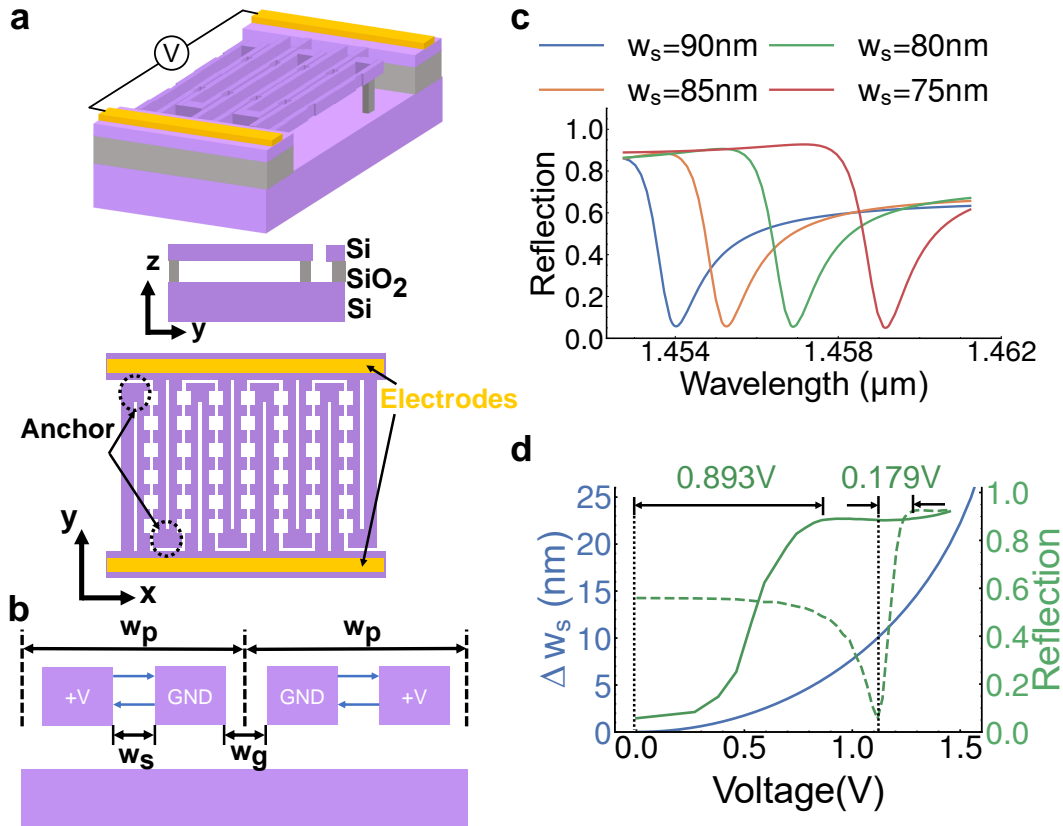
Figure 4.4: **Slot mode tuning properties. a.** Device design. From top to bottom: perspective view, a cross-section along the bar, and top view. **b.** The voltage setting of the device. Grounded bars (GND) and bars at a voltage (V) are interdigitally connected in groups of two. w_p is the smallest period of the device. **c.** Calculated reflection spectra of the device in (a) for different spacings between nano-beams (w_s). Light is incident from $+z$ to $-z$ direction. **d.** Blue: Simulated slot gap width change Δw_s at the center of the nanobar for different bias voltages. Solid Green: Modulation of the reflection amplitude at wavelength $1.4544\mu m$. Dashed green: Modulation of the reflection amplitude at wavelength $1.4573\mu m$.

the proposed device.

To experimentally demonstrate the proposed concept, the devices described in Fig. 4.4a are fabricated and characterized. The fabrication methods are similar to what we previously reported [70]. Figs. 4.5a-d show the step-by-step zoom-in image from an optical camera image to the scanning electron microscope (SEM) image. In order to realize a suspended structure in the experiment, we implement two modifications to the theoretical design (see supplementary note 1). First, to make sure the anchor is fixed, we carefully control the hydrofluoric acid etching

time when releasing the silicon nanobars. As a result, the BOX layer is not fully etched. Second, to improve the robustness of the device, we employ a series of anchors to extend the overall length of the slot. In Fig. 4.5c, the device length is $150\mu m$, and the distance between the anchors is $25\mu m$. The devices are connected to two electrode pads in parallel for multi-device fabrication and testing. All electrodes are wire-bonded to a customized PCB board connected to the voltage source. We found that the experimental reflection response (Fig. 4.5f) reproduces the simulation results shown in Fig. 4.5e. The varied background reflection indicates a low-Q guided mode, and different Fano resonance shapes could be attributed to the different coupling strength between the slot mode and guided mode [102]. Since the reflection spectra are normalized using the reflection from the gold electrode, the actual reflection should be a few percentage higher. When voltage is applied, the resonance exhibits a redshift as shown in Fig. 4.5g. A 1.2 V bias voltage induces a 0.9 nm redshift of the slot mode, confirming that the resonance is highly sensitive to the slot gap change. Besides the redshift, the modulation of the reflection is 10% at $\lambda = 1.569 \ \mu m$. In addition to redshift, there is also an amplitude decrease, which we attribute to diminished coupling between the slot modes and the incident beam [103, 104]. When the electrical bias is applied, the bending of the two-sided fixed suspended bars occurs, causing local slot widths variation along the y direction. The local variation in slot widths will decrease the local coupling rate between the incident light and the slot mode.

Multiwavelength design with individual Slot Tuning

Based on the previous discussion on the principle of the slot mode, we know that the slot mode is mostly propogating along the slot. That indicates that each slot could be independently operated. To prove this concept, we propose a multiwavelength device design, where the device has resonance in two different wavelengths and each resonance could be individually addressed. Fig. 4.6a shows the proposed device designed for operations at two different wavelengths. The x-direction period includes 8 bars in total: 4 pairs of V and GND nanobars with total width w_p. Each pair hosts a slot resonance, with the slot gaps w_{s1} or w_{s2}. When $V_1 = V_2 = 0$, $w_{s1} = w_{s2}$. To create slot resonances at two different wavelengths, every two pairs have different slab widths w_{b1} or w_{b2}. For this example, $w_{b2} - w_{b1} = 10 \ nm$. This device is out of the subwavelength regime since $w_{b1} \neq w_{b2}$. However, since the difference between w_{b1} and w_{b2} is only 10nm the structure is only weakly diffracting (see section 4.6). In this voltage setting, the slot widths w_{s1} and w_{s2}
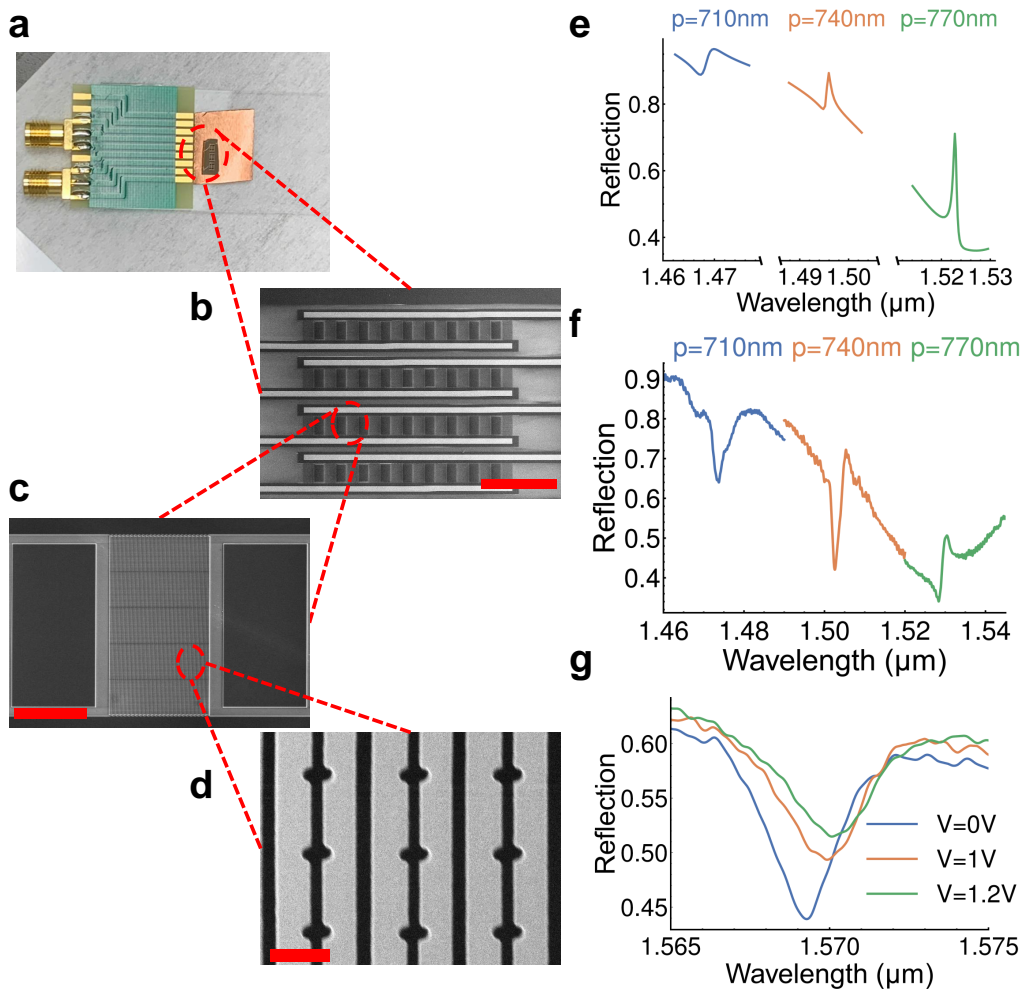
Figure 4.5: **Experimental NEMS tuning. a.** An optical image of the chip that is wire bonded to a customized print circuit board. **b-d.** Scanning electron microscopy images of the device. The scale bars are $500\mu m$, $50\mu m$ and $500nm$ respectively. **e-f.** The simulated (top) and experimental (bottom) reflection spectra of the proposed device for different notch periods p. **g.** The reflection spectra of the slot metasurface devices under different electrical bias voltages.

could be dominantly controlled by V_1 and V_2, respectively. In other words, the control voltage V_1 (V_2) mainly shrinks the gap w_{s1} (w_{s2}) but does not affect the gap w_{s2} (w_{s1}) since the electrostatic force will mostly affect the adjacent nanobar at a different voltage. Therefore, the tuning voltage $V_1(V_2)$ can control the corresponding slot gap $w_{s1}(w_{s2})$ while keeping the other slot gap w_{s2} (w_{s1}) unchanged, and the period width remains constant. Fig. 4.6b shows the reflection spectra when we change the w_{s1} and w_{s2} separately while keeping the other constant. We also plot the electric field profile in the corresponding resonance. The electric field profile only includes half of the period because of symmetry. In Fig. 4.6b, the resonances in shorter (longer) wavelengths are related to the slot on the left (right), and the other slot remains non-resonant because of the frequency detuning. Since only half of the slots are excited in the resonance, the reflection modulation amplitude is limited to 50 %. Thus, the maximum amplitude modulation is 13.3 dB in 1.491 μm and 20.5 dB in 1.509 μm. The green (orange) curve indicates that when we only move $w_{s1}(w_{s2})$, the resonance in low (high) wavelength will show the redshift, but the other resonance remains almost undisturbed. As a result, this design strategy will allow us to modulate the reflectivity in multiple wavelengths independently. The device for multiwavelength operation will have first-order diffraction. The 0th order and the 1st order spectra are shown in Fig. 4.6 (the -1st order has the same power as the 1st order due to symmetry). When the input wave is not on resonance, the direct reflection is slightly over 10% and the first-order reflection is nearly 0, as the geometry difference between the two slots is small. On resonance, the 0th and 1st order reflective power increases to 40% and 10% respectively. The total reflective power has increased to 60% due to the increased reflection from the 0th order and 1st (-1st) diffraction channel. This confirms that when the input wave is on resonance, the reflective power in the 0th order is not coming from other reflective diffraction channels, but from the transmission channels.

4.4 Phase modulation design and numerical results

Although large amplitude modulation could be achieved through the aforementioned designs, the phase response is still limited due to the limited coupling coefficient from the input plane wave to resonant mode [28, 64]. To enhance the phase response, one of the potential solutions is to add a mirror at the bottom of the nanobars [27, 28]. The mirror reflects the light and enhances the coupling between the resonant slot mode and the illuminated light from the top. Here, we propose a NEMS design with a metal mirror, where the phase response could be close to 2π.
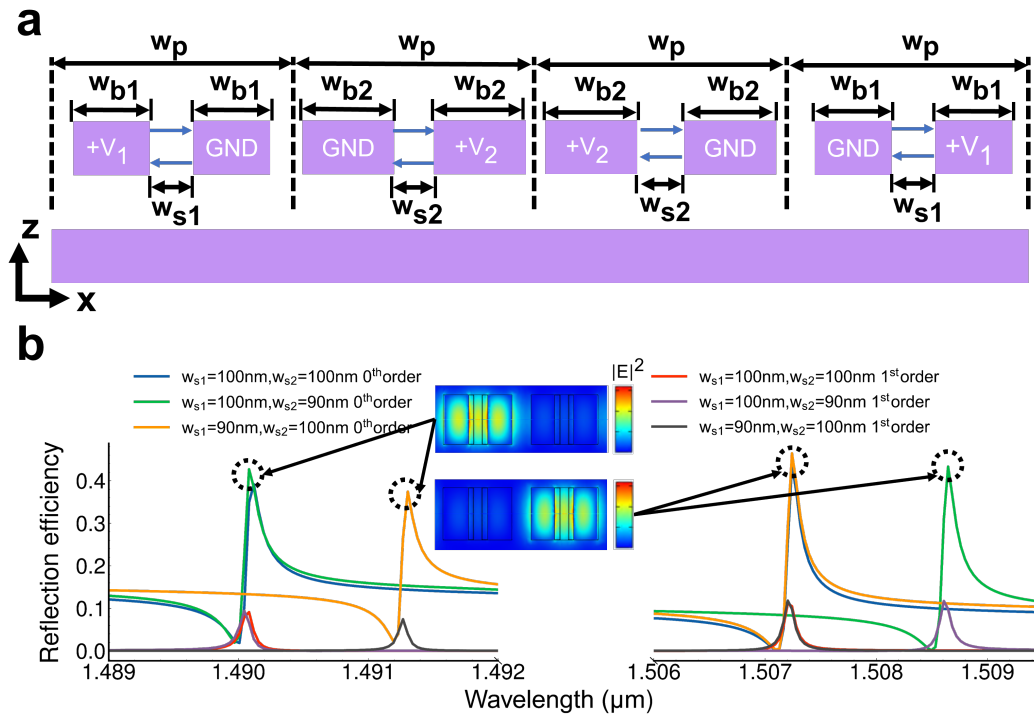
Figure 4.6: **Multiwavelength NEMS tuning. a.** Cross-section of one period for the multiwavelength device. The slot widths where we insert notch perturbations (not shown in the figure) are w_{s1} and w_{s2}, which target the tuning of two wavelengths. Two nanobars that form the slot have the same width w_{b1} and w_{b2} respectively. w_g is the air gap between the grounded bars. The bars that belong to different bias voltages are separated by two ground bars to make sure that two bias voltages will independently control the slot sizes. **b.** Spectral shifts due to size changes in different slots. The shrinkage of the slot gap $w_{s1}(w_{s2})$ leads to the redshift of the mode resonance in $1.490\mu m(1.507\mu m)$ while keeping the other mode resonance unperturbed. Insets represent the cross-section of the electric field profile in two slot resonances. The resonance at the lower wavelength represents the resonance in the left slot, and the resonance at the higher wavelength represents the resonance in the right slot.

The cross-section of the design is presented in Fig. 4.7a. The gold mirror is added between the oxide layer and the silicon substrate. To introduce a fabrication-compatible structure and simplify the discussion, we assume that the silicon oxide layer is fully etched when releasing the silicon bars. Except for the anchor regions on both sides of the bars, there are only air gaps between the silicon nanobars and the gold mirror. This structure could be fabricated by wafer bonding and thinning [105, 106], and the gold mirror could also be replaced by a Bragg mirror [64]. The existence of the gold mirror will enhance the mode coupling with the upper port as the mirror reflects the light upward. Thus, the reflected phase response at the resonance will get enhanced to nearly 2π. Fig. 4.7b shows the reflection amplitude and phase around the slot resonance for different slot gaps w_s. Due to the high reflectivity of the gold mirror, when the device is off-resonant the overall reflectivity is close to 1. The coupling between the incident wave and slot mode resonance will induce a Fano reflectivity lineshape [61]. The phase response covers 1.8π from $w_s = 70nm$ to $w_s = 90nm$. The high reflectivity and large phase coverage indicate that the resonance is highly over-coupled. To illustrate the effect of air gap over coupling strength, the complex reflection coefficient for slot resonances at different air gaps h_a are plotted in Fig. 4.7c. Each resonance generates a circle in the complex plane. As h_a increases, the area of the circle also increases, indicating the increase of the coupling strength [64]. At $h_a = 275nm$, the zero reflectivity shows that the critical coupling regime is achieved. Further increase of h_a will help the mode resonance enter the over-coupling regime, where the circle includes the origin point. At $h_a = 350nm$ the phase coverage is close to 2π, and the overall reflection is over 80%. This indicates that it is possible to achieve phase-only tuning from slot mode resonance. As an example, Fig. 4.7b shows that when we change the slot width, we could achieve 2π phase-only modulation with nearly unity reflection.

After the investigation of the phase modulation, we could jointly combine the property of the locally resonant slot mode and enhanced 2π phase modulation to achieve one-dimensional spatial phase modulation at the wavelength-scale pixel level. To unveil the potential of wavefront engineering on this platform, we design an active beam deflector which can attain diffraction efficiency $\sim$75 % in the first order. The design for one period is illustrated in Fig. 4.8a. It should be noted that although the slot resonance is mostly confined within the slot, the crosstalk between the adjacent slots can only be ignored in the amplitude-related design, but remains crucial in phase-related design (see supplementary material section 3-4). To enable the spatial tuning of the slot metasurfaces, the cross-coupling between the

a

b

c
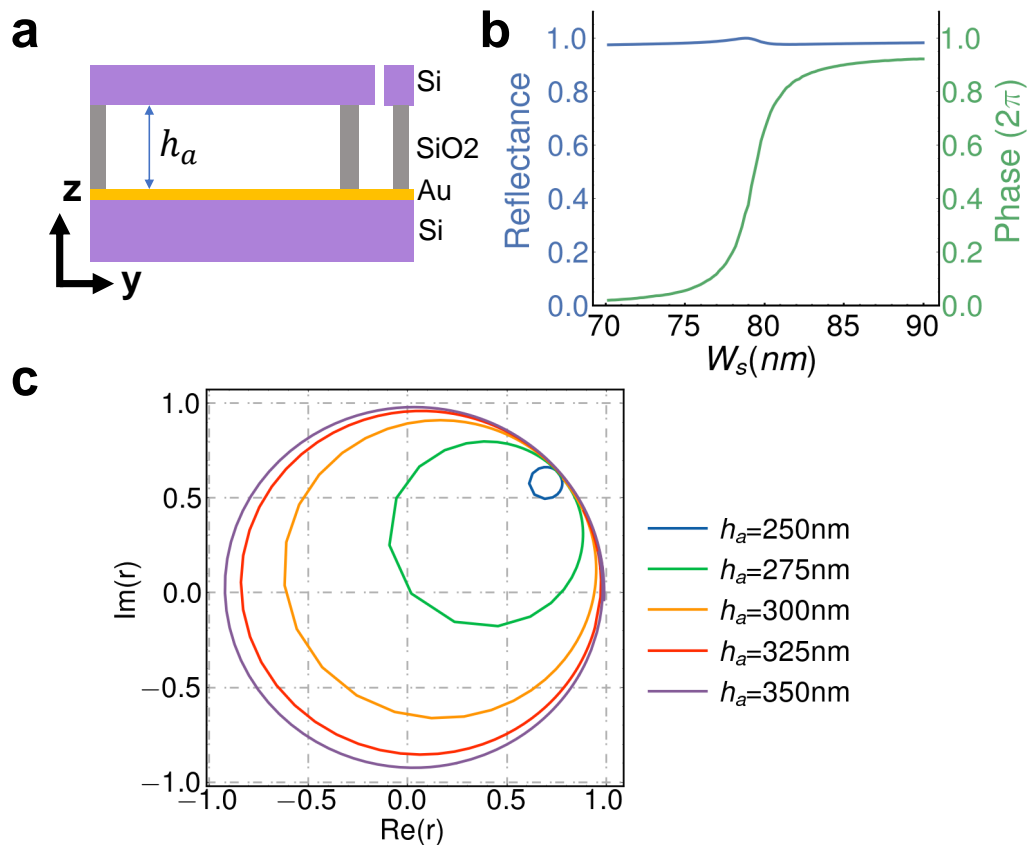
Figure 4.7: **Design of phase modulator. a.** The cross-section of the proposed structure that incorporates nearly 2π phase modulation. **b.** The reflection amplitude and phase around the slot resonance as a function of different slot sizes. By reducing the slot gap size from $90nm$ to $70nm$, the reflectance remains over 97% while phase coverage is over 1.8π. **c.** The reflection coefficient in the complex plane around the slot resonance in air gap thicknesses h_a from $250nm$ to $350nm$. When $h_a > 275nm$, a phase coverage close to 2π is achieved.

adjacent slots should be blocked. We use a small silicon nanobar to block the cross-coupling [107, 108], and the gaps between the nanofins w_{aw} and the nanofin width w_{bw} are chosen to be only 100nm to reduce the pixel size but keep the fabrication compatibility. The existence of the additional adjacent nanofins will extend the period length to 1200nm, but the size of the pixel still is in the sub-wavelength regime in the air. These additional nanofins will cause a small redshift of the resonance frequency, but the phase coverage is preserved, as shown in Fig. 4.8b. From this one-to-one mapping relationship between slot size w_s and phase response, we pick three points (0.55π, 1.27π, 1.97π) that are roughly spaced by $\frac{2\pi}{3}$ to form a three-pixel supercell structure, labeled as blue stars. The three different points are
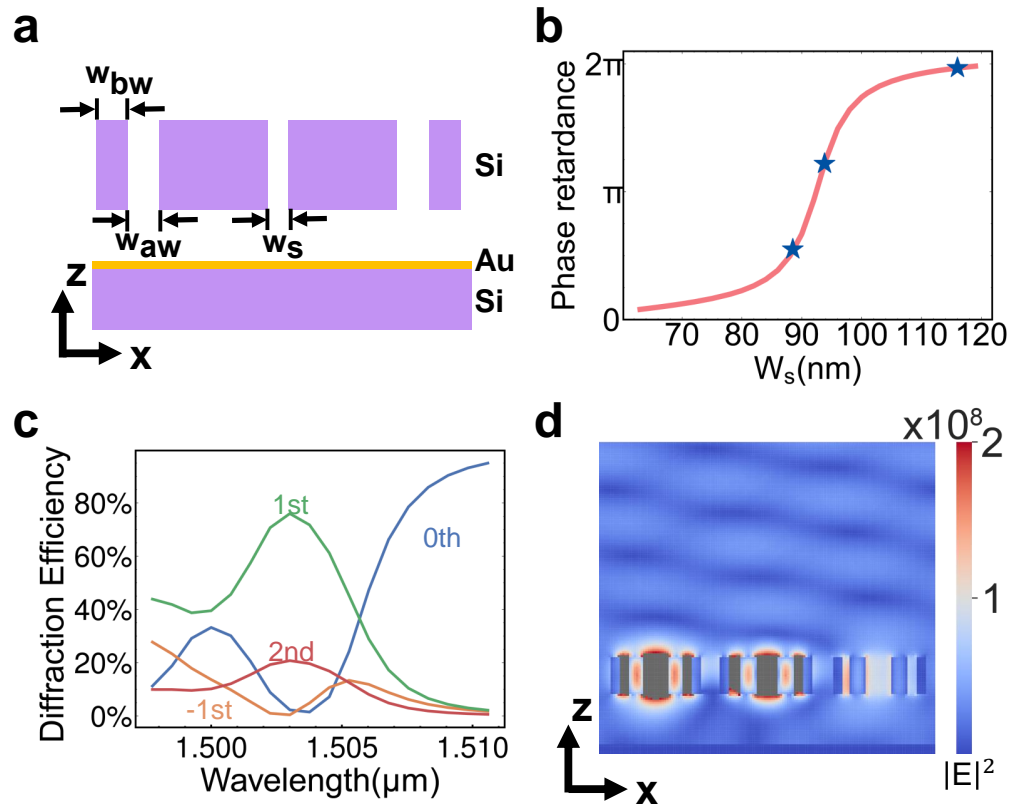
Figure 4.8: **Demonstration of a beam deflector. a.** The geometry of one periodic unit of the beam deflector. The nanobar blockers with width w_{bw} are added to prevent the cross-coupling between the pixels. The nanobar blockers don't have notch perturbation. **b.** The phase response of the slot mode with respect to the slot size w_s. The blue stars represent points where $w_s = 88.5nm, 93.8nm, 116nm$ respectively. We choose these 3 slot gaps to form a 3-period supercell beam deflector. **c.** The diffraction efficiency of the device designed according to (b). The major diffraction orders (-1st, 0th, 1st, 2nd) are shown. **d.** The electric field profile of the device described in (b) at $1.503\mu m$. The grey pixels indicate that the field is saturated.

intentionally chosen to be larger to avoid the pull-in effect, and they are optimized around the exact $\frac{2\pi}{3}$ spacing points due to the residual crosstalk between different slots. As shown in Fig. 4.8c, the diffraction efficiency achieves maximum ~ 75% in 1.504μm for the 1st order. Fig. 4.8d illustrates the electrical field profile of the slot structure at 1.504μm, where the first order steering angle is 24.7°. Since the slot gap size change is only ~ 30 nm, the required voltage to drive the beam steering should be at CMOS level.

We note that the beam deflector design shown in Fig. 4.8 could be easily extended to supercells including more slots for the purpose of smaller deflection angle and ultimately quasi-continuous beam steering [27, 28]. However, our computing tools do not allow for simulating these larger structures because of lack of memory. Although using the phase gradient is the easiest way to generate a steered beam, advanced optimization techniques are expected to result in suppressed side lobes and enhanced directivity [109].

4.5 Conclusion

In conclusion, in this chapter we propose a platform that could achieve efficient amplitude and phase tuning under the CMOS-level modulation voltage and have wavelength-scale pixel level. It could achieve 16.9 *dB* modulation within 0.752 V in numerical simulation. We also observe 10% reflection modulation under 1.2*V* bias voltage in the experiment. The locally resonant property enables individual reflective phase tuning in individual slots. With a more judicious design, it achieves 75% diffraction efficiency. The key component of the platform is that the slot mode resonance is highly sensitive to electrostatic perturbation thanks to the confined electric fields in the slots.

For the future directions, the required driving voltage may be further reduced by inverse-designed gratings, as we believe more sophisticated nanostructures could lead to a stronger optical response to mechanical displacement. By utilizing avoided crossing of resonances, the phase modulation capacity could be potentially improved up to 4π [67]. Furthermore, a more complicated phase profile could be generated if the number of pixels is extended. We expect that the combination of the slot modes and the NEMS platform will enable 1D high-resolution phase-only spatial light modulators with CMOS-level operations, lower power consumption and scalable manufacturing.
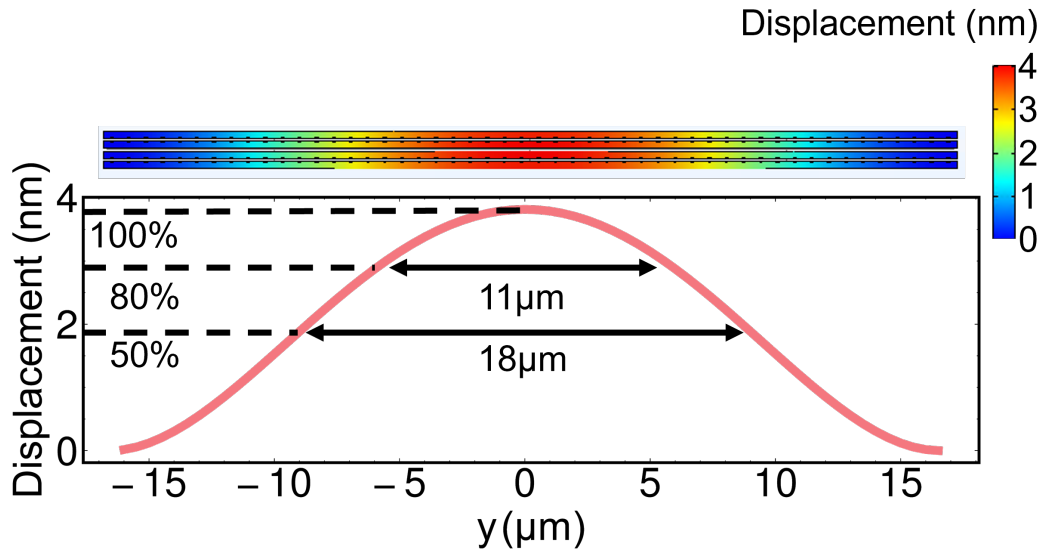
Figure 4.A.1: **Mechanical displacement profile of the nanobars when** $V = 1V$**.** The displacement is the absolute displacement for one nanobar. Top: the colormap of the mechanical displacement in the top view. Bottom: the 1D displacement profile along the nanobar.

4.6 Appendix

Simulation and experiment details and detailed device parameters

The optical simulation is performed using COMSOL Multiphysics™ with periodic conditions applied along the x and y directions (see Fig. 4.1 in the main text). Detailed simulation device parameters are provided in Table 4.A.1. For the mechanical simulation shown in Fig. 4.4d, we also employ COMSOL Multiphysics™. The nanobar length is set to $33\mu m$, with both ends fixed. The nanobars serve as terminals with a fixed voltage V or ground. We calculate the displacement as the maximum displacement along the x-direction at the center of the nanobar. The displacement profile, shown in Fig. 4.A.1, exhibits a bell curve with maximum displacement at the center. Specifically, for a nanobar length of $33\mu m$, the regions where displacements exceed 80% and 50% of the maximum displacement are $11\mu m$ and $18\mu m$, respectively. In Figs. 4.5c-d, we assume a uniform shrinkage of w_s for simplicity. Considering the relatively flat displacement curve at the center of the nanobar ($y = 0$), we also assume that the displacement is the same at the center along the y-direction. Furthermore, the decrease in resonance amplitude observed in Fig. 4.5g can be explained by the non-uniform property of the mechanical displacement.

In Fig. 4.4a, the silicon oxide layer beneath the suspended nanobars is fully etched.
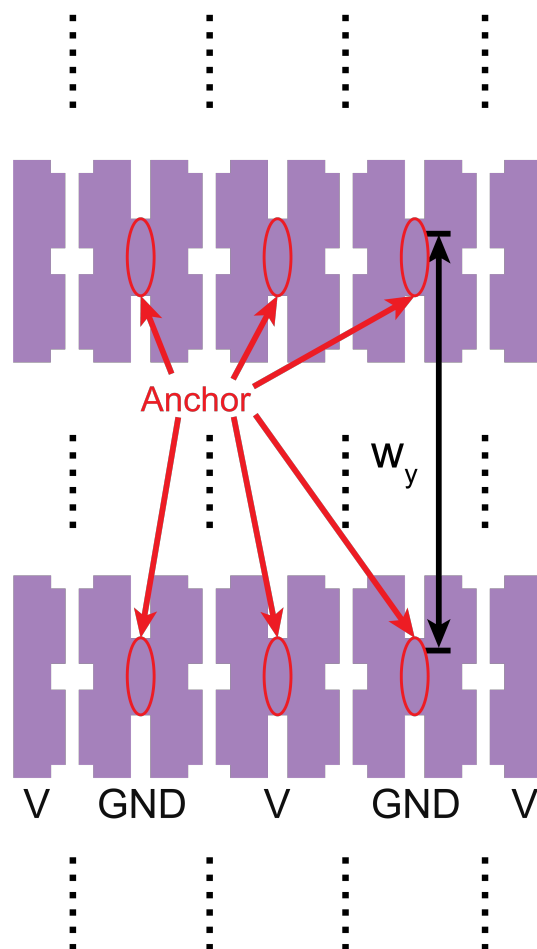
Figure 4.A.2: **Top view of Experimental device with a series of anchors.** The newly created anchor connects the adjacent bar with the same bias voltage. w_y is the y-axis distance between the anchors.

In the experiment, we create an air gap and release the nanobars using hydrofluoric (HF) acid etching. To fix the anchor while releasing the nanobar, we carefully control the etching time. In our experiment, the silicon-on-insulator (SOI) wafer has a $3\mu m$ buried oxide (BOX) layer thickness, resulting in a remaining oxide layer after nanobar release. The thickness of the remaining oxide layer, h_o, is indicated in Table 4.A.1. We note that the surface of the remaining BOX layer is non-uniform due to the isotropic nature of HF etching. The estimated remaining layer thickness is based on the estimated rate of HF acid etching. For the designs in Fig. 4.4, Fig. 4.7 and Fig. 4.8, we do not consider these experimental details and assume $h_o = 0$.

In the simulation, we assume an infinitely long slot length and apply periodic

boundary conditions along the y-axis. However, in the experiment, the length of the nanobars plays a crucial role in validating this approximation and determining the speed (see supplementary note 5). Since the distance between the nanobars is only approximately 90 nm, increasing the length of the slot makes it susceptible to perturbations during fabrication. To further extend the slot length, we incorporate additional anchors between the air gaps adjacent to each slot. These anchors connect the adjacent nanobars, and their length is chosen to be sufficient for connecting the anchor to the unetched silicon oxide layer. To strike a balance between the minimum bias voltage required for tuning and the fabrication yield rate, we choose an anchor distance of $w_y = 25\mu m$. The top view of the experimental fabricated device is illustrated in Fig. 4.A.2, showcasing the extended slot length achieved through this approach.

The measurement setup is depicted in Fig. 4.A.3. Detailed information about the setup and experimental procedures can be found in our previous report[70]. To obtain the reflection spectra of the x-polarized input light, the grating is aligned at 90 degrees with respect to the beam splitter axis. The polarizer (Pol.) and the half wave plate (HWP) in front of the objective lens are aligned at 45 and 22.5 degrees, respectively.

Device	p	h	w_p	w_s	w_{b1}	w_{b2}	d	l	h_a	h_o	w_{aw}	w_{bw}
Fig. 4.2a, Fig. 4.3a-c	varied	500	700	90	220	220	varied	varied	N/A	N/A	N/A	N/A
Fig. 4.4c-d	740	490	700	varied	240	240	60	110	150	0	N/A	N/A
Fig. 4.5e-f	varied	490	1400	90	555	555	90	120	250	2700	N/A	N/A
Fig. 4.4g	870	490	740	90	245	245	70	120	300	2700	N/A	N/A
Fig. 4.6	590	570	1000	90	345	335	60	80	150	0	N/A	N/A
Fig. 4.7b	720	500	800	90	250	250	60	90	500	0	N/A	N/A
Fig. 4.7c	720	500	800	90	250	250	60	90	varied	0	N/A	N/A
Fig. 4.8c	720	500	1200	90	250	250	60	90	650	0	100	100

Table 4.A.1: **Device parameters used for the plot in main figures** (unit:nm) N/A: not applicable. Varied: the value of the parameter is a variable in main figure.

The crosstalk between adjacent bars

The added block in Fig. 4.8a has the scope to prevent the crosstalk between slots. To prove that it is necessary to add the blocks, we also perform full-wave simulations on the slot metasurfaces without any blocks. Fig. 4.A.4a shows the dictionary of the phase response for the periodic slot structure. We choose $(0.494\pi, 1.200\pi, 1.876\pi)$
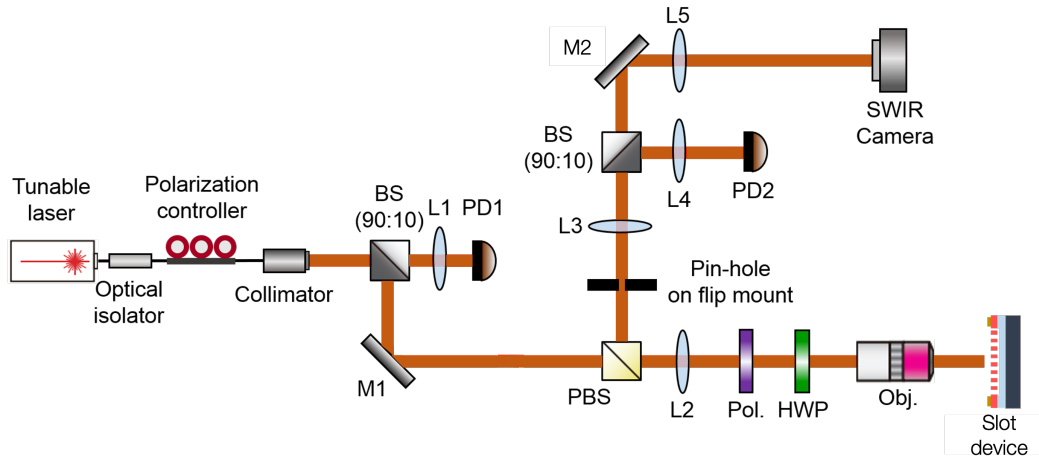
Figure 4.A.3: **Schematic illustration of the experimental setup.** The brown line indicates the paths of the light propagation. Pol.: linear polarizer. BS: beamsplitter. PBS: polarizing beamsplitter. L: lens. PD: photodetector. M: mirror. QWP: quarter waveplate. HWP: half waveplate. Obj.: microscope objective lens. SWIR camera: short-wave infrared camera.
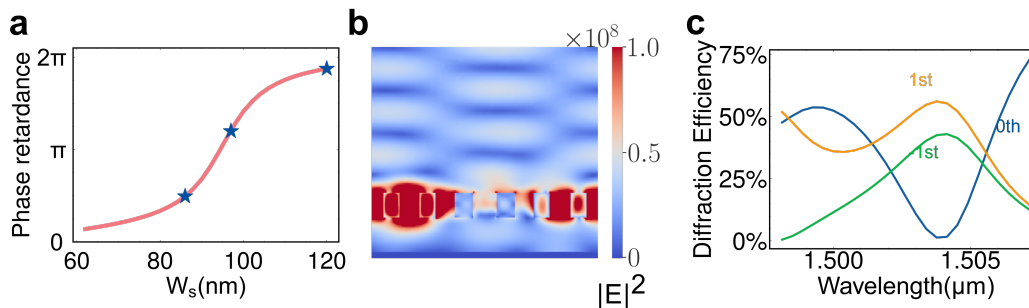
Figure 4.A.4: **Diffraction test without block. a.** The phase response of the slot mode with respect to the slot size w_s without the blocker. **b.** The electric field profile of the device described in a. at $1.504\mu m$. **c.** The diffraction efficiency of the device designed according to a. Major diffraction orders (0th, 1st, -1st) are shown.

to form a beam steering supercell. The resulting electric field profile under the normal incident light is in Fig. 4.A.4b. Instead of showing clear beam deflection, the profile incorporates different diffraction orders. Thus, the directivity of the beam deflection is lower, and there isn't a clear beam steering direction in the electrical field profile.

AC analysis and mechanical eigenfrequency

The mechanical eigenfrequency of the system is numerically investigated using COMSOL Multiphysics™. The simulation setting is the same as the one discussed in section 4.6. By varying the distance between the anchors (fixed boundary), the eigenfrequency of the device Fig. 4.5 is shown in the table 4.A.2.

W_y	Eigenfrequency (MHz)
$25\mu m$	3.5
$50\mu m$	0.89
$75\mu m$	0.40
$100\mu m$	0.22
$125\mu m$	0.14

Table 4.A.2: **Mechanical eigenfrequency of the nanobars shown in Fig. 4.5g assuming different distances of anchors W_y.**

The AC characteristic of this NEMS platform was previously investigated in ref[70]. Since this device has a longer device length ($150\mu m$), it is estimated that our experiment device has lower bandwidth (< 25kHz). This frequency is much lower than the mechanical resonance frequency of the system, so we will only consider the AC response without any resonant effect. We provide a simplified circuit model to explore the AC performance tradeoff of the system, shown in Fig. 4.A.5. We assume that the circuit includes a source resistance $R = 50\Omega$, and we model the parallel nanobars as parallel resistances $Rs = \rho\frac{l_{si}}{hw_b}/N = 0.13G\Omega$, where silicon resistivity $\rho = 10\Omega \cdot m$, nanobar height $h = 500nm$, nanobar width $w_b = 220nm$, slot gap width $w_g = 90nm$, number of nanobars $N = 100$. The slot gap capacitance $Cs = C_{per}l_{si}(N-1) = \epsilon_0\frac{K(\sqrt{1-k^2})}{K(k)}l_{si}(N-1) = 0.19pF$ is modeled using the calculation from [110], where $K(k)$ is the elliptical integrals of the first kind, and $k = \cos\left(\frac{\pi w_b}{2w_g}\right)$. The response of the voltage on the capacitor could be expressed as

$$V_{Cs} = V_0|\frac{1/(j\omega C_s)}{R_s + 1/(j\omega Cs) + R}| \tag{4.1}$$

We can calculate the 3dB attenuation frequency for voltage is $f_{3dB} = 10.4$kHz.
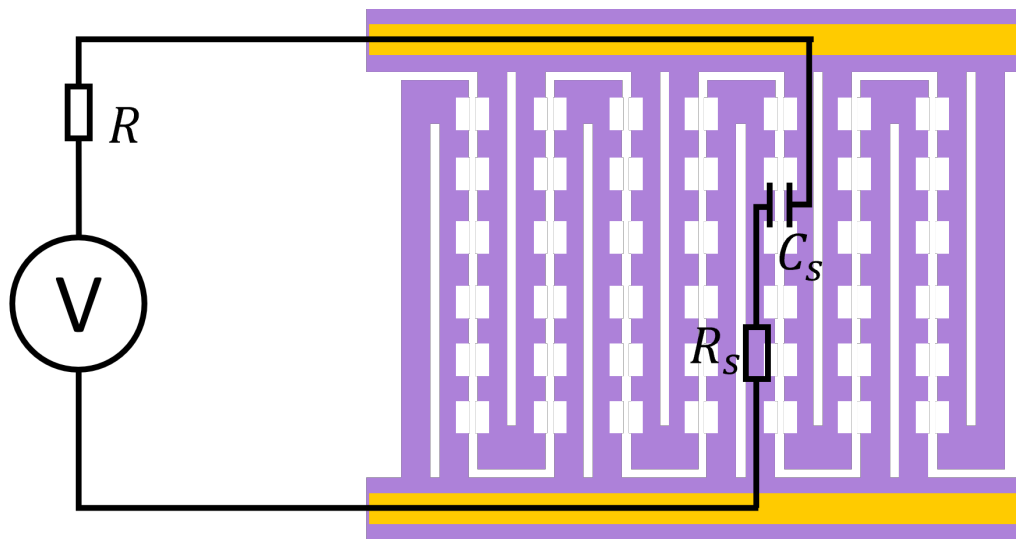
Figure 4.A.5: **Simplified Circuit for AC analysis.** V: External bias voltage. R_s: the resistance of the doped silicon bar. C_s: the capacitance of the slot.

Chapter 5

DYNAMIC LIGHT MANIPULATION VIA SILICON-ORGANIC SLOT METASURFACES

The material in this chapter was in part presented in [111].

Active metasurfaces provide the opportunity for fast spatio-temporal control of light. Among various tuning methods, organic electro-optic materials provide some unique advantages due to their fast speed and large nonlinearity, along with the possibility of using fabrication techniques based on infiltration. In this chapter, we report a silicon-organic platform where organic electro-optic material is infiltrated into the narrow gaps of slot-mode metasurfaces with high quality factors. The mode confinement into the slot enables the placement of metallic electrodes in close proximity, thus enabling tunability at lower voltages. We demonstrate the maximum tuning sensitivity of 0.16nm/V, the maximum extinction ratio of 38% within ±17V voltage at telecommunication wavelength. The device has 3dB bandwidth of 3MHz. These results provide a path towards tunable silicon-organic hybrid metasurfaces at CMOS-level voltages.

5.1 Motivation

In Chapter 3 and 4, we focus on the development of NEMS metasurfaces. With a dual-mode resonant design, the phase response has increased to 144°. Using slot mode and adding a back mirror, the high-overcoupled condition is satisfied and wavelength-scale phase modulation could be achieved. If we take another look at the design of the slot mode, we could find that it has two important properties:

- The field is confined in the low refractive index media

- The distance between the high refractive index media is small

In other words, as long as there are two media with refractive index contrast, and the low refractive index media forms a "slot", the slot mode could be formed. In addition, the mode has superior sensitivity when we have refractive index perturbation in low refractive index media. In NEMS platform, when electrostatic force moves the nanobars, the "effective" refractive perturbation happens at the intersection between

the high refractive index media and low refractive index media. Therefore the slot mode provides high optical response at low bias voltage. However, if we generalize the use of the slot mode to this refractive index perturbation perspective, the use of the slot mode isn't limited to NEMS platform anymore.

In modern photonics, a multitude of technologies for tunable optics and frequency conversion[112, 113] are realized with nonlinear materials that have low loss and a strong $\chi^{(2)}$ effect, such as lithium niobate[114, 115], aluminum nitride[116], and organic electro-optic (OEO) materials[117]. Their ultrafast responses make it possible to use RF or millimeter-wave control[118]. Developments in computational chemistry have also led to artificially engineered organic molecules that have record-high nonlinear coefficients with long-term and high-temperature stability [119, 120]. However, their potential in modifying free-space light has been relatively unexplored until recently. Several OEO material-hybrid designs have demonstrated improved tunability of metasurfaces [121–123]. Utilizing dielectric resonant structures and RF-compatible coplanar waveguides, a free-space silicon-organic modulator has recently accomplished GHz modulation speed [110]. However, all demonstrations to date require high operating voltages ±60V, due to low resonance tuning capability(frequency shift / voltage) which hinders their integration with electronic chips.

In this work, we propose combining high-Q metasurfaces based on slot-mode resonances with the unique nano-fabrication techniques enabled by OEO materials which drastically reduces the operating voltage. The low voltage is mainly achieved from the ability to place the electrodes in close proximity to each other while hosting high-Q modes in between and the large overlap of the optical and RF fields in OEO materials. In the following sections, we first provide the design concepts and considerations for achieving a reduced operating voltage. Next, we numerically demonstrate the advantage of a particular selected mode compared to other supported modes in the structure. Finally, we experimentally realize our concepts and characterize the performance of the electro-optic metasurface.

5.2 Device design

The reported device and its operation scheme are depicted in Fig. 5.1. Light polarized along x (E_x) is incident onto the device along $-z$ direction, and then couples into the slot mode hosted in between the silicon nano-bars. Gold electrodes are placed on top of the nano-bars and doped silicon is used to maximize the voltage drop across the slot filled with OEO material. The active OEO material regions have
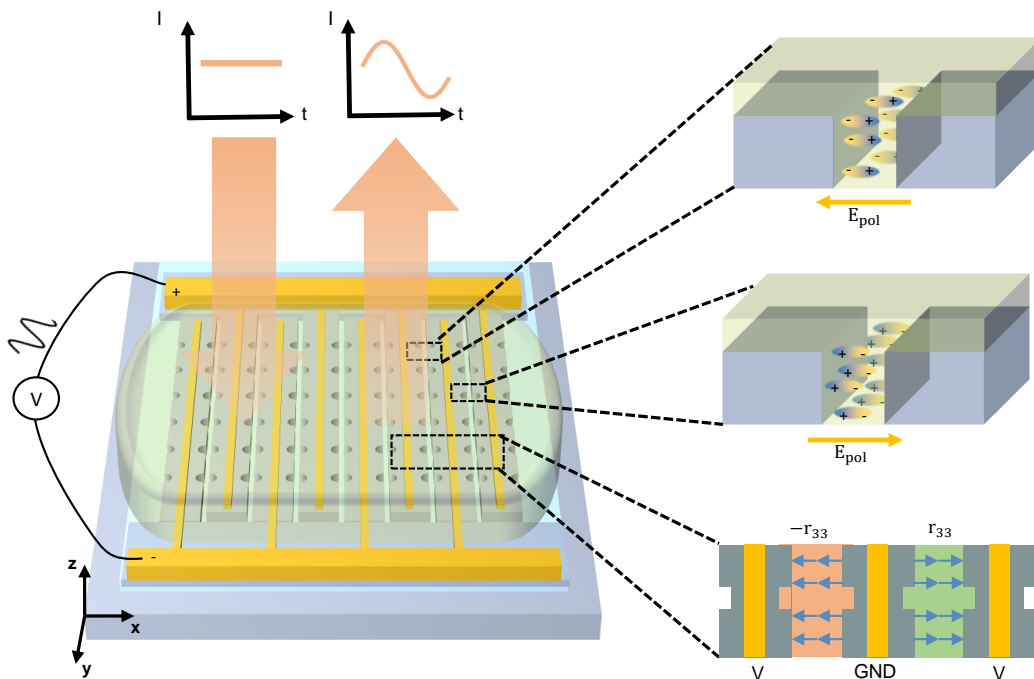
Figure 5.1: **Conceptual schematic of silicon-organic electro-optic tunable meta-surfaces.** A beam of light is incident on the metasurface, which consists of silicon nano-bars. The light is coupled into the slot mode inside the metasurface, which is sensitive to any refractive index perturbation in the slot. The OEO material is coated on top of the metasurface and fills the slot waveguide between the silicon nano-bars. The organic molecule inside the slot is aligned with the DC/RF field generated by the electrodes. When the RF bias voltage is applied on the electrodes, the electro-optic (Pockels) effect will generate refractive index modulation. As a result, the intensity of the reflected beam will be modulated accordingly.

nonlinear coefficients r_{33} with each two adjacent slots exhibiting opposite signs of nonlinear coefficients due to the poling field direction. When the operating signal is applied, the active layer induces a refractive index change

$$\Delta n(t) = -\frac{1}{2}n_{\text{mat}}^3 r_{33} E_{\text{ext}}(t) \tag{5.1}$$

where E_{ext} is the external electric field in the OEO material. Notice that due to the geometry of the electrodes, the signal electric fields $E_{\text{ext}}(t)$ also have opposite signs in adjacent gaps, as shown in Fig. 5.1. Therefore, the overall response from any two adjacent slots is the same. Besides the operating voltage or the field in slots, the perturbation strength to the optical mode also depends on the overlap factor Γ_c between the electric field profile and the optical mode profile. Γ_c is irrelevant to the external voltages. To calculate this overlap factor, we need to treat E_{ext}, r_{33} as

spatial dependent variables. Based on cavity perturbation theory [47] (see the full derivation in section 5.8), we could extract the formula to calculate the shift of the resonant frequency:

$$\Delta\omega = -\frac{\Delta n_{\text{avg}}}{n_{\text{mat}}}\omega\Gamma_c \tag{5.2}$$

where $\Delta n_{avg} = -\frac{1}{2}n_{\text{mat}}^3 r_{33}\frac{V_{\text{ext}}}{w_g}$ denotes the refractive index change upon applying a constant field of $\frac{V_{\text{ext}}}{w_g}$ across the gap.

By examining Equation 5.2, we can gain valuable insights into two distinct methods for reducing the voltage of the device: reducing the distance between electrodes and increasing the overlap factor. However, introducing closer metallic electrodes leads to inevitable losses, thus reducing the quality factors and limiting the sensitivity to refractive index changes. Therefore, transmitting electric fields through conductive dielectrics is preferred. In our reported device, doped silicon acts as the electrodes with gap width (w_g) down to 100nm. At the same time, this gap between the silicon nano-bars will host slot modes[97], whose demonstrated high overlap with the OEO material has been utilized in many integrated silicon-organic modulators[124–126]. However, the slot waveguide is intrinsically decoupled from the free-space light due to momentum unmatching. To enable coupling with normally incident light, we create periodic notches along every slot [94, 127]. The notch periodicity and the notch size dominantly determine the resonance wavelength and the coupling strength of the slot resonance, respectively. As a result, both the quality factor and the resonant wavelength could be judiciously engineered (see supplementary sections 1-2). Although a similar structure has been proposed for sensing[128], the design strategy and target applications here are completely different. To show the advantage of the slot modes while shrinking the distance between electrodes down to 100nm, it is worth discussing the possible optical modes in such a structure. The detailed schematic view, top view, and cross-section view of the example device are shown in Fig. 5.2a, where three different colors (gray, blue, green) indicate different materials (silicon, silica, OEO material or HLD). In the numerical simulations shown in Fig. 5.2b-h, HLD has a refractive index of 1.85[120]. Fig. 5.2b shows the poling field profile upon applying a DC bias across the electrodes. The x-z cross-section is cut at the center of a notch pair shown as dashed rectangle in the schematic view of Fig. 5.2a. Neglecting any interface effect[129], we can treat the relative amplitude of r_{33} at each spatial point as following this pictured poling field profile. The geometry of the electrodes results in a high E_x field along the slot and a rapid field decay above and below the slot. Therefore, to simplify the simulation,
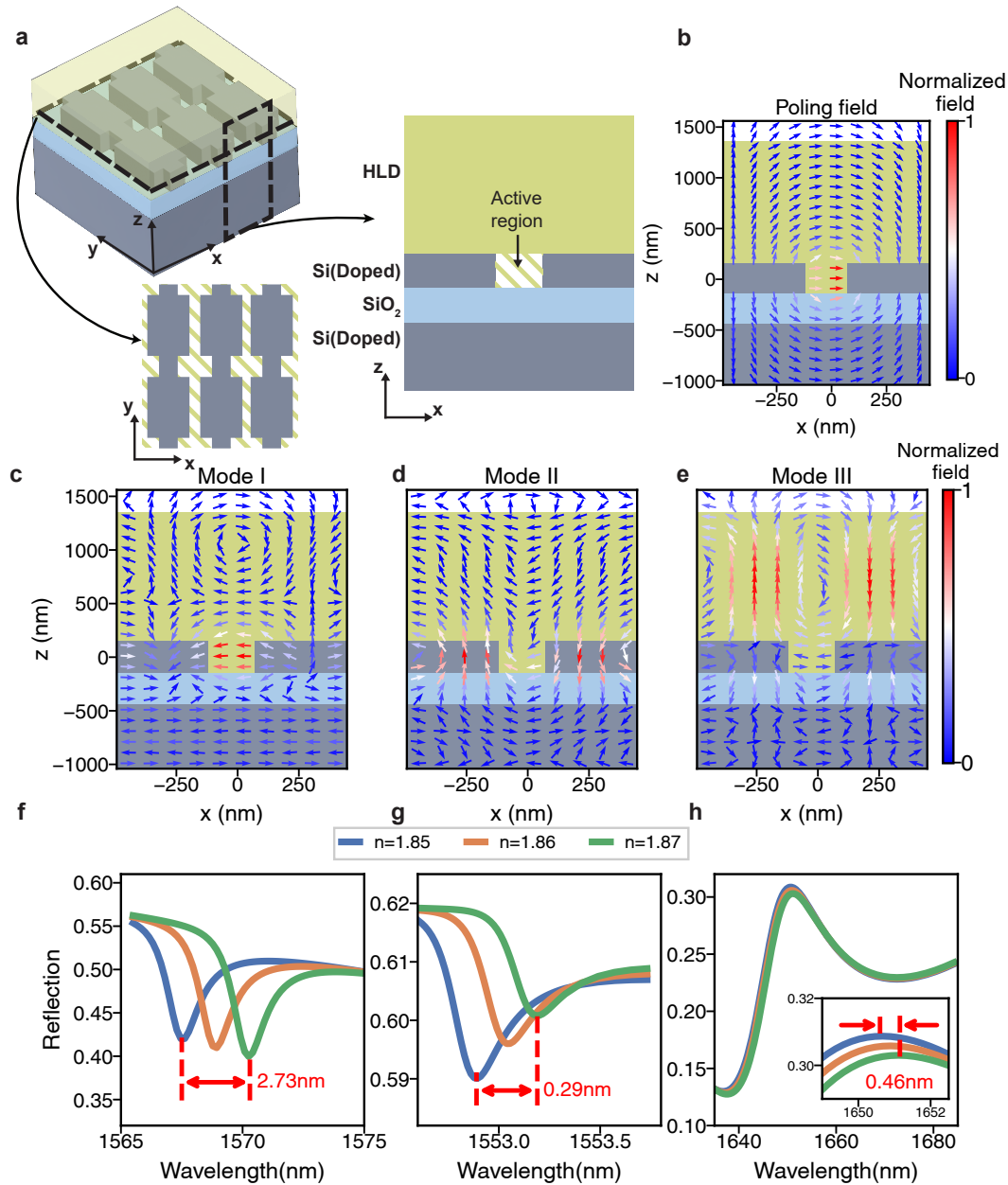
Figure 5.2: **The advantage of slot mode resonance in organic electro-optic modulators. a**. The schematic view (top left), top view (bottom left) and cross-section (right) of the device that supports the slot mode. In the schematic view the OEO material is plotted transparent to show the slot structure underneath. The slots are formed in the device layer of the silicon-on-insulator (SOI) substrate which is covered by the OEO material HLD. To show the essence of the problem, only the slot is considered as the active region. The dashed rectangles in schematic view represent the top view across the device layer and the cross section of a period cell. **b**. The poling field profile when the left and right silicon rail have bias voltages V(V>0) and 0, respectively. **c-e**. Normalized electric field profiles for three optical modes that could couple to E_x incident light. **c**. the slot mode. **d**. the guided mode in the silicon bar. **e**. the guided mode in the OEO material. **f-h**. the tuning performance of the three optical modes. Figures f, g and h match with the field profile in figures c, d and e, respectively. The inset in h is a zoom-in spectrum between 1649nm and 1652.5nm.

we assume that only the OEO material inside the slot is nonlinearly active. The structure will host various optical modes, many of which have a significant E_x field component such that it could strongly overlap with the incident E_x beam. Fig. 5.2c-e show three cross-sectional optical mode profiles (Mode I, II, III) originating from different parts of the device. The cross-sections are cut at the same y position as in Fig. 5.2b. Mode I is the slot mode, which has the field highly confined inside the slot, as discussed above, even upon applying the notch perturbation. Mode II is the bounded state guided within the slab. Notice that besides the slot mode, periodic notches also unlock the free-space radiation for this guided mode in the slab [95]. Mode III is a guided mode in OEO material, which has also been reported in [122]. Unlike the other optical modes, the field in slot mode is well aligned with the poling field and thus has the highest overlap factor Γ_c. As a result, under the same bias voltage, the slot mode has the largest resonance shift, as demonstrated through the simulation results in Fig. 5.2g-i. With the same amount of index change in the active region, Mode I, II, and III have resonance shifts of 2.73nm, 0.29nm, and 0.46nm, respectively. A more accurate model estimates the overlap factor by considering the orientation of the nonlinearity[122] (see the derivation in section 5.8). The calculated Γ based on this model for modes I, II, and III are 0.156, 0.017, and 0.015, respectively. The slot mode shows an order of magnitude higher Γ_c, compared to the others. Therefore, the slot mode is crucial for low-voltage modulation in silicon-organic metasurfaces.

We experimentally realize the concept discussed above, using a silicon-on-insulator (SOI) wafer. The device's cross-section, top view, and voltage setting are schematically illustrated in Fig. 5.3a-b. The detailed device parameters are shown in table 5.A.2. The nanostructures are fabricated with conventional nanofabrication techniques (see details on the fabrication procedure in section 5.8). The step-by-step zoom-out scanning electron microscopy(SEM) images (prior to spin-coating of OEO material) are shown in Fig. 5.3c-f. Doped silicon nano-bars have a resistance of $1 \sim 10\Omega \cdot$ cm, and $\sim$ 100nm wide gold strips along the nano-bars are added to further reduce the voltage drop across the silicon. In Fig. 5.3c, the gold strips are deliberately aligned at the center of the silicon rail so that only minimal absorption is introduced (See the discussions regarding the effect of metal strips in Fig. 5.A.5 in section 5.8.) Fig. 5.3e shows an $80 \times 100 \ \mu m^2$ device. Multiple devices are fabricated on a chip as shown in Fig. 5.3f for increasing the tolerance of the fabrication errors and testing multiple geometric parameters. After the coating of the OEO material, the device is wire bonded to a customized printed circuit board for poling
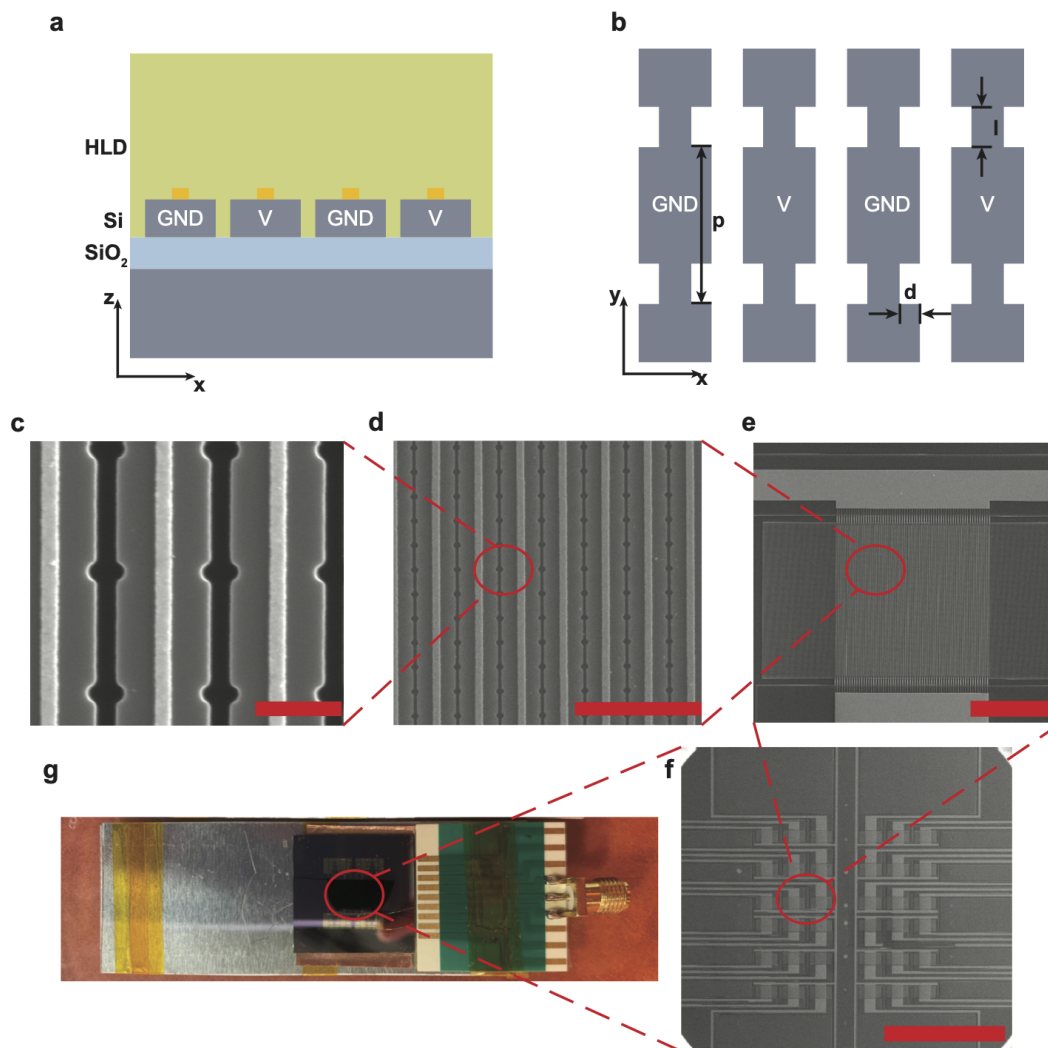
Figure 5.3: **The electro-optic free-space modulator. a-b**. The cross-section and top view of the experimentally fabricated device. **c-g**. The step-by-step zoom-out image of the device and setup. c-f are the scanning electron microscopy (SEM) images. The scale bars are 500nm, 3μm, 50 μm, and 1 mm, respectively. g is the optical image of the device. Multiple devices are fabricated within a chip, and they are wire-bonded to the printed circuit board for parallel testing.

and operating, as shown in Fig. 5.3g.

5.3 DC experimental results

To experimentally verify the relationship between resonant optical characteristics of the slot modes and the geometry of the device, we have fabricated several devices having different design parameters and compared their measured optical properties with corresponding numerical calculations (see Fig. 5.A.2 for details in optical

measurement setup). Fig. 5.4 shows the calculated and measured spectra of the slot mode resonances with different geometries. We characterize the slot resonances by varying the notch period and notch size in Fig. 5.4a-b and Fig. 5.4c-d, respectively. In Fig. 5.4a-b, we observe that a 20nm increment in notch periodicity leads to ~ 21.6nm and 22.2nm average redshift of the resonance in simulation and experiment, respectively. Also, with respect to the resonant wavelengths, the resonance amplitudes, and the spectral shapes of the resonance, the measured spectra in Fig. 5.4c show good agreement with the calculated spectra in Fig. 5.4d. In particular, the quality factor increases with the decrease of the resonance amplitude.

This trade-off is mainly due to the decreasing radiation rate to the top port (to $+z$ direction), which results in the under-coupling between the slot mode and the illuminated light from the top [64]. Specifically, the amplitude of the resonance is determined by the ratio of the mode coupling rate between the input light and the slot mode to the sum of other undesired decay rates [130]. The undesired decays include absorption in the gold layer, scattering from the rough sidewalls or finite edge of the chips, and radiation to the oxide layer or the silicon substrate. As the absorption in the gold layer and the radiation to the silicon substrate are nearly inevitable in the proposed planar structures, the trade-off between the resonance amplitude and the quality factors is inevitable especially when the coupling rate decreases. The proposed devices in Fig. 5.4e can achieve modulation amplitude over 10% and Q-factor over 1000 in the experiment even with the absorption in the gold. Operation results under DC bias are shown in Fig. 5.5. Fig. 5.5a-c show the results from three different devices under maximum bias voltages before any dielectric breakdown. The variation in the breakdown voltages results from the quality of the OEO material preparation and fabrication quality. The maximum absolute frequency shift of 5.5nm is achieved under ±17V in Fig. 5.5a, and the spectral shift per unit external DC bias is $S_{abs} = \Delta\lambda/\Delta V = 0.161$nm/V, which is ~ 1.6× higher than that of the previously reported tunable free-space optical modulators [110]. Using Eqs. 5.1 and 5.2, r_{33} in-device is calculated at 45.7 pm/V at 1495nm. In Fig. 5.5b and c, 2.3nm and 2.6nm resonance shifts are observed with ±11V and ±12V bias voltages, respectively. Figures 5.5b and c show high Q-factors over 1000. The increase in Q-factor also improves the normalized modulation figure-of-merit ($S_n = \Delta\lambda/(\text{FWHM} \cdot \Delta V)$ [131]. In our best-performing device shown in Fig.5.5b, S_n is 0.09/V, which is an order of magnitude higher than other reported devices[131]. The reflection spectra are plotted in Fig. 5.5d as a function of different bias voltages. The spectra clearly show the bidirectional linear relationship
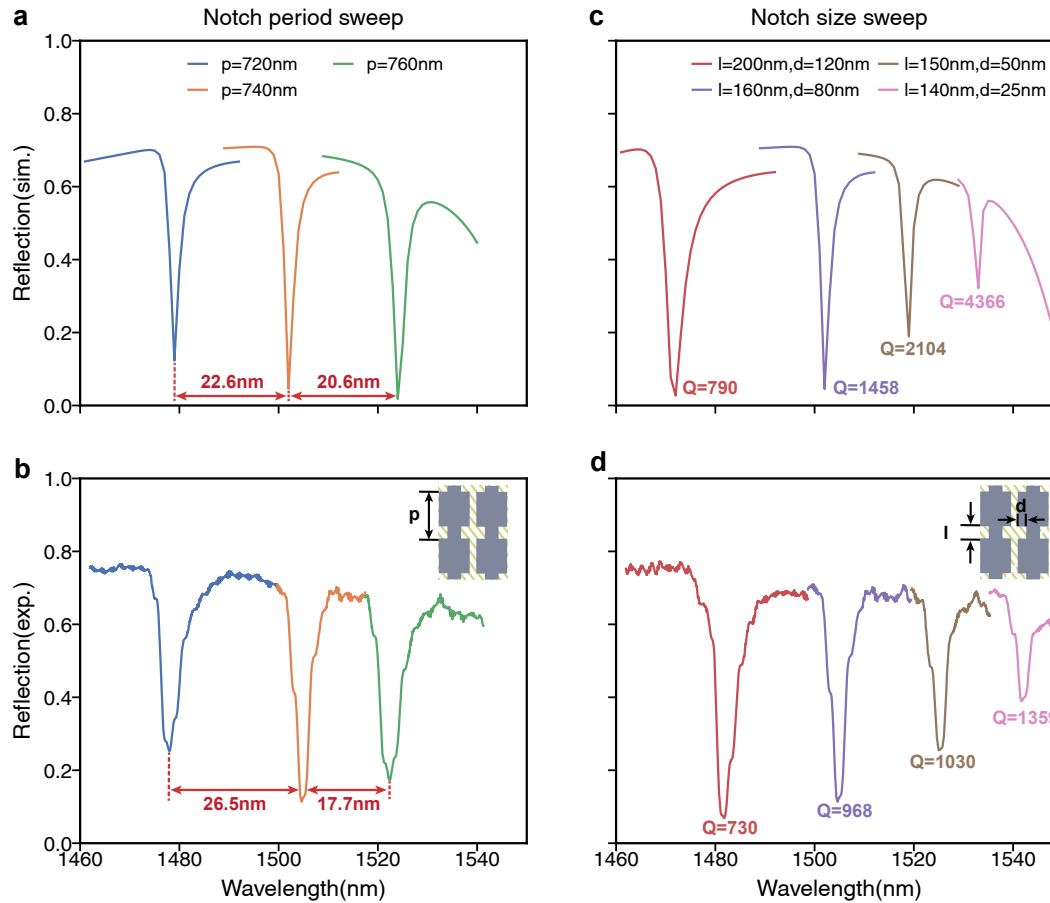
Figure 5.4: **Slot mode resonance characterization. a-d** The simulated (a,c) and experimentally measured (b,d) reflection spectra when sweeping different sets of perturbation parameters. a-b. Sweep the periodicity of the notches. All curves have the same notch size $l = 160$nm, $d = 80$nm. Blue: $p = 720$nm. Orange: $p = 740$nm. Green: $p = 760$nm. The resonance shifts due to periodicity changes are labelled in experiment and simulation curves. c-d. Sweep the notch sizes. All curves have the same notch periodicity $p = 740$nm. Red: $l = 200$nm, $d = 120$nm. Purple: $l = 160$nm, $d = 80$nm. Brown: $l = 150$nm, $d = 50$nm. Pink: $l = 140$nm, $d = 25$nm. The quality factor of the resonances are labelled for experimental and simulated plots.
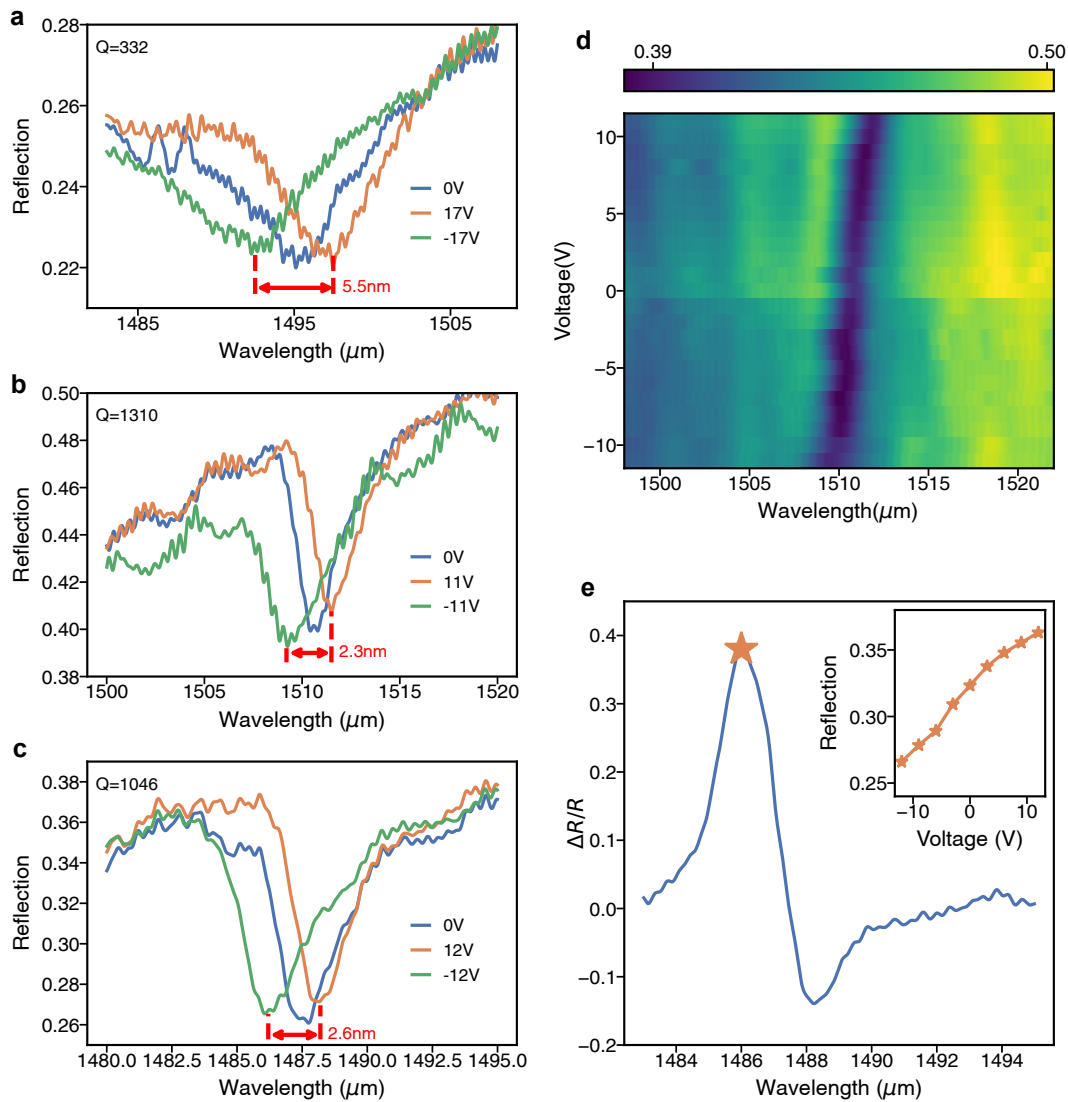
Figure 5.5: **DC tuning characteristics. a-c**. Reflection spectra of three different devices under DC tuning. The applied biases are denoted in the legend. **d**. The reflection spectra of the device in **b** with bias voltages ranging from -11V to 11V. **e**. The maximum modulation ratio ($\Delta R/R = (R_{max} - R_{min})/R_{V=0}$) for each wavelength in device shown in **c**. The inset depicts the absolute reflection as the DC bias voltage is swept from -12V to 12V for a fixed wavelength of incident light of 1486nm. The absolute reflection changes over 10%.

between the bias voltage and the resonance shift, confirming that the spectral shift results from the electro-optic effect[122]. In Fig. 5.5e, the relative modulation ratio, $\Delta R/R$, from the device in Fig. 5.5c is plotted. The maximum modulation ratio is over 40%. It is worth noting that the asymmetry of the modulation is due to the Fano shape of the resonance [61]. The inset in Fig. 5.5e, shows the reflection intensity as a function of the bias voltage when the input light wavelength is 1486.5nm. From -12V to $+12$V, the reflection amplitude is gradually increasing.

5.4   AC experimental results

The AC modulation characteristic is tested with the devices in Fig. 5.5a and plotted in Fig. 5.6a. A sine wave with peak-to-peak value, V_{pp}, of 20V is applied into the device while the wavelength of the incident light is set at 1490nm where the device achieves the highest modulation depth (estimated as 6.8% from Fig. 5.5a). The sine wave frequency is swept from 50kHz to 5.8MHz. The cutoff 3dB bandwidth is at 3MHz. The insets in Fig. 5.6a show the normalized modulation signal when driving with frequency f=80kHz and f=2.8MHz, respectively. To investigate the AC response, we use a simplified model to predict the AC response shown in Fig. 5.6b. The model collectively considers the contributing factors to the response speed within and outside the devices. In the devices, we model the nano-bars as a resistance including the contribution from the gold strip R_{Au} and the silicon nano-bar R_{Si} (see supplementary section 4). The slot is modeled as the parallel connected resistance R_{OEO} and capacitance C_{OEO}. Outside the devices, we assume that the major electrical components are the stray capacitance in the circuits, which are split into the capacitance due to the SOI wafer [132] C_{SOI} and other factors C_{load}. The parameters in the model are determined by both the geometry of the devices and the AC response of similar devices with different substrates or electrode layouts (See supplementary section 4). The AC response from the prediction of the model is shown as the green line in Fig. 5.6a, which agrees with the experimental result. Based on the model estimation, the capacitance from the silicon-organic platform and the stray capacitance along the whole circuits are the main factors preventing the speed increase. The capacitance from the SOI wafer could be solved by advanced CMOS technology used in integrated electro-optic modulators [133]. Judicious material and structural engineering of these circuits have already achieved gigahertz operation of electro-optic modulators [100, 110, 134, 135]. As a result, there is no fundamental limit in increasing the operation speed up to GHz in our platform.
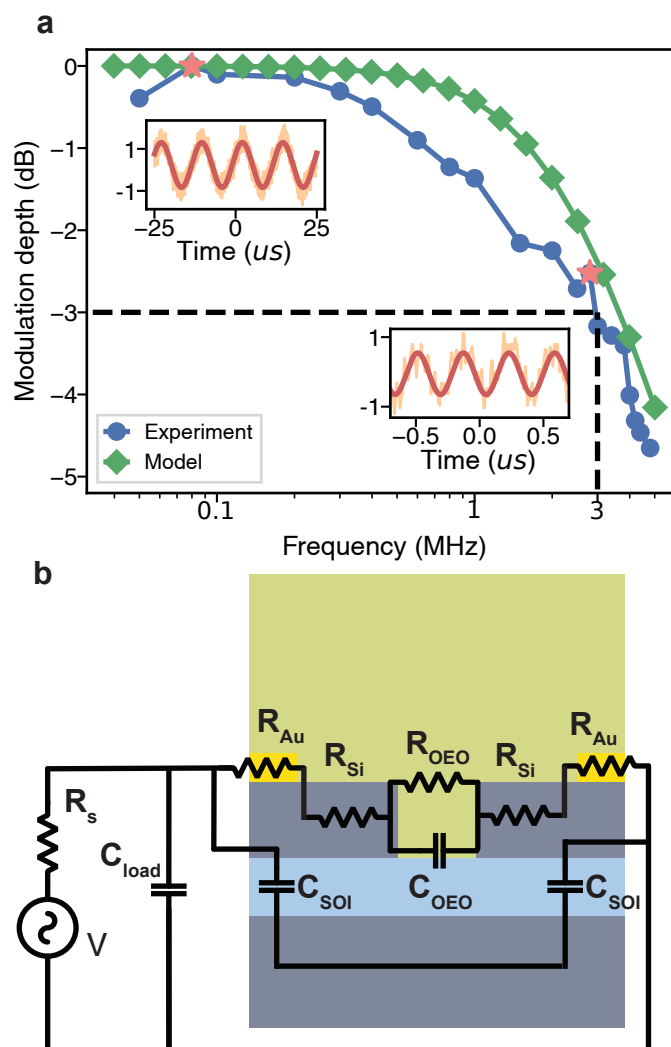
Figure 5.6: **AC tuning characteristics and circuit model scheme. a.** The experimental and modeled AC response of the active device. Blue curve: the experimental normalized modulation depth. The cutoff bandwidth is at 3MHz. Green curve: the model prediction of the modulation depth. Insets: the example modulation signal (Orange) and the fitting sine wave (Red) in the time domain. The frequencies of the modulation signal are 80kHz (top left) and 4MHz (bottom right), respectively. **b.** The circuit model of the device. V: the voltage source. R_s: the source resistance. C_{load}: external stray capacitance outside the device. C_{SOI}: the capacitance due to the use of SOI wafer. R_{Au}: the resistance of the gold strip on top of the silicon nano-bar. R_{Si}: the resistance of the silicon nano-bar. C_{Poly}: the OEO material capacitance. R_{Poly}: the OEO material resistance.

5.5 Phase modulation design

In previous sections we discussed about the use of slot mode to reduce the driving voltage of silicon-organic devices. In fact, the device structure shown in Fig. 5.3 is close to the simplest one in terms of the fabrication perspective; it starts with an SOI wafer, using two steps of lithography to pattern the slot and the electrode, then coating the OEO material (see Fig. 5.A.1 for detailed fabrication flow). On the other hand, the condition of the structures to support a slot mode only require two layers (organic electro-optic material and silicon device layer). The gold electrode is necessary to transmit the driving signal, and its position has been optimized to minimize the induced loss. However, the layers below the slot and above the OEO material haven't been explored. We could engineer them to achieve more ambitious goals. For example, switching the substrate from SOI to fused silica could improve the AC bandwidth[110]. In this section, we also discuss about the potential extension to the phase modulation.

Currently, the slot mode in our proposed structure couldn't have large phase modulation results. In section 2.6, we discussed several methods to enhance the phase response using optical modes. Several method could be applied to the silicon-organic platform.

Without mirror

In section 2.6, a low background reflection r would make it easier to achieve an overcoupled mode. Therefore, we need to adjust the geometry parameters to find the region where the background reflection is relatively low. Here we present a design example of the results in Fig. 5.7.

The geometry parameters are described in Table. **??**. Fig. 5.7a shows the background reflection r, where we approximate this term by removing the notch of the slot. Since the slot mode is fully decoupled from the incident light, the contribution of the reflection only includes the background term. We can see that the reflection $r < 40\%$, which is smaller than previous design in Fig. 5.4. Fig. 5.7b-c show the reflection amplitude and phase as a function of refractive index and wavelength, respectively. The wrapped curve of phase response clearly shows the overcoupled regime of the slot mode. We also note that the minimum reflection amplitude is around 4% and the maximum reflection amplitude is around 57%. Therefore, although the mode is overcoupled, the variation of the reflection amplitude is still relatively large. This design is not ideal for a pure phase modulator.
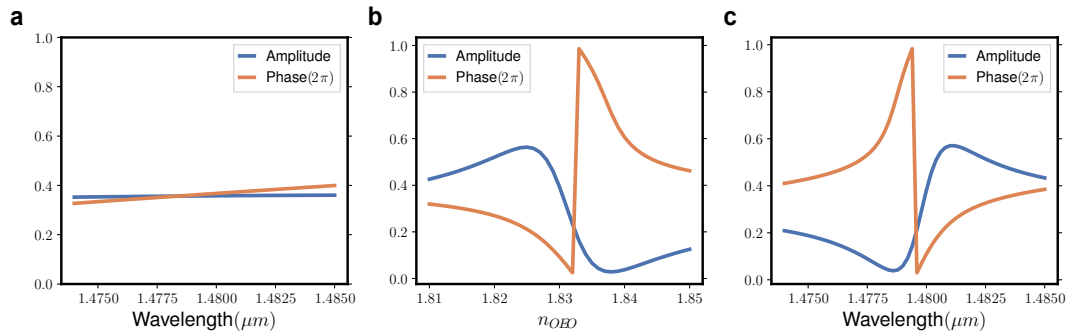
Figure 5.7: **Design example of enhanced phase response without gold mirror. a.** The amplitude and phase response as a function of incident light wavelength when there is no notch perturbation. **b.** The amplitude and phase response as a function of OEO material refractive index. **c.** The amplitude and phase response as a function of incident light wavelength.

With mirror

The non-perfect reflective response of the no-mirror design calls for the design with mirror. Directly blocking the radiation from one port still has its own advantage and worth being discussed. In our silicon-organic platform, we could block the radiation from top port or bottom port. Consequently, we could add a gold mirror on top of the OEO material or below the BOX layer, shown in Fig. 5.8a and d.

If we choose to add a top mirror, the incident light direction has to be in $+z$ from below the device. The bottom of the device has to be polished, but the fabrication process only requires one extra deposition step. Adding the mirror introduces another design parameter h_p, which is the polymer height. Previously h_p is not crucial since the field exponentially decays above the slot. However, if h_p is crucial in determining the reflective response, since if h_p is too small, the plasmonic absorption induced by the metal layer will reduce the overall reflection amplitude and the decrease the 'loss ratio' of the bottom port. On the other hand, higher h_p will help with the uniformity of the OEO layer. Thus it is preferred to choose higher h_p if possible. In Fig. 5.8b-c, we choose $h_p = 1\mu m$, which is compatible with the fabrication procedure of the HLD OEO material. The required refractive index modulation is only 0.01, and the overall reflection is over 70% with variation in 10%. It is a better design for phase modulator.

Since we spin coat the OEO material onto the device after the nanostructure fabrication, the thickness of the OEO material couldn't be controlled exactly. Adding the gold layer at the bottom will incorporate the metal layer deposition into the device
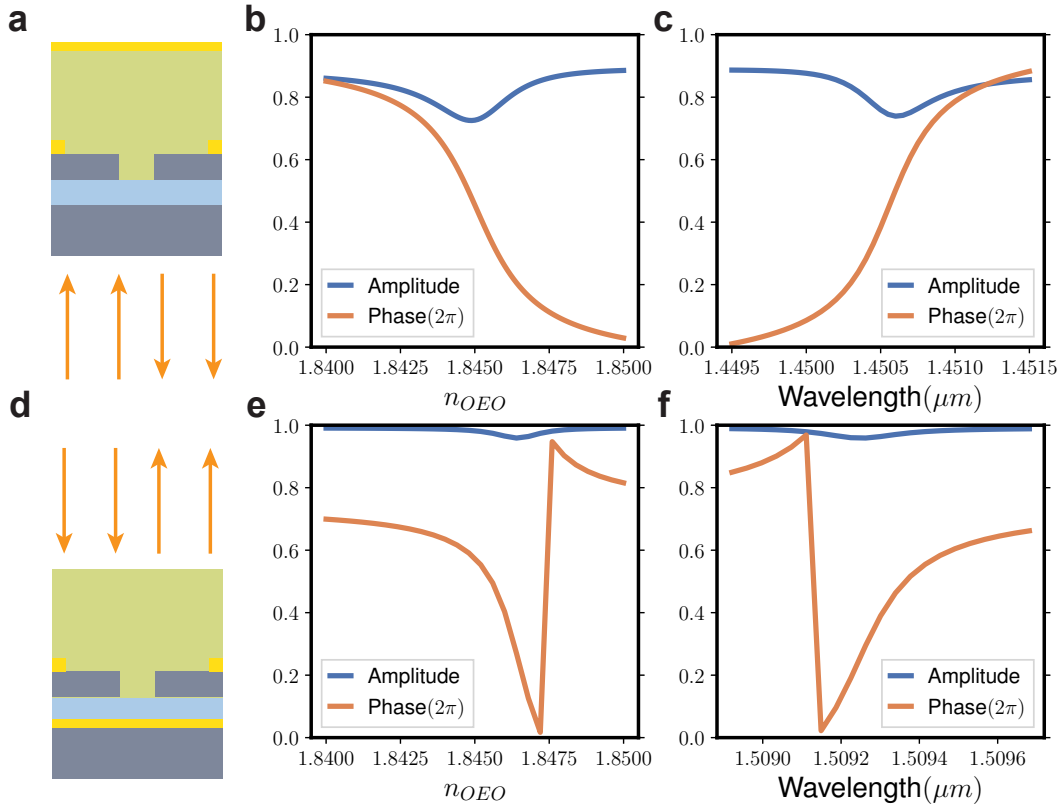
Figure 5.8: **Design example of enhanced phase response with gold mirror. a.**
The light is incident from the backside of the device and reflected back. **b-c.** The
amplitude and phase response of the designed device in a. b. The refractive index
sweeps from 1.84 to 1.85 at incident wavelength $1.4496\mu m$. c. The wavelength
sweeps from $1.4495\mu m$ to $1.4515\mu m$. **d.** The mirror is between the oxide layer
and the substrate. The light is incident from the top. **e-f.** The amplitude and phase
response of the designed device in d. e. The refractive index sweeps from 1.84 to
1.85 at incident wavelength $1.5088\mu m$. f. The wavelength sweeps from $1.4495\mu m$
to $1.4515\mu m$.

fabrication process, and therefore we have more controllability on the position of
the metal layer. In Fig. 5.8d, an new parameter h_{SiO2} is introduced. We select
$h_{SiO2} = 300nm$ in the design. Since the distance is larger, the absorption is much
less and we achieved more than 90% reflection on resonance.

In conclusion, from a fabrication perspective, we explored three designs in this
section, from the simplest one to the most difficult one. The design without mirror
has to suffer from low and non-uniform reflection amplitude. The design with
the top mirror has relatively low yield due to the uncertainty of the OEO material
thickness. The design with the bottom mirror will have the best performance, but
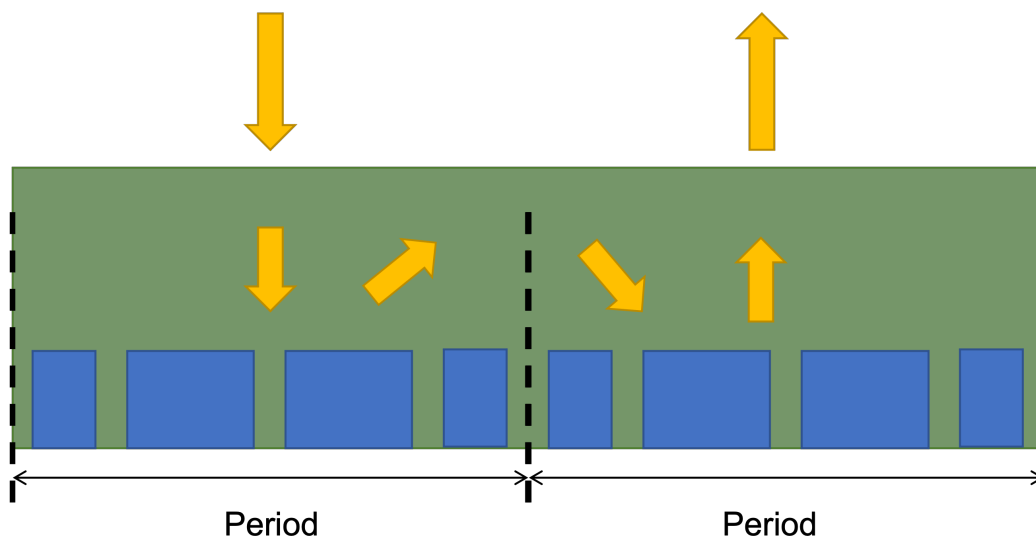
Figure 5.9: **The crosstalk mechanism when period is larger than λ_{OEO}.** When the period length is between λ_{OEO} and λ_{air}, the power diffracted within the OEO layer will be fully reflected and transferred to adjacent period structures.

the difficulty for developing the fabrication recipe is a challenge.

5.6 Beam steering design

The design with the bottom mirror shows ideal performance so that we could further explore the spatial light modulation. As shown in Chapter 4, the slot mode with enhanced phase response could enable wavelength-scale spatial modulation. However, sub-wavelength level control couldn't be realized here even with the trick of block[108] in the scenario we discussed here[1]. We show the physical reason in Fig. 5.9. Our OEO material has refractive index around 1.8, where the effective wavelength is around $\lambda_{OEO} = 860nm$. To prevent the diffraction in air, the size of the pixel has to below the wavelength in air λ_{air}. If the pixel size is between λ_{OEO} and λ_{air}, the diffraction within the OEO material layer will transfer the power into the adjacent pixel, shown in Fig. 5.9. If the pixel size is smaller than 860nm, the direct crosstalk between the pixels couldn't be blocked anymore.

To still enable the individual pixel modulation, our method is to use the 'supercell' pixel in Fig. 5.10. One pixel includes several identical periodic cells, and controlled by one bias voltage. The pixel size increases multiple times, but the crosstalk is significantly suppressed, since the crosstalk area within the same pixel is much less affected. We gradually increase the number of periods within a pixel, and find out

---

[1]$\lambda_{air} = 1.55\mu m$ target wavelength, feature resolution around 100nm, silicon-organic platform
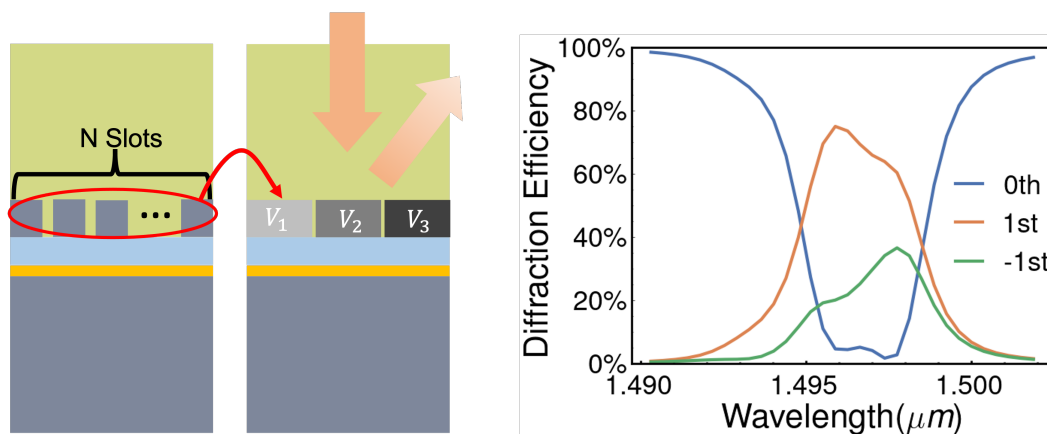
Figure 5.10: **Beam steering device scheme and response.** Left: The beam steering device shceme. *N* periods form one individual addressed pixel. Each pixel provides a phase response. Right: the performance of the 3-pixel beam steerer when *N* = 12. 1st order diffraction is over 70% at the maximum wavelength.

that using 12 periods as a pixel (N=12) leads to over 70% diffraction efficiency. In this design, the pixel size in *x*-direction is $12\mu m$, and it is comparable with current commercial opponents.

5.7   Discussion

In this work, we propose a silicon-organic metasurface for free-space modulation with reduced operation voltage less than ±17V. We experimentally observed the resonance with quality factor 330-1310 and up to ∼ 5.5nm shift with nonlinear coefficient r_{33} = 45.7pm/V at 1495nm. The proposed slot mode combines the advantages of a short distance between two electrodes and a large overlap with the OEO material, achieving a tuning sensitivity S_{abs} = 0.161nm/V, which shows an improvement with a factor of 1.6 in sensitivity compared to the state-of-art [110, 131]. Finally, the metasurface has up to 3MHz bandwidth. The use of the slot mode is not limited to electro-optic systems. The proposed design approach can be applied to any system where sensitivity to perturbations in low-index media is critical. For example, in NEMS systems, the slot mode resonance could potentially improve sensitivity to the mechanical movement, compared to conventional guided mode resonances [70].

The currently demonstrated sensitivity is limited by the quality factor and the nonlinear coefficient r_{33}. The quality factor could be improved by using smaller notches or a refined fabrication process. The relatively low nonlinear coefficient compared to what we expected[120] is partly due to the surface state of doped silicon used as the

electrode[136] and the small width of the slot[129]. Barrier layer protection[137] has the potential to increase the nonlinear coefficient r_{33} by 4-5 times [138], reducing the tuning voltage down to CMOS-level. Judicious doping level adjustments and the microwave coplanar waveguide design could enable GHz speed operation[110, 125]. Therefore, with the increase of electro-optic coefficient and operation bandwidth, our platform is a potential solution for GHz free-space modulation at the CMOS level voltage.

This study primarily focuses on structures which are periodic in both x and y dimensions. However, it is not a necessary condition for preserving the slot mode. As a mode propagating along the y direction, the slot mode doesn't necessitate periodic conditions in x direction [108]. By varying the geometry of the slots, individual slot modulation could be potentially achieved. In the y-dimension, by introducing high contrast index variations or photonic crystal mirrors, the footprint of the resonant device could be reduced considerably [139, 140]. Furthermore, the proposed devices expect to achieve phase modulation if the overcoupling condition is satisfied by the out-of-plane asymmetry in nanostructures [66] or a bottom mirror [27, 28].

In summary, this report presents a low-voltage amplitude modulator using a silicon-organic platform. The slot mode metasurface has the potential to enable high-speed and low-voltage optical switching, sensing, and tuning, for numerous applications such as LiFi, LiDAR, spatial light modulators, and quantum optical communication.

5.8   Appendix

Fabrication and poling methods

The device is fabricated from an SOI (silicon on insulator) wafer, which consists of 300nm device p-doped silicon ($1 - 10\Omega \cdot$ cm), 300nm BOX (buffered silicon oxide), and $500\mu m$ silicon substrate. The detailed fabrication workflow is shown in Fig. 5.A.1. The device requires two sequential nanofabrication steps for the silicon rails and metallic strip. Both E-beam lithography steps utilize ZEP-520A (Zion Corporation) as the resist, 100kV electron beam (EBPG-5200, Raith GmbH) to expose, and ZED-N50 (Zion Corporation) as the developer. After the first E-beam lithography, we use the resist as the soft mask and the pattern is transferred to silicon by ICP-RIE etching (PlasmaLab System 100, Oxford Instrument). Next, the resist is removed by Remover PG. The second E-beam lithography writes the liftoff mask for the electrodes, following which 5nm Ti and 60nm Au are deposited sequentially using an E-beam evaporator (Kurt J. Lesker E-beam evaporator). Liftoff
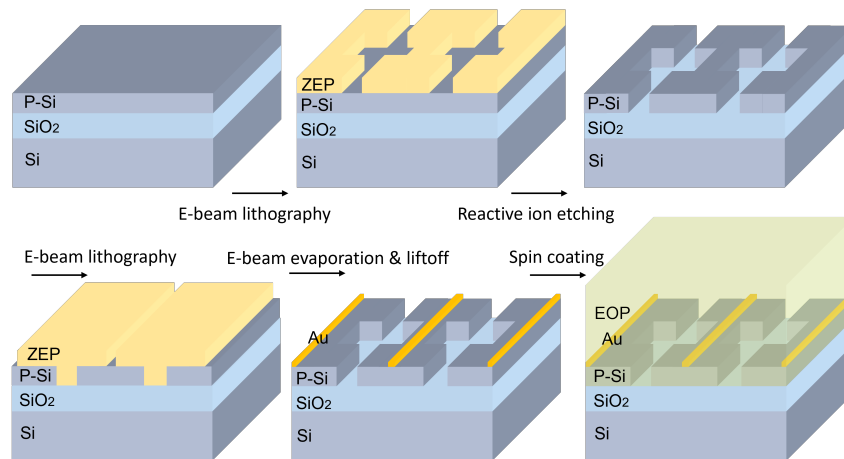
Figure 5.A.1: **Fabrication workflow.** Top row: the fabrication of the slot by E-beam lithography and ICP-RIE etching. Bottom row: the fabrication of the electrode by metal liftoff and the coating of the polymer.

is then performed in Remover PG. Finally, a layer of OEO material (HLD, NLM Photonics) is spin-coated on top of the device, followed by a 3-hr solvent removal in a vacuum oven at $65°C$. Poling of the HLD material is performed by heating the device under the nitrogen environment while applying a poling voltage. This voltage creates a poling field around $100V/\mu m$ across the slot. The heating process consists of a $6°$ C/s temperature ramping, 5 to 10 minutes of holding at $95°$, and rapid cooling.

Simulation methods

The simulations in Fig. 5.2 and Fig. 5.A.3 use COMSOL Multiphysics software. The periodic condition is applied in both x and y directions. Refractive indexes of the silicon, silicon oxide, and OEO material are assumed to be 3.52, 1.44, and 1.85. Fig. 5.4a,c are simulated with FDTD (Lumerical) with periodic boundary conditions applied in x and y.

Measurement

The measurements were conducted using the experimental setup depicted in Fig. 5.A.2. The light source utilized was a tunable external-cavity diode laser (Toptica CTL-1550). A fiber collimator (Thorlabs, F260FC-1550) was employed to collimate the beam. A beam splitter is placed in front of the collimator to split a small amount of power for the reference InGaAs detector (Thorlabs, PDA10CS). The polarized state of the incident light was set to TE polarization using a linear polarizer. Then
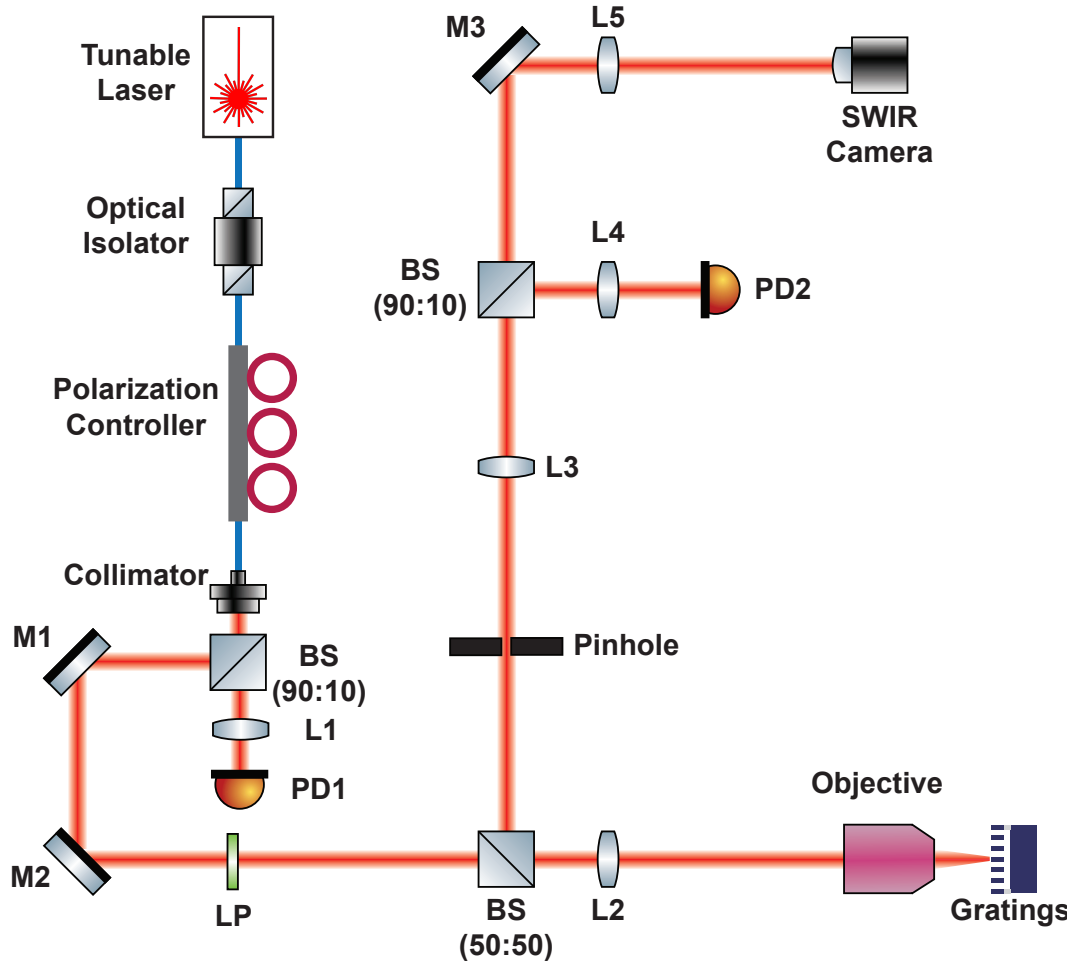
Figure 5.A.2: **Schematic illustration of the experimental setup.** Red lines indicate paths of light propagation. LP: linear polarizer. BS: beamsplitter. L: lens. PD: photodetector. M: mirror. Obj.: microscope objective lens. SWIR camera: short-wave infrared camera.

the light goes through a beam splitter and only half of the power is used. A ×20 infinity-corrected objective lens (Mitutoyo, M Plan Apo NIR) and a tube lens with a focal length of 200mm were used to image the sample at the object plane, with the tube lens and the mounting stage of the sample adjusted to ensure normal incidence. An iris (Thorlabs, ID25) was inserted at the image plane to select a region of interest with a diameter of 45μm in the object plane. The spatially filtered light was either focused onto another InGaAs detector for the measurement of the spectra or imaged on an InGaAs SWIR camera (Goodrich, SU320HX-1.7RT) using relay optics. The reflection signals were obtained by dividing the signal from the sample by the signal from the sources. It should be noted that due to different input polarization states, the incident power onto the sample varied at different wavelengths. Thus, the signals
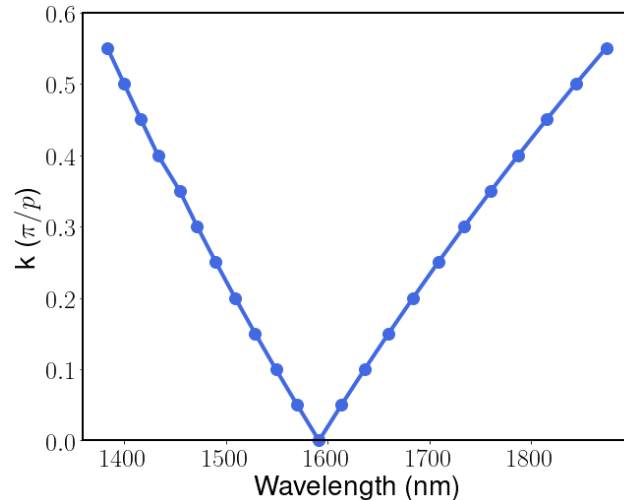
Figure 5.A.3: **Band diagram of the slot mode without perturbation.** The calculated slot mode wavelength for different in-slot momentum k_y along the slot. The in-slot momentum is wrapped under the unit of π/p where $p = 740nm$. At $\lambda = 1591.6nm$, $k_y = 0$, indicating that the perturbation in the $740nm$ period will open the resonance at this wavelength.

were further normalized by the signals from the exposed gold pad on the chip.

Creation of the slot mode resonance in OEO polymer device

In this section, the principle of slot mode resonance creation is discussed. The idea comes from previous research on high-Q resonances[94, 95]. In integrated photonics, a slot waveguide is used for light propagation because its momentum is larger than the momentum of free-space light. This bounded-state property guarantees zero radiation loss in the ideal slot waveguide. However, the subtle periodic perturbation will compensate for the momentum mismatch and enable the radiation into the free space. For example, by targeting $k_y = 0$, we can couple the slot waveguide to the z-incident light, as illustrated in Fig. 5.1 of the main manuscript. Specifically, the slot mode has a dispersion relationship shown in Fig. 5.A.3. We wrap the dispersion curve within the range of π/p. Under this operation, the curve reaches $k_y = 0$ at a specific wavelength of $\lambda = 1591.6nm$. In other words, under the perturbation with period p, k_y will be wrapped to 0 and thus couples to the normal incident light. We also numerically confirm the existence of the resonance in Fig.5.A.4 and the properties of perturbations. Simulations reveal three effects depending on the notch size: the blue shift from the non-perturbed resonance wavelength, the quality factor, and the modulation amplitude. Firstly,
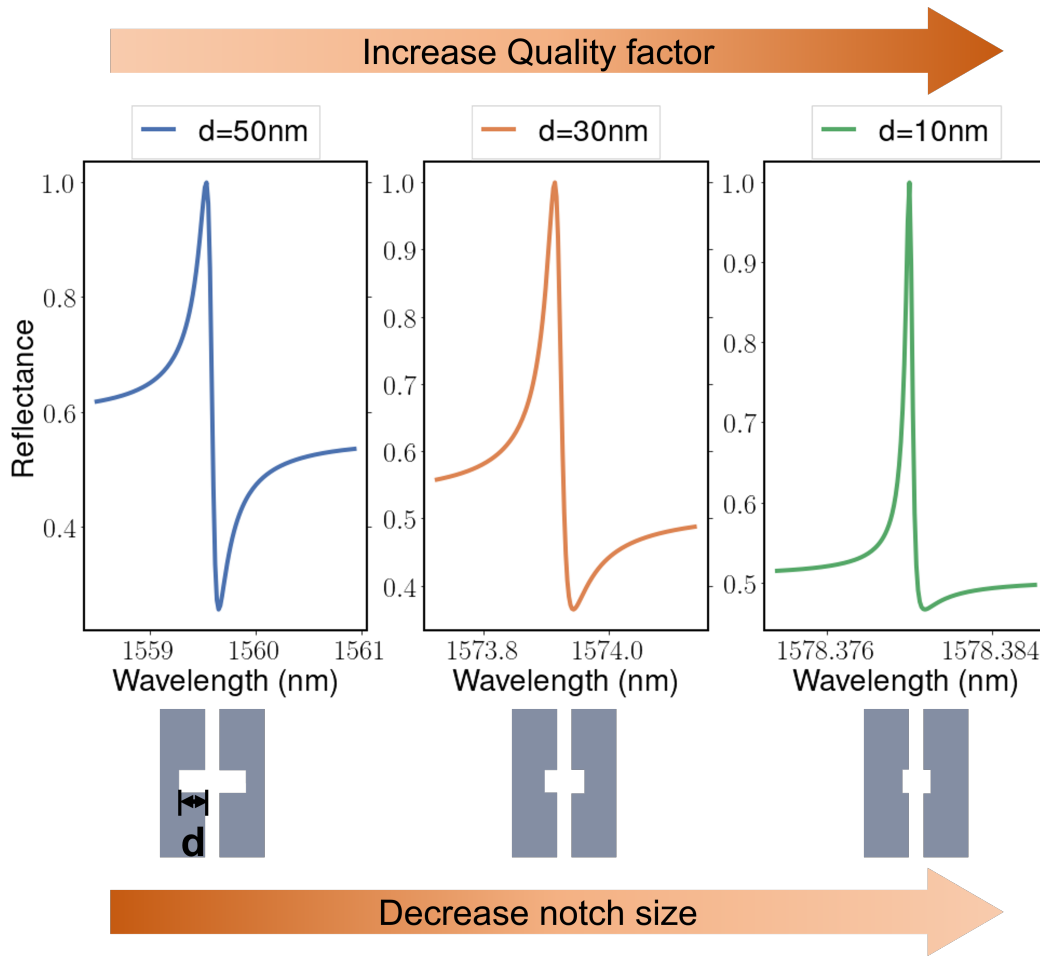
Figure 5.A.4: **Creation of the slot mode resonance.** From left to right: the reflection spectra when decreasing the width of the notch d from $50nm$ to $10nm$. The simulated structure is the same as shown in Fig. 5.2 of the main manuscript.

the geometrical perturbation by creating notches leads to the blue shift according to the first order perturbation theory[46]. Secondly, the quality factor increases as the perturbation disappears. This indicates that the notch size controls the radiative loss of the slot mode, and it is the origin of the resonance. Thirdly, shown in Fig. 5.4 of the main manuscript, the smaller the notch size, the smaller the modulation amplitude, which is the result of the decreasing coupling rate. In conclusion, the notch size and notch period are two powerful knobs that enable resonance creation at a large range of wavelengths and with arbitrary quality factors.

Calculation of the overlapping factor

The interaction strength between the polymer and optical mode has previously been investigated, including that between polymer and guided mode[122] and that

between polymer and non-perturbed slot mode[141]. The calculation formula of the overlapping factor (Γ_c) has been proposed in equation (24) in the supplementary material of reference[122], under the quantum picture. Here, we will provide another derivation of the same equation from the cavity perturbation theory[46].

The basic picture of the electro-optic-induced resonance shift could be decomposed in several steps. First, the mode frequency shift is caused by the local dielectric tensor perturbation $\Delta\bar{\bar{\epsilon}}$. Second, the local anisotropic dielectric tensor perturbation is generated by tuning the electric field $\mathbf{E}_{\text{ext}}$ under non-negligible electro-optic coefficient r_{33}. Third, the direction and the amplitude of r_{33} depend on the poling electric field $\mathbf{E_p}$. Note that the bold variables $\mathbf{E}_{\text{ext}}$, $\mathbf{E_p}$ means they are vectors, and all these variables are dependent on the locations. We will walk through the calculation step by step.

In the first step, the ith mode frequency shift $\Delta\omega_i$ when we have a dielectric tensor perturbation could be easily calculated by perturbation theory [46]:

$$\frac{\Delta\omega_i}{\omega_i} = -\frac{1}{2}\frac{<\mathbf{E_i}, \Delta\bar{\bar{\epsilon}}\mathbf{E_i}>}{<\mathbf{E_i}, \bar{\bar{\epsilon}}\mathbf{E_i}>} \tag{5.3}$$

Here, $\mathbf{E_i}$ is the vector of ith mode field, $\bar{\bar{\epsilon}}$ and $\overline{\overline{\Delta\epsilon}}$ are the dielectric tensor of the material and its perturbation. The inner product is the integral across the region of one period in both x and y directions, and infinity in z direction:

$$\int_{-\infty}^{\infty} \int_{-p/2}^{p/2} \int_{-w_p/2}^{w_p/2} \mathbf{E_1}^{\dagger}\bar{\bar{\epsilon}}\mathbf{E_2}\mathrm{d}x\mathrm{d}y\mathrm{d}z :=< \mathbf{E_1}, \bar{\bar{\epsilon}}\mathbf{E_2} > \tag{5.4}$$

$\mathbf{E_1}^{\dagger}$ means the conjugate transpose of the vector. In the second step, the "local" perturbation of the dielectric tensor $\Delta\bar{\bar{\epsilon}}$ is dependent on "local" electro-optic coefficient r_{33}. The definition of the electro-optic coefficient is by relative impermeability $\bar{\bar{\eta}} = (\frac{\bar{\bar{\epsilon}}}{\epsilon_0})^{-1}$, and here we are only interested in non-negligible coefficient r_{33}[142]:

$$\Delta\eta'_{33} = r_{33}|\mathbf{E}_{\text{ext}}| = r_{33}E_{ext,z'} \tag{5.5}$$

We define a local coordinate system (x', y', z'), where z' axis is the same direction as the local poling electric field $\mathbf{E_p}$. $\Delta\eta'_{33}$ means that the variable is expressed in coordinate system (x', y', z'). Since the poling field and the tuning field use the same electrodes, thus under this local coordinate system the relationship between $\mathbf{E}_{\text{ext}}$ and $\Delta\bar{\bar{\eta}}$ is simpler (only $r_{33} \neq 0$ and $\mathbf{E}_{\text{ext}} = (0, 0, E_{\text{ext,z'}})^T$), shown in Equation 5.5. If we write the equation in tensor form, the result is

$$\overline{\overline{\Delta\eta'}} = \frac{\mathbf{E}'_{\text{ext}}\mathbf{E}'_{\text{ext}}{}^{\dagger}}{|\mathbf{E}'_{\text{ext}}|} \tag{5.6}$$

The transformation matrix between the local axis base vectors $\mathbf{e'_i}$ and the global axis base vectors $\mathbf{e_i}$ are defined by Q:

$$\mathbf{e_i} = Q_{ij}\mathbf{e'_j} \tag{5.7}$$

Then the dielectric constant perturbation could be expressed:

$$\Delta\bar{\bar{\epsilon}} = -\frac{1}{\epsilon_0}\bar{\bar{\epsilon}} \cdot \overline{\overline{\Delta\eta}} \cdot \bar{\bar{\epsilon}} = -\frac{1}{\epsilon_0}\bar{\bar{\epsilon}} \cdot Q\overline{\overline{\Delta\eta'}}Q^T \cdot \bar{\bar{\epsilon}} \tag{5.8}$$

$$= -\frac{1}{\epsilon_0}r_{33}\bar{\bar{\epsilon}} \cdot Q\frac{\mathbf{E'_{ext}}\mathbf{E'_{ext}}^\dagger}{|\mathbf{E'_{ext}}|}Q^T \cdot \bar{\bar{\epsilon}} \tag{5.9}$$

$$= -\frac{1}{\epsilon_0}r_{33}\bar{\bar{\epsilon}} \cdot \frac{\mathbf{E_{ext}}\mathbf{E_{ext}}^\dagger}{|\mathbf{E_{ext}}|} \cdot \bar{\bar{\epsilon}} \tag{5.10}$$

In the third step, we need to connect the local variant r_{33} with the poling and the tuning voltage. We define the poling efficiency k_p:

$$k_p = r_{33}/|\mathbf{E_p}| \tag{5.11}$$

Since we are using the same electrode for poling and tuning, $\mathbf{E_p}$ and $\mathbf{E_{ext}}$ follow the same distribution. For simplicity, we could define $\mathbf{E_p} = \alpha\mathbf{E_{ext}}$. k_p is a constant within the OEO region, and outside OEO region $k_p = 0$. α is number that is not dependent on the locations. Therefore, the inner product in equation 5.4 could be expressed as

$$< \mathbf{E_i}, \Delta\bar{\bar{\epsilon}}\mathbf{E_i} > = -\frac{1}{\epsilon_0} < \mathbf{E_i}, \bar{\bar{\epsilon}} \cdot k_p\alpha\mathbf{E_{ext}}\mathbf{E_{ext}}^\dagger \cdot \bar{\bar{\epsilon}}\mathbf{E_i} > \tag{5.12}$$

$$= -\frac{k_p\alpha}{\epsilon_0} < \mathbf{E_{ext}}^\dagger\bar{\bar{\epsilon}} \cdot \mathbf{E_i}, \mathbf{E_{ext}}^\dagger\bar{\bar{\epsilon}} \cdot \mathbf{E_i} >_{\text{OEO}} \tag{5.13}$$

We define the inner product $< \cdot, \cdot >_{\text{OEO}}$ when the integral only includes the region of OEO materials. The shift of the frequency due to electro-optic field is

$$\frac{\Delta\omega_i}{\omega_i} = \frac{k_p\alpha}{2\epsilon_0}\frac{< \mathbf{E_{ext}}^\dagger\bar{\bar{\epsilon}} \cdot \mathbf{E_i}, \mathbf{E_{ext}}^\dagger\bar{\bar{\epsilon}} \cdot \mathbf{E_i} >_{\text{OEO}}}{< \mathbf{E_i}, \bar{\bar{\epsilon}}\mathbf{E_i} >} \tag{5.14}$$

$$= \frac{k_p\alpha}{2\epsilon_0}\frac{\iiint_{\text{poly}} \epsilon^2|\mathbf{E_{ext}^T}\mathbf{E_i}|^2\mathrm{d}x\mathrm{d}y\mathrm{d}z}{\iiint_{\text{everywhere}} \epsilon|\mathbf{E_i}|^2\mathrm{d}x\mathrm{d}y\mathrm{d}z} \tag{5.15}$$

We made two assumptions in the equation 5.15. First, although we consider the anisotropic perturbation of the dielectric tensor, we assume that the dielectric tensor $\bar{\bar{\epsilon}}$ is isotropic. Thus we can use a scalar ϵ instead of tensor. Second, we assume that $\mathbf{E_{ext}}$ is a real vector as the tuning source frequency is much lower compared to the optical oscillation frequency.

If we approximate the average poling field as $|\overline{\mathbf{E_p}}| = V_p/w_g$, then we can estimate the average $\overline{r_{33}} = k_p|\overline{\mathbf{E_p}}| = k_pV_p/w_g$. Given tuning voltage V_{ext}, we could also get $\alpha = \frac{V_p}{V_{\text{ext}}}$. The definition of the overlap factor is

$$\frac{\Delta\omega}{\omega} = \frac{1}{2}\frac{\epsilon}{\epsilon_0}\overline{r_{33}}\Gamma_c\frac{V_{\text{ext}}}{w_g} \tag{5.16}$$

where V is the voltage, w_g is the slot gap width. Incorporate all these equations we can get the expressions for overlapping factor,

$$\Gamma_c = \frac{w_g^2}{V_{\text{ext}}^2}\frac{\iiint_{\text{poly}}\epsilon|\mathbf{E_{ext}^T E_i}|^2\mathrm{d}x\mathrm{d}y\mathrm{d}z}{\iiint_{\text{everywhere}}\epsilon|\mathbf{E}_i|^2\mathrm{d}x\mathrm{d}y\mathrm{d}z} \tag{5.17}$$

$\mathbf{E}_{\text{ext}}$ has a linear relationship with V_{ext}/w_g, so the overlapping factor is not relevant to the externally applied voltage.

Upon applying the above formula for the three modes discussed in the main text and the Au strip-integrated device, we record results in Table 5.A.1. The overlap factor

Modes	I.	II.	III.	I.(with gold)
Γ_c	0.156	0.017	0.015	0.127

Table 5.A.1: **The overlap factor Γ_c of the optical modes discussed in Fig. 5.2 and Fig.5.A.5.**

decreases slightly with the integration of Au strips due to the existence of metal absorption. Also, compared to the guided modes II and III, the slot mode achieves around one order of magnitude higher overlapping factor.

Effect of Additional metal strip on the loss of the slot mode resonance

To ensure a minimal metallic loss, metal strips are integrated at the center of the silicon rail and have a width of $100nm$. For $850nm$-wide slabs, metal strips have limited effect on the overlapping factor Γ_c, the resonance shift, and the overall absorption. Firstly, Γ_c decreases by 0.03 upon this insertion, shown in Tab.5.A.1. Secondly, informed from the simulated reflection spectra in Fig.5.A.5, the resonance shift from $n = 1.85$ to $n = 1.87$ is $2.71nm$. Thus, the extra metal strips hardly affect the sensitivity of the slot mode with respect to the electro-optic effect of the polymer. Finally, the calculated quality factors of the resonances with and without metal strips are 1864 and 1979 (Fig. 5.2f), respectively. Both quality factors are just slightly above our experimental realization, and the effect of the metal is minimal. In conclusion, the metal strip will only have minimal effect on the resonance property and the tuning performance.
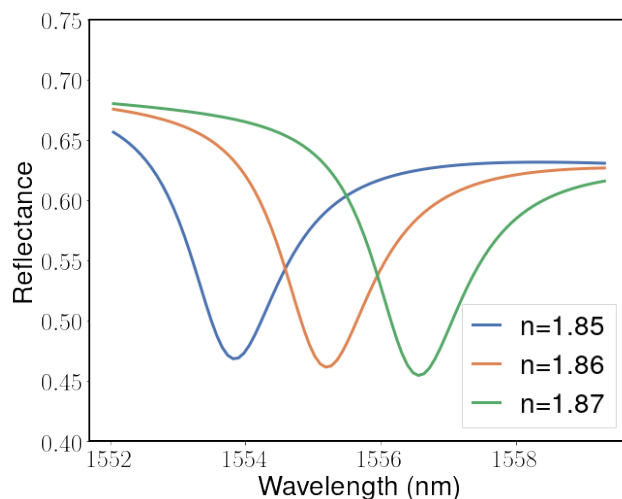
Figure 5.A.5: **Numerical calculation of the reflection spectra for the device with metal strips.** The spectra with different refractive indexes in the active region are plotted. The device structure is the same as shown in Fig. 5.2 but with the metal strip. The shift between $n = 1.85$ and $n = 1.87$ is 2.71nm.

The simplified circuit model and the RF measurement for the bandwidth estimation

In this section, we further discuss the simplified circuit model which has been used in Fig. 5.6b. The model parameters are chosen as described in the following paragraph. To determine the capacitance in the circuit and determine the primary limiting factor of the bandwidth in our device, we conduct electric transmission tests on different structures. The outcomes and the modeling circuits for each structure are shown in Fig. 5.A.6, and the illustrations of experimental setups are shown in Fig. 5.A.7.

First, we assess the bandwidth of the PCB board. The schematic diagram of the measurement setup is shown in Fig. 5.A.7a, and the result is represented by the purple curve in Fig. 5.A.6a. It is clear that signals below 20MHz remain unaffected. The bandwidth of the PCB board is significantly larger than all the other measurements; therefore, we do not take into account the effect of the PCB on the signal bandwidth.

Next, we measure the transmission of signals V_{out} through the PCB and an coplanar waveguide (CPW). Despite continuing to use a large electrode pad for wire bonding, the coplanar waveguide could significantly reduce the transmission loss through the waveguide. The gold electrode waveguide is situated on top of a thin film undoped silicon layer with a fused silica substrate[122]. The schematic diagram of the measurement setup can be seen in Fig. 5.A.7b. The measured data exhibits 3dB

attenuation at 21MHz.We model the circuit as a RC circuit shown in Fig. 5.A.6b. The calculation of V_{load} is

$$V_{\text{load}} = |\frac{Z_{\text{load}}}{R + Z_{\text{load}}}| \tag{5.18}$$

where $Z_{\text{load}} = \frac{1}{j2\pi f C_{\text{circ}}}$. The calculated capacitive load $C_{\text{circ}} = 262.5\text{pF}$.

Third, we measure the transmission spectra of signals through the PCB and the optimized RF waveguide on the SOI wafer in air (measurement data, circuit and diagram II in Fig. 5.A.6a-b and Fig. 5.A.7b). The SOI wafer introduces additional capacitance $C_{\text{SOI'}}$ between gold electrodes and the doped silicon substrate. Therefore in case II, $Z_{\text{load}} = \frac{1}{j2\pi f(C_{\text{circ}}+C_{\text{SOI'}})}$. Based on the measurement, the 3dB cutoff frequency is 6.8MHz. Therefore, we can estimate the capacitance of the SOI wafer in this case as $C_{\text{SOI'}} = 548.24\text{pF}$. As a sanity check, if we treat the SOI wafer capacitance as the parallel plate, then the capacitance $C_{\text{SOI'}}$ could be expressed as

$$C_{\text{SOI'}} = \frac{\epsilon_0 \epsilon_{\text{SiO}_2} S_{\text{SOI'}}}{2h_{\text{SiO}_2}} \tag{5.19}$$

ϵ_0 is the vacuum permittivity. We can solve the area of the whole waveguide $S_{\text{SOI'}} = 9.5mm^2$. It is similar to the area of the electrode design since there are two large pads for wire bonding. As our main device doesn't incorporate the CPW, the impedance unmatching through the waveguide will impact the load voltage V_{load}. To identify other possible parasitic capacitances in the circuit, we measure the loading voltage signal V_{load} with another test chip with a smaller electrode area (measurement data, circuit and diagram III in Fig. 5.A.6a-b and Fig. 5.A.7b). The measurement 3dB cutoff frequency is 4MHz. In this device, we assume that $Z_{\text{load}} = C_{\text{circ}} + C_{\text{SOI'}} + C_{\text{other}}$, which implies that the contribution of all other factors except for the original contribution in case I and SOI capacitance contribution in case II could be modeled as a capacitor C_{other}. We also assume that the area of the electrode is the same as in case II. The result $C_{\text{other}} = 567.5\text{pF}$. As such, we define the external capacitance of our device in optical measurement $C_{\text{load}} = C_{\text{circ}} + C_{\text{other}} = 813.5\text{pF}$. The substrate contribution of the device in the main figure is determined by the electrode area $S_{\text{SOI}} = 16mm^2$ in the device $C_{\text{SOI}}/2 = 920.82\text{pF}$ using equation 5.19 (since in Fig. 5.6 of the main manuscript the capacitance between the electrode and substrate is labeled as C_{SOI}). Based on all these discussions, the final model shown in Fig. 5.6b of the main manuscript considers two major capacitances, C_{load} and C_{SOI}, to capture the effect of the parasitic capacitance along the circuit and the substrate.
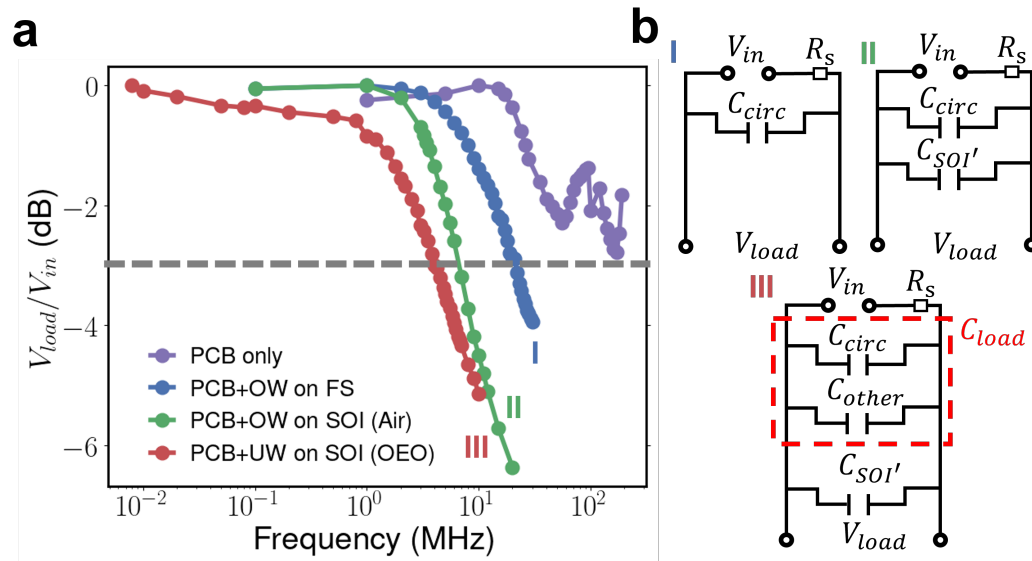
Figure 5.A.6: **Electrical tests for the circuit on other device structures.** The detected signal is the electric transmission signal (V_{load}) that passes through the electrode layout instead of optical modulation signal. a. measurement transmission V_{out}/V_{in} as a function of frequency. b. The equivalent circuit model for different structures. Purple curve : the signal only passes the PCB board. Blue curve (I): the signal passes the PCB board and an optimized waveguide (OW). The OW achieves impedance matching in most propagation region. The connections between PCB and waveguides are wire bonded. The substrate is replaced as fused silica. The 3dB bandwidth is 21MHz. R_s: source resistance. C_{circ}: the additional capacitance within PCB-bonding wire-waveguide circuit. Green curve (II): same setting as I but the substrate is SOI substrate. The waveguide is exposed to an air environment. The 3dB bandwidth is 6.8MHz. $C_{SOI'}$: the additional capacitance for optimized waveguide due to SOI substrate. Red curve (III): The device is coated with OEO material, and the waveguide is the same as the device in Fig. 5.6 of the main manuscript with a smaller wire bonding pad. The 3dB bandwidth is 4MHz. C_{other}: the additional capacitance due to impedance unmatching.

Within the device, we treat the electric path across the slot as two gold nanobars R_{Au}, two resistive silicon nanobars R_{Si}, a resistive component R_{OEO} and a capacitive component C_{OEO}. R_{OEO} and C_{OEO} are parallel connected to each other and series connected to R_{Si} and R_{Au}, as shown in Fig. 5.6 of the main manuscript. The resistance of the gold nanobar can be modeled as $R_{\text{Au}} = \frac{\rho_{\text{Au}} w_{\text{Au}}}{h_{\text{Au}} l_{\text{Au}}} = 338\Omega$, where $\rho_{\text{Au}} = 2.2 \times 10^{-6}\Omega \cdot cm$, $l_{\text{Au}} = 100\mu m$, $h_{\text{Au}} = 65nm$. Thanks to the extruded gold electrode, the resistance of the silicon bar can be modeled as $R_{\text{Si}} = \frac{\rho_{\text{Si}} w_{\text{Si}}}{h_{\text{Si}} l_{\text{Si}}} = 1.17k\Omega$, where $\rho_{\text{Si}} = 10\Omega \cdot cm$, $l_{\text{Si}} = 100\mu m$, $w_{\text{Si}} = 350nm$, $h_{\text{Si}} = 300nm$. The resistance of the OEO material is modelled as $R_{\text{OEO}} = \frac{\rho_{\text{OEO}} w_{\text{OEO}}}{h_{\text{OEO}} l_{\text{OEO}}} = 200G\Omega$, where $\rho_{\text{OEO}} = 6 \times 10^9\Omega \cdot cm$, $l_{\text{OEO}} = 100\mu m$, $h_{\text{OEO}} = 300nm$. The capacitance of the polymer is modeled approximately as a parallel capacitor, thus $C_{\text{OEO}} = \frac{\epsilon_0 \epsilon_{\text{OEO}} h_{\text{OEO}} l_{\text{OEO}}}{w_{\text{OEO}}} = 21.25fF$, where $\epsilon_{\text{OEO}} = 8$. The impedance of one slot is then $Z_{\text{single}} = 2R_{\text{Au}} + 2R_{\text{Si}} + Z_{\text{OEO}}$, where $Z_{\text{OEO}} = \frac{R_{\text{OEO}}}{1 + j2\pi f C_{\text{OEO}}}$. Thus, the total impedance of the device is $Z_{\text{dev}} = Z_{\text{single}}/N_{\text{slot}}$ where $N_{\text{slot}} = 90$.

Finally, incorporating all previous calculations we can get

$$V_{\text{OEO}} = V \frac{Z_{\text{dev}}}{Z_{\text{total}}} \frac{Z_{\text{OEO}}}{Z_{\text{single}}} \tag{5.20}$$

The calculated result is shown in Fig. 5.6a.

Discussion on the strategies of bandwidth improvement

Based on the discussion in supplementary note 4, we have identified the source factor of the bandwidth limitation. To increase the bandwidth of the device, we suggest the following strategies:

- Use doped silicon on fused silica wafer to remove C_{SOI}. This type of wafer will require the development of a specialized fabrication process, but it could be potentially constructed by ion implantation and annealing. This improvement could be supported by experiments I and II, as the replacement of the wafer will lead to the increase of the bandwidth in experiment I.

- The design and implementation of a microwave coplanar waveguide, combined with the use of a probe instead of wire bonding and meticulous removal of possible parasitic capacitance in the circuit, could effectively minimize C_{load}, and it has been shown in ref. [110]. We expect that in the ideal case the bandwidth should only be restricted by $R_{\text{Au}}, R_{\text{Si}}, C_{\text{OEO}}$ and R_{OEO}.
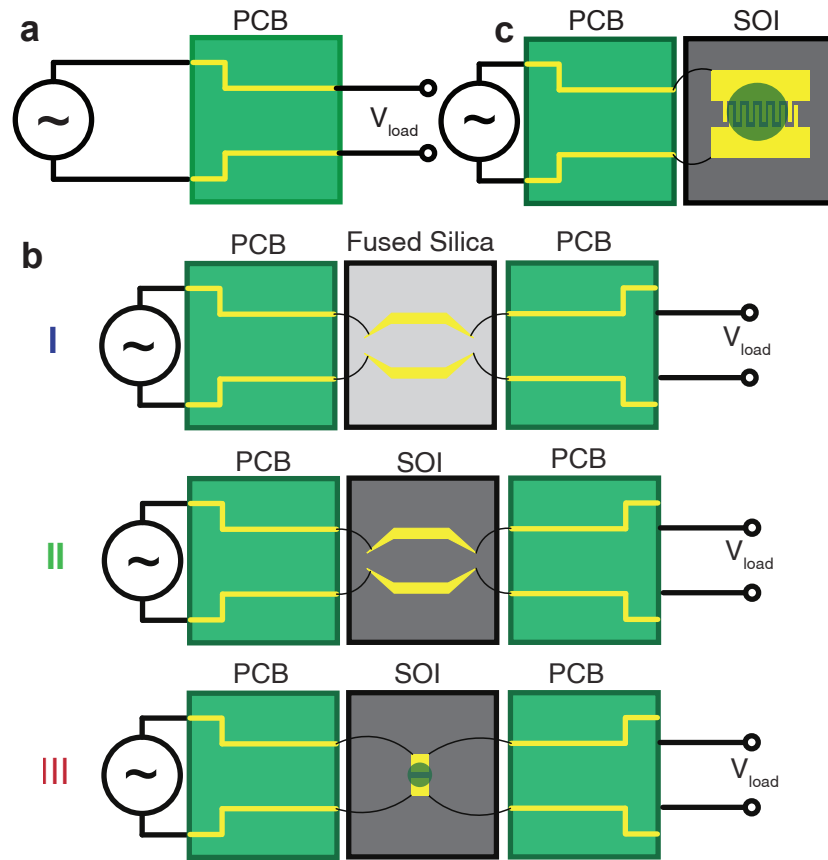
Figure 5.A.7: **Schematic diagrams of the AC measurements. a**. The diagram of the AC measurement for PCB speed. It corresponds to the PCB only measurement data in Fig. 5.A.6a. **b.** The diagrams of the AC measurement for case I,II,III in Fig. 5.A.6. **c.** The diagrams of the AC measurement for Fig. 5.6 of the main manuscript.

- The careful adjustment of doping levels, device length, and device geometry to tailor them toward achieving GHz bandwidth presents another feasible avenue for optimization. As shown in supplementary note 4, the bandwidth limitation by R_{Au},R_{Si},C_{OEO} and R_{OEO} is approximately $1/(2\pi(R_{Si} + R_{Au})C_{OEO}) = 4.8$GHz. The bandwidth could be further improved if we reduce the device length or increase the doping levels.

Therefore, we believe the silicon-organic electro-optic modulation device based on slot waveguide could achieve GHz bandwidth.
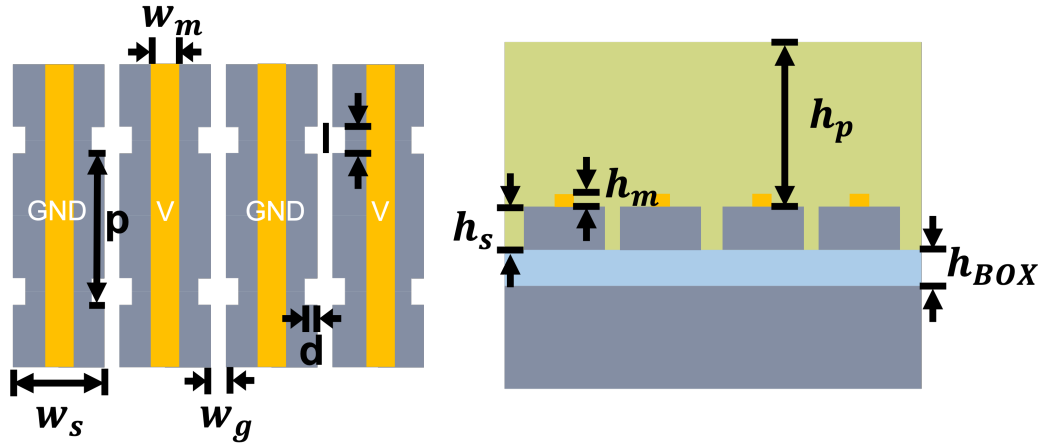
Figure 5.A.8: **Label of the device geometry.** p: period of the notch. d: width of the notch. l: length of the notch. w_s: slab width. w_g: slot width. w_m: metal width. h_s: the height of the SOI device layer. h_m: the height of the metal electrode layer. h_p: the height of the OEO material layer minus the height of the SOI device layer (include h_m). h_{BOX}: the height of the buffered oxide layer.

Fabrication and poling workflows, measurement setup

The detailed fabrication workflow is shown in Fig. 5.A.1.

The measurement setup, which has been discussed in detail in our previous report[70], is shown in Figure 5.A.2.

Device parameter details

We list the parameter details of the devices simulated or fabricated in the main figures. The symbols for the geometrical parameters are labeled in Fig. 5.A.2. All experimental devices are fabricated using an SOI wafer with a 300-nm device layer and a 300-nm BOX layer. For fabricated devices, the listed parameters are the design layout parameters with estimated geometry shifts due to fabrication. We estimate the geometry shift by the SEM image of other devices on the same chip.

Devices	p	w_g	w_s	d	l	w_m	h_p	h_m	h_s	h_{BOX}
Fig. 5.2	740	90	850	50	120	N/A	1200	65	300	300
Fig. 5.4	Varied	100	830	Varied	Varied	100	1800	65	300	300
Fig. 5.5a	720	90	840	60	130	100	1200	65	300	300
Fig. 5.5b	900	80	650	55	133	100	1200	65	300	300
Fig. 5.5c	880	80	650	55	133	100	1200	65	300	300
Fig. 5.7	700	100	700	60	160	100	1000	65	500	300
Fig. 5.8a-c	700	100	700	130	240	100	1800	65	600	720
Fig. 5.8d-f	595	90	500	50	120	100	1000	65	500	300

Table 5.A.2: Device parameters used for the plot in Chapter 5 (unit: nm). N/A: not applicable. Varied: the certain parameter is a variable in the main figures.

Chapter 6

CONCLUSION AND OUTLOOK

6.1 Summary

In this dissertation, I presented my research on reconfigurable photonics. Due to the small strength of the modulation mechanisms, bulk media could only generate limited response. Therefore, judicious engineering in the nanostructures plays an important role in enhancing the strength of the external modulation stimuli. For various target responses, the different kinds of nanophotonic modes will result in different effects.

For a nanophotonic mode, there are several aspects that determine its use: the mode field pattern, quality factor, and radiation rates for each port. Mode field pattern determines the inside energy distribution within the eigenmode, and a strong concentration of reconfigurable medium is preferred since it could enhance the sensitivity of the refractive index perturbation. Quality factor represents the total loss of the eigenmode. Although high-Q mode makes the optical response more sensitive, the decrease of the coupling also decreases the resonance amplitude in an under-coupled regime. Besides, high-Q mode limits the optical operation bandwidth. Therefore, a sweet spot of the quality factor of the mode is required. Radiation rates for each port represent the distribution of the energy loss through every port. This radiation pattern determines the coupling status between the incident light and the mode (under-coupling, critical-coupling or over-coupling). Even with the same type of eigenmode, altering the geometry of the device could switch the coupling status of the device. Therefore, nanophotonics design is a complicated process and needs to be considered simultaneously with the target response, target wavelength, material constraints, modulation mechanism, fabrication limitation and many more customized factors specific to the problem. I showcase several examples in this dissertation.

In Chapter 3, our goal was to enhance the phase response. We explored the use of GMR and quasi-BIC in the NEMS platform and demonstrated that dual-mode resonance could further improve its phase response. In Chapter 4, our goal was to control the amplitude and phase response. We focused on the mode field pattern characteristic of the slot mode and combined with the electrostatic modulation to

enhance its sensitivity. Based on this observation, various device layouts were proposed separately for the under-coupling regime for amplitude modulation and over-coupling regime for phase modulation. In Chapter 5, we noticed that the slot mode could be extended in the use of electro-optic material. In addition, the fast response and large refractive index change provided superior advantage in free-space modulation.

6.2   Outlook

The pursuit of power-efficient and compact reconfigurable devices never ends. Achieving this goal not only requires the advance of different research fields, but also requires the cross-disciplinary collaboration.

First, the modulation effect on the refractive index perturbation could be further improved. For example, in organic electro-optic materials, the electro-optic coefficient of organic molecules are consistently improved[120], and chemists are still trying to design new molecule structures that could provide higher nonlinear coefficient with low loss.

Second, the advance of nanophotonic design needs a large design space and advanced design techniques. In this dissertation, the nanostructures only exist in one layer. Multilayer metasurfaces could provide more freedom for the mode characteristics[66]. Moreover, our devices discussed here are all periodic and only include regular shapes. Inverse design techniques and machine learning techniques could greatly expand the design space from physics-intuitive design to computational-driven design, and generate highly-sophisticated results that are surprisingly suitable for reconfigurable photonics[45]. The advance of the fabrication will also contribute to the increase of the performance.

Metasurfaces have been proven to show great advantage over many conventional candidates in many static optical solutions. In the future, we believe that it will also play an important role in the advancement of reconfigurable optics.

BIBLIOGRAPHY

[1] A. Arbabi, Y. Horie, M. Bagheri, and A. Faraon, "Dielectric metasurfaces for complete control of phase and polarization with subwavelength spatial resolution and high transmission", Nature Nanotechnology **10**, 937–943 (2015) (cit. on pp. 1–2).

[2] A. V. Kildishev, A. Boltasseva, and V. M. Shalaev, "Planar photonics with metasurfaces", Science **339**, 12320091–12320096 (2013) (cit. on p. 1).

[3] S. Jahani and Z. Jacob, "All-dielectric metamaterials", Nature Nanotechnology **11**, 23–36 (2016) (cit. on p. 1).

[4] P. Lalanne and P. Chavel, "Metalenses at visible wavelengths: past, present, perspectives", Laser and Photonics Reviews **11**, 1600295 (2017) (cit. on p. 1).

[5] P. Genevet, F. Capasso, F. Aieta, M. Khorasaninejad, and R. Devlin, "Recent advances in planar optics: from plasmonic to dielectric metasurfaces", Optica **4**, 139 (2017) (cit. on p. 1).

[6] P. Qiao, W. Yang, and C. J. Chang-Hasnain, "Recent advances in high-contrast metastructures, metasurfaces, and photonic crystals", Advances in Optics and Photonics **10**, 180 (2018) (cit. on p. 1).

[7] S. M. Kamali, E. Arbabi, A. Arbabi, and A. Faraon, "A review of dielectric optical metasurfaces for wavefront control", Nanophotonics **7**, 1041–1068 (2018) (cit. on p. 1).

[8] E. Carrasco and J. A. Encinar, *Reflectarray antennas* (John Wiley & Sons, 2018), pp. 323–359 (cit. on p. 1).

[9] D. M. Pozar and T. A. Metzler, "Analysis of a reflectarray antenna using microstrip patches of variable size", Electronics Letters **29**, 657–658 (1993) (cit. on p. 1).

[10] N. Yu, P. Genevet, M. A. Kats, F. Aieta, J. P. Tetienne, F. Capasso, and Z. Gaburro, "Light propagation with phase discontinuities: Generalized laws of reflection and refraction", Science **334**, 333–337 (2011) (cit. on p. 1).

[11] M. Pan, Y. Fu, M. Zheng, H. Chen, Y. Zang, H. Duan, Q. Li, M. Qiu, and Y. Hu, "Dielectric metalens for miniaturized imaging systems: progress and challenges", Light: Science and Applications **11**, 195 (2022) (cit. on p. 2).

[12] J. P. Balthasar Mueller, N. A. Rubin, R. C. Devlin, B. Groever, and F. Capasso, "Metasurface Polarization Optics: Independent Phase Control of Arbitrary Orthogonal States of Polarization", Physical Review Letters **118**, 113901 (2017) (cit. on p. 2).

[13] Y. Yao, R. Shankar, M. A. Kats, Y. Song, J. Kong, M. Loncar, and F. Capasso, "Electrically tunable metasurface perfect absorbers for ultrathin mid-infrared optical modulators", Nano Letters **14**, 6526–6532 (2014) (cit. on p. 2).

[14] M. S. Faraji-Dana, E. Arbabi, A. Arbabi, S. M. Kamali, H. Kwon, and A. Faraon, "Compact folded metasurface spectrometer", Nature Communications **9**, 4196 (2018) (cit. on p. 2).

[15] H. Kwon, E. Arbabi, S. M. Kamali, M. Faraji-Dana, and A. Faraon, "Single-shot quantitative phase gradient microscopy using a system of multifunctional metasurfaces", Nature Photonics **14**, 109–114 (2020) (cit. on p. 2).

[16] A. C. Overvig, S. Shrestha, S. C. Malek, M. Lu, A. Stein, C. Zheng, and N. Yu, "Dielectric metasurfaces for complete and independent control of the optical amplitude and phase", Light: Science and Applications **8**, 92 (2019) (cit. on p. 2).

[17] S. M. Kamali, E. Arbabi, A. Arbabi, Y. Horie, M. S. Faraji-Dana, and A. Faraon, "Angle-multiplexed metasurfaces: Encoding independent wavefronts in a single metasurface under different illumination angles", Physical Review X **7**, 41056 (2017) (cit. on p. 2).

[18] P. Camayd-Muñoz, C. Ballew, G. Roberts, and A. Faraon, "Multifunctional volumetric meta-optics for color and polarization image sensors", Optica **7**, 280 (2020) (cit. on p. 2).

[19] Y. Zhou, H. Zheng, I. I. Kravchenko, and J. Valentine, "Flat optics for image differentiation", Nature Photonics **14**, 316–323 (2020) (cit. on p. 2).

[20] C. Guo, M. Xiao, M. Minkov, Y. Shi, and S. Fan, "Photonic crystal slab Laplace operator for image differentiation", Optica **5**, 251 (2018) (cit. on p. 2).

[21] D. N. Neshev and A. E. Miroshnichenko, "Enabling smart vision with metasurfaces", Nature Photonics **17**, 26–35 (2023) (cit. on p. 2).

[22] A. Arbabi and A. Faraon, "Fundamental limits of ultrathin metasurfaces", Scientific Reports **7**, 43722 (2017) (cit. on p. 2).

[23] D. A. Miller, "Why optics needs thickness", Science **379**, 41–45 (2023) (cit. on p. 2).

[24] Y. Zhou, I. I. Kravchenko, H. Wang, J. R. Nolen, G. Gu, and J. Valentine, "Multi-layer Noninteracting Dielectric Metasurfaces for Multiwavelength Metaoptics", Nano Letters **18**, 7529–7537 (2018) (cit. on p. 2).

[25] M. Mansouree, H. Kwon, E. Arbabi, A. McClung, A. Faraon, and A. Arbabi, "Multifunctional 2.5D metastructures enabled by adjoint optimization", Optica **7**, 77 (2020) (cit. on p. 2).

[26] G. Kafaie Shirmanesh, R. Sokhoyan, R. A. Pala, and H. A. Atwater, "Dual-Gated Active Metasurface at 1550 nm with Wide (>300°) Phase Tunability", Nano Letters **18**, 2957–2963 (2018) (cit. on p. 4).

[27] G. K. Shirmanesh, R. Sokhoyan, P. C. Wu, and H. A. Atwater, "Electro-optically Tunable Multifunctional Metasurfaces", ACS Nano **14**, 6912–6920 (2020) (cit. on pp. 4, 18, 47, 52, 76).

[28] J. Park, B. G. Jeong, S. I. Kim, D. Lee, J. Kim, C. Shin, C. B. Lee, T. Otsuka, J. Kyoung, S. Kim, K. Y. Yang, Y. Y. Park, J. Lee, I. Hwang, J. Jang, S. H. Song, M. L. Brongersma, K. Ha, S. W. Hwang, H. Choo, and B. L. Choi, "All-solid-state spatial light modulator with independent phase and amplitude control for three-dimensional LiDAR applications", Nature Nanotechnology **16**, 69–76 (2021) (cit. on pp. 4, 18, 47, 52, 76).

[29] S. I. Kim, J. Park, B. G. Jeong, D. Lee, K. Y. Yang, Y. Y. Park, K. Ha, and H. Choo, "Two-dimensional beam steering with tunable metasurface in infrared regime", Nanophotonics **11**, 2719–2726 (2022) (cit. on p. 4).

[30] M. Li, S. Biswas, C. U. Hail, and H. A. Atwater, "Refractive Index Modulation in Monolayer Molybdenum Diselenide", Nano Letters **21**, 7602–7608 (2021) (cit. on p. 5).

[31] Y. Yu, Y. Yu, L. Huang, H. Peng, L. Xiong, and L. Cao, "Giant Gating Tunability of Optical Refractive Index in Transition Metal Dichalcogenide Monolayers", Nano Letters **17**, 3613–3618 (2017) (cit. on p. 5).

[32] I. Datta, S. H. Chae, G. R. Bhatt, M. A. Tadayon, B. Li, Y. Yu, C. Park, J. Park, L. Cao, D. N. Basov, J. Hone, and M. Lipson, "Low-loss composite photonic platform based on 2D semiconductor monolayers", Nature Photonics **14**, 256–262 (2020) (cit. on p. 5).

[33] T. I. Andersen, R. J. Gelly, G. Scuri, B. L. Dwyer, D. S. Wild, R. Bekenstein, A. Sushko, J. Sung, Y. Zhou, A. A. Zibrov, X. Liu, A. Y. Joe, K. Watanabe, T. Taniguchi, S. F. Yelin, P. Kim, H. Park, and M. D. Lukin, "Beam steering at the nanosecond time scale with an atomically thin reflector", Nature Communications **13**, 3431 (2022) (cit. on p. 5).

[34] Q. Li, J.-H. Song, F. Xu, J. van de Groep, J. Hong, A. Daus, Y. J. Lee, A. C. Johnson, E. Pop, F. Liu, and M. L. Brongersma, "A Purcell-enabled monolayer semiconductor free-space optical modulator", Nature Photonics **17**, 897–903 (2023) (cit. on p. 5).

[35] Y. Zhang, C. Fowler, J. Liang, B. Azhar, M. Y. Shalaginov, S. Deckoff-Jones, S. An, J. B. Chou, C. M. Roberts, V. Liberman, M. Kang, C. Ríos, K. A. Richardson, C. Rivero-Baleine, T. Gu, H. Zhang, and J. Hu, "Electrically reconfigurable non-volatile metasurface using low-loss optical phase-change material", Nature Nanotechnology **16**, 661–666 (2021) (cit. on p. 5).

[36] Y. Wang, P. Landreman, D. Schoen, K. Okabe, A. Marshall, U. Celano, H. S. Wong, J. Park, and M. L. Brongersma, "Electrical tuning of phase-change antennas and metasurfaces", Nature Nanotechnology **16**, 667–672 (2021) (cit. on p. 5).

[37] S. Q. Li, X. Xu, R. M. Veetil, V. Valuckas, R. Paniagua-Domínguez, and A. I. Kuznetsov, "Phase-only transmissive spatial light modulator based on tunable dielectric metasurface", Science **364**, 1087–1090 (2019) (cit. on p. 5).

[38] P. Moitra, X. Xu, R. Maruthiyodan Veetil, X. Liang, T. W. Mass, A. I. Kuznetsov, and R. Paniagua-Domínguez, "Electrically Tunable Reflective Metasurfaces with Continuous and Full-Phase Modulation for High-Efficiency Wavefront Control at Visible Frequencies", ACS Nano **17**, 16952–16959 (2023) (cit. on p. 5).

[39] S. M. Kamali, A. Arbabi, E. Arbabi, Y. Horie, and A. Faraon, "Decoupling optical function and geometrical form using conformal flexible dielectric metasurfaces", Nature Communications **7**, 1–7 (2016) (cit. on p. 5).

[40] A. Karvounis, B. Gholipour, K. F. MacDonald, and N. I. Zheludev, "Giant Electro-Optical Effect through Electrostriction in a Nanomechanical Metamaterial", Advanced Materials **31**, 1804801 (2019) (cit. on pp. 5, 21, 24–25).

[41] A. L. Holsteen, A. F. Cihan, and M. L. Brongersma, "Temporal color mixing and dynamic beam shaping with silicon metasurfaces", Science **365**, 257–260 (2019) (cit. on pp. 5, 21).

[42] A. Archetti, R. J. Lin, N. Restori, F. Kiani, T. V. Tsoulos, and G. Tagliabue, "Thermally reconfigurable metalens", Nanophotonics **11**, 3969–3980 (2022) (cit. on p. 5).

[43] S. C. Malek, C.-C. Tsai, and N. Yu, "Thermally-switchable metalenses based on quasi-bound states in the continuum", arXiv preprint arXiv:2306.13644 (2023) (cit. on p. 5).

[44] R. A. Soref and B. R. Bennett, "Electrooptical effects in silicon", IEEE Journal of Quantum Electronics **23**, 123–129 (1987) (cit. on p. 6).

[45] C. L. Panuski, I. Christen, M. Minkov, C. J. Brabec, S. Trajtenberg-Mills, A. D. Griffiths, J. J. McKendry, G. L. Leake, D. J. Coleman, C. Tran, J. St Louis, J. Mucci, C. Horvath, J. N. Westwood-Bachman, S. F. Preble, M. D. Dawson, M. J. Strain, M. L. Fanto, and D. R. Englund, "A full degree-of-freedom spatiotemporal light modulator", Nature Photonics 2022 16:12 **16**, 834–842 (2022) (cit. on pp. 6, 92).

[46] J. D. Joannopoulos, S. G. Johnson, J. N. Winn, and R. D. Meade, *Photonic Crystals: molding the flow of light* (Princeton University Press, Oct. 2011) (cit. on pp. 7, 80–81).

[47] C. Cohen-Tannoudji, B. Diu, and F. Laloe, "Quantum mechanics, volume 1", Quantum Mechanics **1**, 898 (1986) (cit. on pp. 9, 62).

[48] T. Tamir, "INHOMOGENEOUS WAVE TYPES AT PLANAR INTERFACES - 3. LEAKY WAVES.", Optik (Jena) **38**, 269–297 (1973) (cit. on p. 11).

[49] S. S. Wang and R. Magnusson, "Theory and applications of guided-mode resonance filters", Applied Optics **32**, 2606 (1993) (cit. on p. 11).

[50] L. Huang, R. Jin, C. Zhou, G. Li, L. Xu, A. Overvig, F. Deng, X. Chen, W. Lu, A. Alù, and A. E. Miroshnichenko, "Ultrahigh-Q guided mode resonances in an All-dielectric metasurface", Nature Communications 14, 1–9 (2023) (cit. on p. 11).

[51] S. J. Kim and M. L. Brongersma, "Active flat optics using a guided mode resonance", Optics Letters 42, 5 (2017) (cit. on p. 11).

[52] C. W. Hsu, B. Zhen, A. D. Stone, J. D. Joannopoulos, and M. Soljačić, "Bound states in the continuum", Nature Reviews Materials 1, 16048 (2016) (cit. on pp. 11, 23, 32).

[53] K. Koshelev, A. Bogdanov, and Y. Kivshar, "Engineering with Bound States in the Continuum", Optics and Photonics News 31, 38 (2020) (cit. on p. 11).

[54] K. Koshelev, S. Lepeshov, M. Liu, A. Bogdanov, and Y. Kivshar, "Asymmetric Metasurfaces with High- Q Resonances Governed by Bound States in the Continuum", Physical Review Letters 121, 193903 (2018) (cit. on pp. 11, 23, 38).

[55] C. W. Hsu, B. Zhen, J. Lee, S. L. Chua, S. G. Johnson, J. D. Joannopoulos, and M. Soljacic, "Observation of trapped light within the radiation continuum", Nature 499, 188–191 (2013) (cit. on p. 11).

[56] F. H. Stillinger and D. R. Herrick, "Bound states in the continuum", Physical Review A 11, 446–454 (1975) (cit. on p. 11).

[57] A. C. Overvig, S. C. Malek, M. J. Carter, S. Shrestha, and N. Yu, "Selection rules for quasibound states in the continuum", Physical Review B 102, 035434 (2020) (cit. on pp. 11, 20, 30).

[58] A. Kodigala, T. Lepetit, Q. Gu, B. Bahari, Y. Fainman, and B. Kanté, "Lasing action from photonic bound states in continuum", Nature 541, 196–199 (2017) (cit. on pp. 11, 20).

[59] K. Koshelev, Y. Tang, K. Li, D. Y. Choi, G. Li, and Y. Kivshar, "Nonlinear Metasurfaces Governed by Bound States in the Continuum", ACS Photonics 6, 1639–1644 (2019) (cit. on pp. 11, 20).

[60] K. Fan, I. V. Shadrivov, and W. J. Padilla, "Dynamic bound states in the continuum", Optica 6, 169 (2019) (cit. on pp. 11, 20–21).

[61] S. Fan, W. Suh, and J. D. Joannopoulos, "Temporal coupled-mode theory for the Fano resonance in optical resonators", Journal of the Optical Society of America A 20, 569 (2003) (cit. on pp. 12–13, 27, 49, 69).

[62] K. X. Wang, Z. Yu, S. Sandhu, and S. Fan, "Fundamental bounds on decay rates in asymmetric single-mode optical resonators", Optics Letters 38, 100 (2013) (cit. on p. 14).

[63] G. Liang, H. Huang, A. Mohanty, M. C. Shin, X. Ji, M. J. Carter, S. Shrestha, M. Lipson, and N. Yu, "Robust, efficient, micrometre-scale phase modulators at visible wavelengths", Nature Photonics **15**, 908–913 (2021) (cit. on p. 16).

[64] Y. Horie, A. Arbabi, E. Arbabi, S. M. Kamali, and A. Faraon, "High-Speed, Phase-Dominant Spatial Light Modulation with Silicon-Based Active Resonant Antennas", ACS Photonics **5**, 1711–1717 (2018) (cit. on pp. 18, 27, 31, 47, 49, 66).

[65] X. Yin, J. Jin, M. Soljačić, C. Peng, and B. Zhen, "Observation of topologically enabled unidirectional guided resonances", Nature **580**, 467–471 (2020) (cit. on p. 18).

[66] H. Kwon, T. Zheng, and A. Faraon, "Nano-electromechanical spatial light modulator enabled by asymmetric resonant dielectric metasurfaces", Nature Communications **13**, 5811 (2022) (cit. on pp. 18, 76, 92).

[67] J. Y. Kim, J. Park, G. R. Holdman, J. T. Heiden, S. Kim, V. W. Brar, and M. S. Jang, "Full 2π tunable phase modulation using avoided crossing of resonances", Nature Communications **13**, 2103 (2022) (cit. on pp. 19, 52).

[68] M. Decker, I. Staude, M. Falkner, J. Dominguez, D. N. Neshev, I. Brener, T. Pertsch, and Y. S. Kivshar, "High-Efficiency Dielectric Huygens' Surfaces", Advanced Optical Materials **3**, 813–820 (2015) (cit. on p. 19).

[69] M. Liu and D.-Y. Choi, "Extreme Huygens' Metasurfaces Based on Quasi-Bound States in the Continuum", Nano Letters **18**, 8062–8069 (2018) (cit. on p. 19).

[70] H. Kwon, T. Zheng, and A. Faraon, "Nano-electromechanical Tuning of Dual-Mode Resonant Dielectric Metasurfaces for Dynamic Amplitude and Phase Modulation", Nano Letters **21**, 2817–2823 (2021) (cit. on pp. 20, 43–44, 55, 57, 75, 89).

[71] R. Magnusson and M. Shokooh-Saremi, "Widely tunable guided-mode resonance nanoelectromechanical RGB pixels", Optics Express **15**, 10903 (2007) (cit. on p. 20).

[72] K. Hirose, Y. Liang, Y. Kurosaka, A. Watanabe, T. Sugiyama, and S. Noda, "Watt-class high-power, high-beam-quality photonic-crystal lasers", Nature Photonics **8**, 406–411 (2014) (cit. on p. 20).

[73] Z. Liu, Y. Xu, Y. Lin, J. Xiang, T. Feng, Q. Cao, J. Li, S. Lan, and J. Liu, "High-Q Quasibound States in the Continuum for Nonlinear Metasurfaces", Physical Review Letters **123**, 253901 (2019) (cit. on pp. 20, 25).

[74] N. Karl, P. P. Vabishchevich, S. Liu, M. B. Sinclair, G. A. Keeler, G. M. Peake, and I. Brener, "All-optical tuning of symmetry protected quasi bound states in the continuum", Applied Physics Letters **115**, 141103 (2019) (cit. on pp. 20–21).

[75] S. Han, L. Cong, Y. K. Srivastava, B. Qiang, M. V. Rybin, A. Kumar, R. Jain, W. X. Lim, V. G. Achanta, S. S. Prabhu, Q. J. Wang, Y. S. Kivshar, and R. Singh, "All-Dielectric Active Terahertz Photonics Driven by Bound States in the Continuum", Advanced Materials **31**, 1901921 (2019) (cit. on pp. 20–21).

[76] S. C. Malek, A. C. Overvig, S. Shrestha, and N. Yu, "Active nonlocal metasurfaces", Nanophotonics **10**, 655–665 (2020) (cit. on pp. 20–21, 30).

[77] A. Tittl, A. Leitis, M. Liu, F. Yesilkoy, D.-Y. Choi, D. N. Neshev, Y. S. Kivshar, and H. Altug, "Imaging-based molecular barcoding with pixelated dielectric metasurfaces", Science **360**, 1105–1109 (2018) (cit. on p. 20).

[78] A. M. Shaltout, V. M. Shalaev, and M. L. Brongersma, "Spatiotemporal light control with active metasurfaces", Science **364**, 10.1126/science.aat3100 (2019) (cit. on p. 20).

[79] Y. Kanamori, N. Matsuyama, and K. Hane, "Resonant-Wavelength Tuning of a Pitch-Variable 1-D Photonic Crystal Filter at Telecom Frequencies", IEEE Photonics Technology Letters **20**, 1136–1138 (2008) (cit. on p. 21).

[80] M. J. Uddin and R. Magnusson, "Guided-Mode Resonant Thermo-Optic Tunable Filters", IEEE Photonics Technology Letters **25**, 1412–1415 (2013) (cit. on p. 21).

[81] A. Sharon, H. G. Weber, H. Engel, D. Rosenblatt, A. A. Friesem, and R. Steingrueber, "Light modulation with resonant grating–waveguide structures", Optics Letters **21**, 1564 (1996) (cit. on p. 21).

[82] T. Katchalski, G. Levy-Yurista, A. A. Friesem, G. Martin, R. Hierle, and J. Zyss, "Light modulation with electro-optic polymer-based resonant grating waveguide structures", Optics Express **13**, 4645 (2005) (cit. on p. 21).

[83] N. I. Zheludev and E. Plum, "Reconfigurable nanomechanical photonic metamaterials", Nature Nanotechnology **11**, 16–22 (2016) (cit. on pp. 21, 43).

[84] S.-G. Lee and R. Magnusson, "Band flips and bound-state transitions in leaky-mode photonic lattices", Physical Review B **99**, 045304 (2019) (cit. on p. 23).

[85] H. Honma, K. Takahashi, M. Ishida, and K. Sawada, "A Low-Voltage and High Uniformity Nano-Electro-Mechanical System Tunable Color Filter Based on Subwavelength Grating", Japanese Journal of Applied Physics **51**, 11PA01 (2012) (cit. on p. 24).

[86] Jin Yufeng and Zhang Jiaxun, "MEMS Vacuum Packaging Technology and Applications", in 2005 6th international conference on electronic packaging technology (IEEE, 2003), pp. 1–5 (cit. on p. 25).

[87] H. A. Haus, *Waves and fields in optoelectronics* (Prentice-Hall, 1984) (cit. on p. 27).

[88] J. Park, J.-H. Kang, S. J. Kim, X. Liu, and M. L. Brongersma, "Dynamic Reflection Phase and Polarization Control in Metasurfaces", Nano Letters **17**, 407–413 (2017) (cit. on p. 27).

[89] K. Koshelev, S. Kruk, E. Melik-Gaykazyan, J.-H. Choi, A. Bogdanov, H.-G. Park, and Y. Kivshar, "Subwavelength dielectric resonators for nonlinear nanophotonics", Science **367**, 288–292 (2020) (cit. on p. 30).

[90] A. Forouzmand and H. Mosallaei, "A Tunable Semiconductor-Based Transmissive Metasurface: Dynamic Phase Control with High Transmission Level", Laser & Photonics Reviews **14**, 1900353 (2020) (cit. on p. 30).

[91] J. S. Ginsberg, A. C. Overvig, M. M. Jadidi, S. C. Malek, G. N. Patwardhan, N. Swenson, N. Yu, and A. L. Gaeta, "Enhanced harmonic generation in gases using an all-dielectric metasurface", Nanophotonics **10**, 733–740 (2020) (cit. on p. 30).

[92] V. Liu and S. Fan, "S4 : A free electromagnetic solver for layered periodic structures", Computer Physics Communications **183**, 2233–2244 (2012) (cit. on p. 30).

[93] T. Zheng, H. Kwon, and A. Faraon, "Nanoelectromechanical tuning of high-q slot metasurfaces", Nano Letters **23**, PMID: 37306317, 5588–5594 (2023) (cit. on p. 37).

[94] M. Lawrence, D. R. Barton, and J. A. Dionne, "Nonreciprocal Flat Optics with Silicon Metasurfaces", Nano Letters **18**, 1104–1109 (2018) (cit. on pp. 38, 62, 79).

[95] M. Lawrence, D. R. Barton, J. Dixon, J.-H. Song, J. van de Groep, M. L. Brongersma, and J. A. Dionne, "High quality factor phase gradient metasurfaces", Nature Nanotechnology **15**, 956–961 (2020) (cit. on pp. 38, 64, 79).

[96] V. R. Almeida, Q. Xu, C. A. Barrios, and M. Lipson, "Guiding and confining light in void nanostructure", Optics Letters **29**, 1209 (2004) (cit. on p. 38).

[97] L. Chen, J. Shakya, and M. Lipson, "Subwavelength confinement in an integrated metal slot waveguide on silicon", Optics Letters **31**, 2133 (2006) (cit. on pp. 38, 62).

[98] P. Sanchis, J. Blasco, A. Martinez, and J. Marti, "Design of Silicon-Based Slot Waveguide Configurations for Optimum Nonlinear Performance", Journal of Lightwave Technology **25**, 1298–1305 (2007) (cit. on p. 38).

[99] T. Claes, J. Molera, K. De Vos, E. Schacht, R. Baets, and P. Bienstman, "Label-Free Biosensing With a Slot-Waveguide-Based Ring Resonator in Silicon on Insulator", IEEE Photonics Journal **1**, 197–204 (2009) (cit. on p. 38).

[100] S. Ummethala, J. N. Kemal, A. S. Alam, M. Lauermann, A. Kuzmin, Y. Kutuvantavida, S. H. Nandam, L. Hahn, D. L. Elder, L. R. Dalton, T. Zwick, S. Randel, W. Freude, and C. Koos, "Hybrid electro-optic modulator combining silicon photonic slot waveguides with high-k radio-frequency slotlines", Optica **8**, 511 (2021) (cit. on pp. 38, 69).

[101] J. D. Ryckman and S. M. Weiss, "Localized Field Enhancements in Guided and Defect Modes of a Periodic Slot Waveguide", IEEE Photonics Journal **3**, 986–995 (2011) (cit. on p. 40).

[102] H. Du, W. Zhang, C. G. Littlejohns, S. Stankovic, X. Yan, D. T. Tran, G. J. Sharp, F. Y. Gardes, D. J. Thomson, M. Sorel, G. Z. Mashanovich, and G. T. Reed, "Ultra-sharp asymmetric Fano-like resonance spectrum on Si photonic platform", Optics Express **27**, 7365 (2019) (cit. on p. 45).

[103] D. Conteduca, G. S. Arruda, I. Barth, Y. Wang, T. F. Krauss, and E. R. Martins, "Beyond Q : The Importance of the Resonance Amplitude for Photonic Sensors", ACS Photonics **9**, 1757–1763 (2022) (cit. on p. 45).

[104] J. Kühne, J. Wang, T. Weber, L. Kühner, S. A. Maier, and A. Tittl, "Fabrication robustness in BIC metasurfaces", Nanophotonics **10**, 4305–4312 (2021) (cit. on p. 45).

[105] H. R. Tofteberg, K. Schjølberg-Henriksen, E. J. Fasting, A. S. Moen, M. M. V. Taklo, E. U. Poppe, and C. J. Simensen, "Wafer-level Au–Au bonding in the 350–450 °C temperature range", Journal of Micromechanics and Microengineering **24**, 084002 (2014) (cit. on p. 49).

[106] E. W. Wang, T. Phan, S.-J. Yu, S. Dhuey, and J. A. Fan, "Dynamic circular birefringence response with fractured geometric phase metasurface systems", Proceedings of the National Academy of Sciences **119**, e2122085119 (2022) (cit. on p. 49).

[107] S. Jahani, S. Kim, J. Atkinson, J. C. Wirth, F. Kalhor, A. A. Noman, W. D. Newman, P. Shekhar, K. Han, V. Van, R. G. DeCorby, L. Chrostowski, M. Qi, and Z. Jacob, "Controlling evanescent waves using silicon photonic all-dielectric metamaterials for dense integration", Nature Communications **9**, 1893 (2018) (cit. on p. 50).

[108] E. Klopfer, S. Dagli, D. Barton, M. Lawrence, and J. A. Dionne, "High-Quality-Factor Silicon-on-Lithium Niobate Metasurfaces for Electro-optically Reconfigurable Wavefront Shaping", Nano Letters **22**, 1703–1709 (2022) (cit. on pp. 50, 74, 76).

[109] P. Thureja, G. K. Shirmanesh, K. T. Fountaine, R. Sokhoyan, M. Grajower, and H. A. Atwater, "Array-Level Inverse Design of Beam Steering Active Metasurfaces", ACS Nano **14**, 15042–15055 (2020) (cit. on p. 52).

[110] I.-C. Benea-Chelmus, S. Mason, M. L. Meretska, D. L. Elder, D. Kazakov, A. Shams-Ansari, L. R. Dalton, and F. Capasso, "Gigahertz free-space electro-optic modulators based on Mie resonances", Nature Communications **13**, 3170 (2022) (cit. on pp. 57, 60, 66, 69, 71, 75–76, 87).

[111] T. Zheng, Y. Gu, H. Kwon, G. Roberts, and A. Faraon, "Low-voltage dynamic light manipulation with silicon-organic slot metasurfaces", 10.21203/RS.3.RS-3001703/V1 (2023) (cit. on p. 59).

[112] A. L. Gaeta, M. Lipson, and T. J. Kippenberg, "Photonic-chip-based frequency combs", Nature Photonics **13**, 158–169 (2019) (cit. on p. 60).

[113] G. P. Agrawal, "Nonlinear Fiber Optics", in *Nonlinear science at the dawn of the 21st century* (Elsevier, 2013), pp. 195–211 (cit. on p. 60).

[114] C. Wang, M. Zhang, X. Chen, M. Bertrand, A. Shams-Ansari, S. Chandrasekhar, P. Winzer, and M. Lončar, "Integrated lithium niobate electro-optic modulators operating at CMOS-compatible voltages", Nature **562**, 101–104 (2018) (cit. on p. 60).

[115] A. Weiss, C. Frydendahl, J. Bar-David, R. Zektzer, E. Edrei, J. Engelberg, N. Mazurski, B. Desiatov, and U. Levy, "Tunable Metasurface Using Thin-Film Lithium Niobate in the Telecom Regime", ACS Photonics **9**, 605–612 (2022) (cit. on p. 60).

[116] C. Xiong, W. H. P. Pernice, and H. X. Tang, "Low-Loss, Silicon Integrated, Aluminum Nitride Photonic Circuits and Their Use for Electro-Optic Signal Processing", Nano Letters **12**, 3562–3568 (2012) (cit. on p. 60).

[117] A. Melikyan, L. Alloatti, A. Muslija, D. Hillerkuss, P. C. Schindler, J. Li, R. Palmer, D. Korn, S. Muehlbrandt, D. Van Thourhout, B. Chen, R. Dinu, M. Sommer, C. Koos, M. Kohl, W. Freude, and J. Leuthold, "High-speed plasmonic phase modulators", Nature Photonics **8**, 229–233 (2014) (cit. on p. 60).

[118] H. Murata, "Millimeter-Wave-Band Electro-Optic Modulators Using Antenna-Coupled Electrodes for Microwave Photonic Applications", Journal of Lightwave Technology **38**, 5485–5491 (2020) (cit. on p. 60).

[119] H. Xu, D. L. Elder, L. E. Johnson, Y. de Coene, S. R. Hammond, W. Vander Ghinst, K. Clays, L. R. Dalton, and B. H. Robinson, "Electro-Optic Activity in Excess of 1000 pm V $^{-1}$ Achieved via Theory-Guided Organic Chromophore Design", Advanced Materials **33**, 2104174 (2021) (cit. on p. 60).

[120] H. Xu, F. Liu, D. L. Elder, L. E. Johnson, Y. de Coene, K. Clays, B. H. Robinson, and L. R. Dalton, "Ultrahigh Electro-Optic Coefficients, High Index of Refraction, and Long-Term Stability from Diels-Alder Cross-Linkable Binary Molecular Glasses", Chemistry of Materials **32**, 1408–1421 (2020) (cit. on pp. 60, 62, 75, 92).

[121] J. Zhang, Y. Kosugi, A. Otomo, Y.-L. Ho, J.-J. Delaunay, Y. Nakano, and T. Tanemura, "Electrical tuning of metal-insulator-metal metasurface with electro-optic polymer", Applied Physics Letters **113**, 231102 (2018) (cit. on p. 60).

[122] I.-C. Benea-Chelmus, M. L. Meretska, D. L. Elder, M. Tamagnone, L. R. Dalton, and F. Capasso, "Electro-optic spatial light modulator from an engineered organic layer", Nature Communications **12**, 5928 (2021) (cit. on pp. 60, 64, 69, 80–81, 84).

[123] X. Sun, G. Liu, H. Yu, D. Ban, N. Deng, and F. Qiu, "Design and theoretical characterization of high speed metasurface modulators based on electro-optic polymer", Optics Express **29**, 9207 (2021) (cit. on p. 60).

[124] J. Leuthold, W. Freude, J.-M. Brosi, R. Baets, P. Dumon, I. Biaggio, M. L. Scimeca, F. Diederich, B. Frank, and C. Koos, "Silicon Organic Hybrid Technology-A Platform for Practical Nonlinear Optics", Proceedings of the IEEE **97**, 1304–1316 (2009) (cit. on p. 62).

[125] L. Alloatti, R. Palmer, S. Diebold, K. P. Pahl, B. Chen, R. Dinu, M. Fournier, J.-M. Fedeli, T. Zwick, W. Freude, C. Koos, and J. Leuthold, "100 GHz silicon-organic hybrid modulator", Light: Science & Applications **3**, e173–e173 (2014) (cit. on pp. 62, 76).

[126] C. Kieninger, Y. Kutuvantavida, D. L. Elder, S. Wolf, H. Zwickel, M. Blaicher, J. N. Kemal, M. Lauermann, S. Randel, W. Freude, L. R. Dalton, and C. Koos, "Ultra-high electro-optic activity demonstrated in a silicon-organic hybrid modulator", Optica **5**, 739 (2018) (cit. on p. 62).

[127] S. Kim, K.-H. Kim, and J. F. Cahoon, "Optical Bound States in the Continuum with Nanowire Geometric Superlattices", Physical Review Letters **122**, 187402 (2019) (cit. on p. 62).

[128] C. Wang, Q. Quan, S. Kita, Y. Li, and M. Lončar, "Single-nanoparticle detection with slot-mode photonic crystal cavities", Applied Physics Letters **106**, 261105 (2015) (cit. on p. 62).

[129] L. E. Johnson, D. L. Elder, S. J. Benight, A. F. Tillack, S. R. Hammond, W. Heni, L. R. Dalton, and B. H. Robinson, "Birefringence, dimensionality, and surface influences on organic hybrid electro-optic performance", in Physical chemistry of semiconductor materials and interfaces xx, Vol. 11799, edited by D. Congreve, C. Nielsen, A. J. Musser, and D. Baran (SPIE, Aug. 2021), p. 34 (cit. on pp. 62, 76).

[130] S. Fan and J. D. Joannopoulos, "Analysis of guided resonances in photonic crystal slabs", Physical Review B **65**, 235112 (2002) (cit. on p. 66).

[131] X. Sun, J. Sun, Z. Wang, L. Wang, F. Qiu, and L. Wen, "Manipulating Dual Bound States in the Continuum for Efficient Spatial Light Modulator", Nano Letters **22**, 9982–9989 (2022) (cit. on pp. 66, 75).

[132] H. Zwickel, S. Singer, C. Kieninger, Y. Kutuvantavida, N. Muradyan, T. Wahlbrink, S. Yokoyama, S. Randel, W. Freude, and C. Koos, "Verified equivalent-circuit model for slot-waveguide modulators", Optics Express **28**, 12951 (2020) (cit. on p. 69).

[133] S. Koeber, R. Palmer, M. Lauermann, W. Heni, D. L. Elder, D. Korn, M. Woessner, L. Alloatti, S. Koenig, P. C. Schindler, H. Yu, W. Bogaerts, L. R. Dalton, W. Freude, J. Leuthold, and C. Koos, "Femtojoule electro-optic modulation using a silicon-organic hybrid device", Light: Science & Applications **4**, e255–e255 (2015) (cit. on p. 69).

[134] G.-W. Lu, J. Hong, F. Qiu, A. M. Spring, T. Kashino, J. Oshima, M.-a. Ozawa, H. Nawata, and S. Yokoyama, "High-temperature-resistant silicon-polymer hybrid modulator operating at up to 200 Gbit s^{-1} for energy-efficient datacentres and harsh-environment applications", Nature Communications **11**, 4224 (2020) (cit. on p. 69).

[135] U. Koch, C. Uhl, H. Hettrich, Y. Fedoryshyn, C. Hoessbacher, W. Heni, B. Baeuerle, B. I. Bitachon, A. Josten, M. Ayata, H. Xu, D. L. Elder, L. R. Dalton, E. Mentovich, P. Bakopoulos, S. Lischke, A. Krüger, L. Zimmermann, D. Tsiokos, N. Pleros, M. Möller, and J. Leuthold, "A monolithic bipolar CMOS electronic-plasmonic high-speed transmitter", Nature Electronics **3**, 338–345 (2020) (cit. on p. 69).

[136] A. Chen, H. Sun, A. Szep, S. Shi, D. Prather, Z. Lin, R. S. Kim, and D. Abeysinghe, "Achieving Higher Modulation Efficiency in Electrooptic Polymer Modulator With Slotted Silicon Waveguide", Journal of Lightwave Technology **29**, 3310–3318 (2011) (cit. on p. 76).

[137] W. Jin, P. V. Johnston, D. L. Elder, A. F. Tillack, B. C. Olbricht, J. Song, P. J. Reid, R. Xu, B. H. Robinson, and L. R. Dalton, "Benzocyclobutene barrier layer for suppressing conductance in nonlinear optical devices during electric field poling", Applied Physics Letters **104**, 94_1 (2014) (cit. on p. 76).

[138] S. Huang, T.-D. Kim, J. Luo, S. K. Hau, Z. Shi, X.-H. Zhou, H.-L. Yip, and A. K.-Y. Jen, "Highly efficient electro-optic polymers through improved poling using a thin TiO2-modified transparent electrode", Applied Physics Letters **96**, 119 (2010) (cit. on p. 76).

[139] Z. Chen, X. Yin, J. Jin, Z. Zheng, Z. Zhang, F. Wang, L. He, B. Zhen, and C. Peng, "Observation of miniaturized bound states in the continuum with ultra-high quality factors", Science Bulletin **67**, 359–366 (2022) (cit. on p. 76).

[140] Y. Ren, P. Li, Z. Liu, Z. Chen, Y.-L. Chen, C. Peng, and J. Liu, "Low-threshold nanolasers based on miniaturized bound states in the continuum", Science Advances **8**, eade8817 (2022) (cit. on p. 76).

[141] J. D. Witmer, T. P. McKenna, P. Arrangoiz-Arriola, R. Van Laer, E. Alex Wollack, F. Lin, A. K.-Y. Jen, J. Luo, and A. H. Safavi-Naeini, "A silicon-organic hybrid platform for quantum microwave-to-optical transduction", Quantum Science and Technology **5**, 034004 (2020) (cit. on p. 81).

[142] R. W. Boyd, *Nonlinear Optics* (Elsevier, Jan. 2020), pp. 1–613 (cit. on p. 81).